DISSERTATION

ADVANCING THE CAPABILITY OF HIGH ENERGY YB:YAG LASERS: MULTILAYER COATINGS, PULSE SHAPING AND POST COMPRESSION

Submitted by

Hanchen Wang

Department of Physics

In partial fulfillment of the requirements

For the Degree of Doctor of Philosophy

Colorado State University

Fort Collins, Colorado

Summer 2022

Doctoral Committee:

Advisor: Jorge Rocca

Jacob Roberts
Siu Au Lee
Mario Maroni

ABSTRACT

ADVANCING THE CAPABILITY OF HIGH ENERGY YB:YAG LASERS:

MULTILAYER COATINGS, PULSE SHAPING AND POST COMPRESSION

Recently, cryogenically cooled Yb-doped amplifiers have been successfully scaled both in output energy and in repetition rate. The performance of such laser systems and their applications can be expanded by advancements in the development of optical coatings, that allow for scaling to higher pulse energies; as well as improvements in pulse shaping that include shorter pulse durations and the generation of programmable sequences of ultrashort pulses.

This dissertation focuses on realizing the improvements mentioned above for cryogenic Yb:YAG amplifiers. First it reports the evaluation of ion beam sputtering (IBS) dielectric coatings for Yb:YAG at the environmental conditions in which cryogenic amplifiers are operated. The IBS coatings showed consistent performance in ambient, vacuum and cryogenic conditions, with damage threshold measured 20.4±0.6 J/cm^2 for anti-reflection (AR) coating, and 27.4±1.3 J/cm^2 for high reflector (HR) coating with 280 ps pulse duration at 77 K under the ISO:21254 standard. Second, a method for synthesizing trains of high energy compressed pulses was demonstrated and used to pump an 18.9 nm Ni-like Mo plasma-based soft x-ray laser more efficiently. The synthesized pulse increased the conversion efficiency of this spatially coherent soft x-ray source by 40%. Finally, femtosecond pulses were generated by post compression using a gas filled hollow core fiber (HCF), in which spectral broadening was achieved by self-phase modulation with an additional contribution from stimulated Raman scattering. Utilizing nitrogen gas as the non-liner medium, 300 mJ, 8 ps pulses were broadened to 3.7 nm and re-compressed to 460 fs by a grating compressor. The propagation and spectral broadening of high energy picosecond pulses in gas-filled HCFs were modeled and the results of simulations were compared with experiments.

TABLE OF CONTENTS

Chapter 1 Introduction

With the introduction of chirped pulse amplification (CPA) in 1985 [1], the development of solid state lasers has taken a huge step forward. By adding a frequency dependent temporal dispersion, or positive chirp to the laser pulses prior to the amplifiers, the pulse duration is "stretched" in time. This "stretch" lowers the intensity in the amplifier by orders of magnitude preventing optical damage and enabling a higher energy output from the amplifiers. After amplification, the chirp can be compensated with negative dispersion, typically achieved by a pair of optical gratings, and the high energy pulses are "compressed" to short pulse duration suited to applications. The limit of this compression is linked to the gain bandwidth of the gain medium since the time-bandwidth product is limited by the uncertainty principle. When the time-bandwidth product reaches its minimum, for example, for a pulse with Gaussian temporal and spectral profile, this product is ~ 0.441, the pulse is then transform limited and can not be compressed further.

Ti:Al_2O_3 (Ti:sapphire) with its broad gain bandwidth holds an advantage for the generation of short pulses by CPA, typically in 20-100 fs range [2-4]. Soon after, the peak power of CPA Ti:sapphire lasers reached terawatt (TW) level [5] and much progress has been made scaling both energy and peak power of Ti:sapphire amplifiers up to 10 PW level [6-9]. However, the short upper state lifetime of Ti:sapphire (~ 3 μs [10]) and limitations on thermal loading requires the pump source to be high intensity short pulses. In the case of high pulse energy lasers this pump source is typically a frequency doubled, flash lamp pumped Nd:glass laser, whose repetition rate and average power are limited by thermal loading of the glass. This severely limits the repetition rate of Ti:sapphire CPA laser systems. On the other hand, laser diodes offer a more efficient, high repetition rate, high average power pump source, but their lower peak power requires a different gain medium with much longer upper level lifetime. Yb-doped materials, especially Yb:YAG, have an upper level lifetime of ~1 ms [11] and is particularly suited for laser diode pumping, and has seen extensive development in recent years as a laser gain medium.

Many applications require Joule-level ultrashort pulses at high repetition rates. Figure 1.1 summarized the range of laser parameter typically required, the pulse energy and pulse duration, for a number of selected applications of interest [12-17].

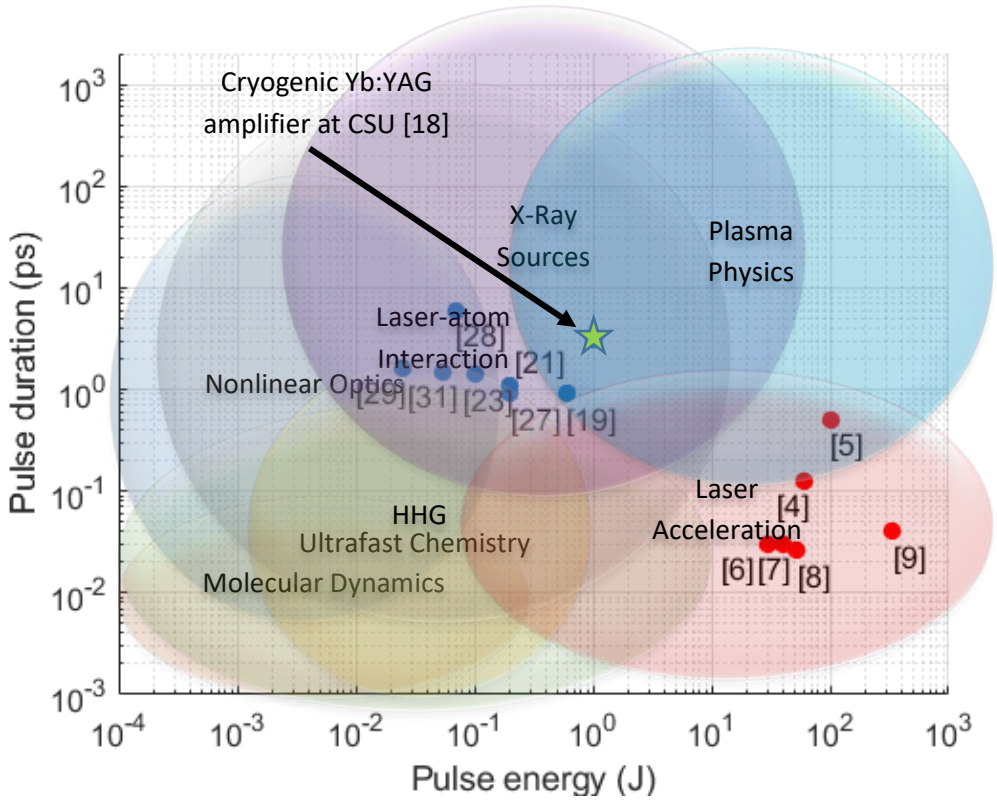

Figure 1.1. Summary of the requirement of pulse energy/pulse duration of applications from ultrafast lasers, and examples of reported high-energy solid state laser parameters. Red indicates Ti:sapphire systems, blue dots refer to Yb-doped systems. The reference for the laser systems[4-9, 19, 21, 23, 26-29, 31] is labeled next to the indicators.

Recently, both room temperature and cryogenically cooled Yb-doped amplifiers have been successfully scaled both in output energy and in repetition rate. A 1.1 J output at 1 kHz repetition rate has been demonstrated from a cryogenic Yb:YAG at Colorado State University (CSU) [18]. Up to 600 mJ output at 1 kHz repetition rate has been demonstrated with room temperature Yb:YAG amplifiers [19]. A large number of Yb based lasers capable of smaller energy at high

repetition rate have been reported [18, 20-30]. Laser pulse energy of 54 mJ with 0.5 kW average power has been demonstrated by Innoslab [31].

Applications such as high-harmonic generation (HHG) [23, 32] require short pulse durations and moderate energies. Plasma-based x-ray sources, coherent and incoherent, on the other hand, require higher energy. These include, plasma-based soft x-ray lasers [20, 24, 33], inverse Compton scattering sources [34, 35], bremssthraung and K-alpha x-ray sources [36]. Other applications include the generation of high energy density plasmas for high energy ion and electron acceleration [37-39], and neutron generation [40]. Another application of interest for ultrashort laser pulses is laser plasma wakefield acceleration for the generation of GeV electron beams. The latter three applications would in particular benefit from the high repletion rate of the diode-pumped Yb amplifiers if the output of such amplifiers could reach 100-fs level pulse width versus ps level in its current state. A discussion of techniques that can potentially achieve this can be found in Chapter 4.

This dissertation describes a 1 J cryogenic Yb:YAG ultrashort pulse laser and its applications. In Chapter 3, a pulse shaper capable of synthesizing ps-ns arbitrary pulse shape with up to 12 individual channels was demonstrated. The application of such tailored train of pulses to soft x-ray laser generation is presented. The results presented demonstrate a 50% increase in conversion efficiency of a tabletop 18.9 nm table-top soft x-ray laser source. In Chapter 4, a technique of spectral broadening and post compression of the cryogenic Yb:YAG amplifier by a gas-filled hollow core fiber (HCF) by >16x, and re-compress to 460 fs is demonstrated. Up to 300 mJ pulses can be coupled into the HCF and compressed by this technique, and could be scaled to higher energies. This post- compression technique, if further developed to obtain sub-100 fs pulses will benefit applications that require efficient drive lasers that have both high pulse energy and shorter pulse duration, such as high gradient plasma accelerators. Finally, the laser was employed to evaluate performance of ion beam sputtering (IBS) optical coatings in the

environmental conditions at which cryogenic Yb:YAG amplifiers are operated. The results are discussed in Chapter 2.

1.1 Cryogenic Yb:YAG laser

1.1.1 Yb:YAG

Ytterbium doped Yttrium aluminum garnet (Yb:YAG) is a popular gain medium for diode-pumped, high-energy solid state laser systems. The base YAG crystal has good thermal and mechanical properties [41], the ytterbium^{3+} dopant is often preferred over other ions such as Nd^{3+}, due to Yb^{3+} has a simpler electronic structure, low quantum defect when pumped by InGaAs diodes at λ = 940-980 nm, and a long upper level lifetime of up to ~1 ms [11, 42, 43]. All these characters combined with more efficient diode pumping, make high-power Yb-based solid state laser systems significantly more compact, and raise overall energy efficiency.

Apart from being more energy efficient and compact, laser diode pumping hold yet another advantage over flash lamp pumping, which is its narrow spectral bandwidth. Many high average power, commercially available diode stacks can reach 6-12 kW per individual stack when pulsing, while keeping a bandwidth less than 5 nm. When well-tuned, this narrow bandwidth can be matched to the peak absorption wavelength of Yb^{3+}, keeping a high conversion efficiency from pump photons to population of the upper laser state in the gain medium, which is critical for high-energy operation to any laser systems.

The host material, Yttrium aluminum garnet ($Y_3Al_5O_{12}$, YAG) has very good mechanical and thermal properties. YAG is a hard material and keeps its mechanical properties even under relative high doping ratio. It has lower thermal conductivity than some other gain medium choices like sapphire (8.6 W/m*K for undoped YAG versus 33 W/m*K for sapphire) at room temperature. However, as shown in Figure 1.2, when cooled to liquid nitrogen temperature of 77 K, its thermal conductivity is raised to 72 W/m*K for undoped YAG [41]. This value is reduced with doping,

but is still sufficient to significantly decrease the temperature gradient across the gain medium. This in turn minimizes the negative effects related to thermal load such as stress, thermal lensing, and increased saturation intensity. In recent years many Yb:YAG CPA laser systems have been demonstrated and have shown the capability to obtain high energy single pulse and high average power [28] [42] [20] [19, 22, 31].

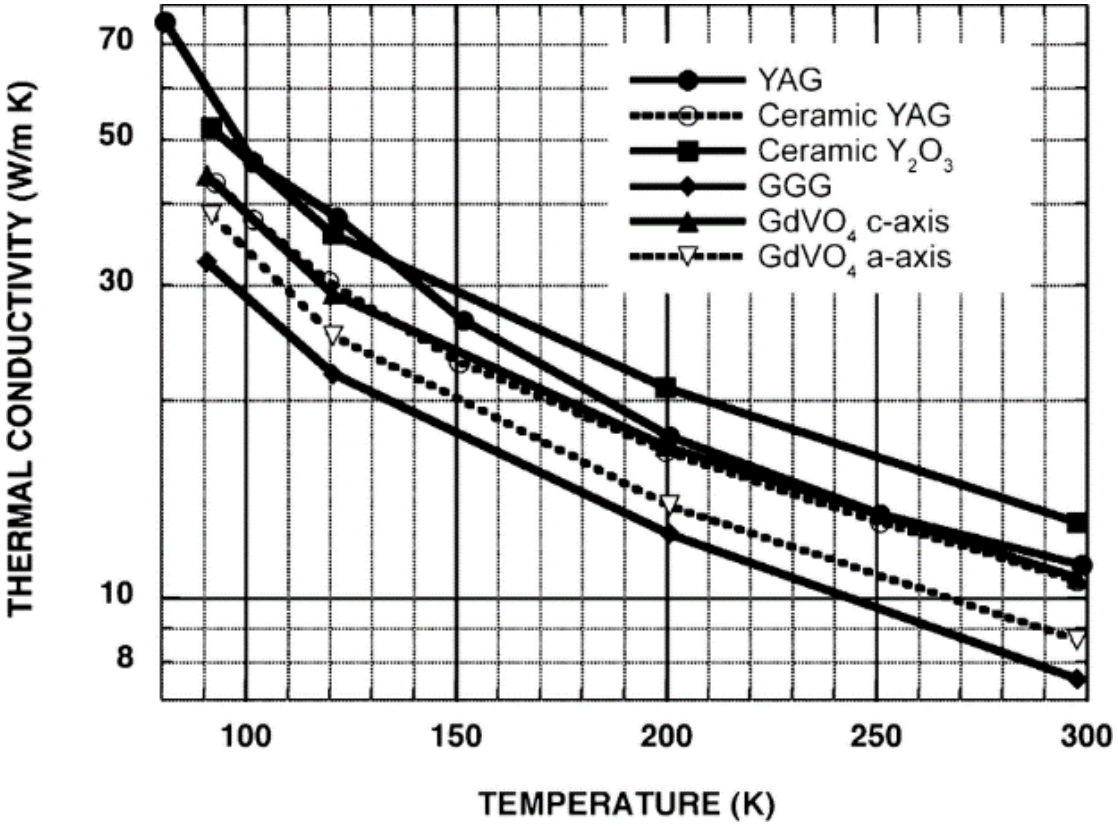

Figure 1.2. Diagram of thermal conductivities versus temperature of some laser gain medium host materials (from [41]). The thermal conductivities of Yb doped YAG crystals increase by 5x-7x at 77K compared with room temperature.

There are more advantages of cryogenic Yb:YAG amplifiers versus its room temperature counterpart. One of them is that the high Stark levels in lower manifold becomes thermally de-populated under cryogenic temperatures, as illustrated in Figure 1.3, changing Yb:YAG from a quasi-3-level system to a true 4-level system [41], which reduces the pump power required to achieve population inversion by at least 50%.

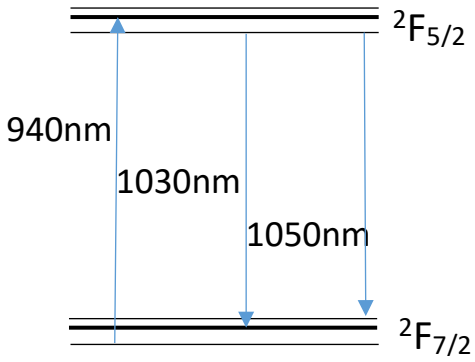

Figure 1.3. Energy levels of Yb3+ doped gain medium with the pump and lasing transitions.

Another advantage is, the emission cross section of Yb^{3+} is increased ~7x under liquid nitrogen temperature compared with room temperature, as shown in Figure 1.4. The saturation fluence F_s of the gain medium is given by:

$$F_s = \frac{\hbar\omega}{2\sigma} \tag{1. 1}$$

where ω is the angular frequency of the laser and σ is the stimulated emission cross section.

With upper state lifetime being not relevant in Q-switch and seeded scenarios, the saturation fluence reduces from 9.3 J/cm^2 to 1.9 J/cm^2 when temperature drops from 300 K to 77 K.

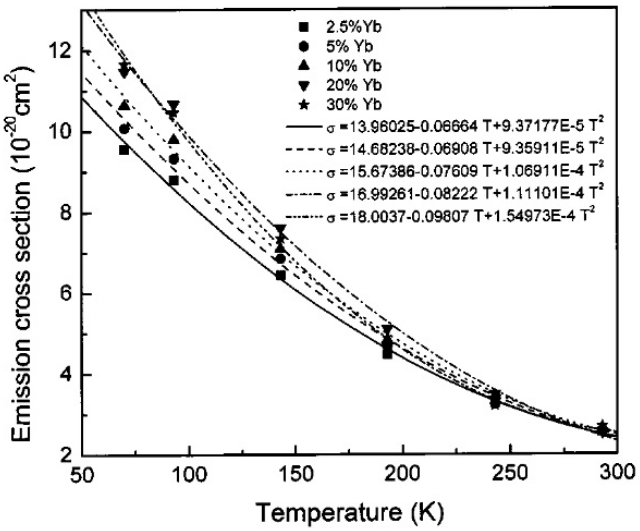

Figure 1.4. Emission cross-section of Yb^{3+} with different doping and different temperatures (from [43])

The lowered saturation fluence is in the range of a good quality optical thin film. This first allows the amplifiers to reach the saturation intensity and to extract the stored energy efficiently without damaging the optics; and secondly increases the single pass gain in the amplifiers, so the number of passes in power amplifiers can be reduced or enable the possibility to utilize thinner disk gain medium.

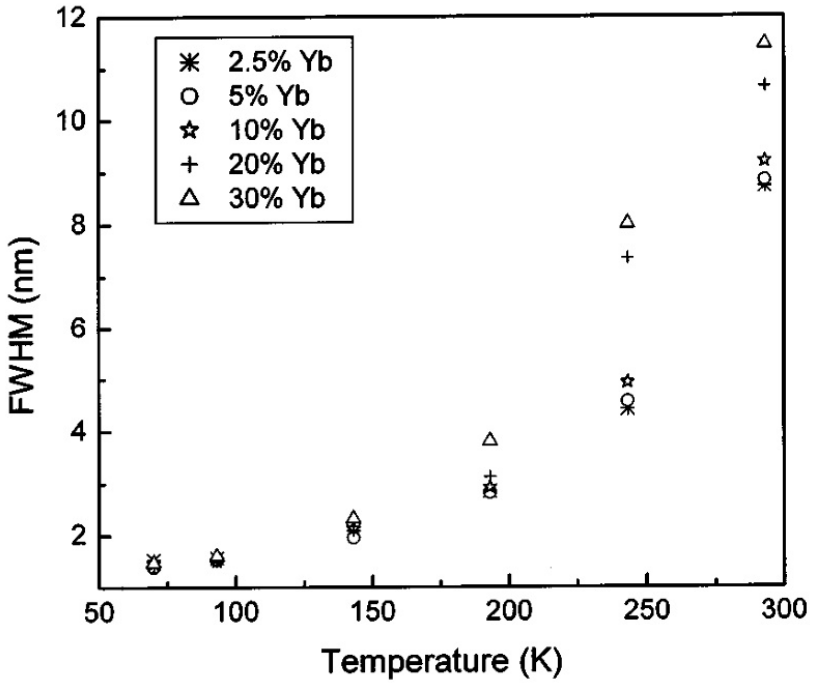

Figure 1.5. Line width of the 1030 nm line of Yb:YAG as a function of temperature in the 70-300 K for five different Yb doping levels. (from [43])

On the other hand, the major disadvantage for Yb:YAG as a laser gain medium, when under cryogenic temperatures, is a substantially reduced emission bandwidth. As shown in Figure 1.5, at room temperature the emission bandwidth of Yb:YAG is ~8 nm level, while under 77 K the bandwidth narrows to <2 nm. The narrowed gain bandwidth combined with gain narrowing effect that would occur in a laser amplifier, inhibits the ability of compressing the output from a cryogenic Yb:YAG laser system to shorter pulses in a CPA laser system. In our Joule-class Yb:YAG amplifiers at CSU, at the output of the amplification chain that includes two cryogenic

amplification stages, the bandwidth is typically 0.3-0.5 nm. The transform limit of such pulses are in the 3-5 ps level. This narrow bandwidth prevents CPA Yb:YAG amplifiers from reaching higher peak intensities as other gain medium choices such as Ti:sapphire and furthermore limits its application in research that requires femtosecond pulses. An efficient method for broadening the spectrum of Yb:YAG amplifiers would open many new possibilities for such amplifiers, such as their use to drive laser-based wakefield particle accelerators. Chapter 4 demonstrates nonlinear spectral broadening of Yb:YAG pulses of several hundred mJ energy by > 15x using gas-filled Hollow Core Fiber (HCF).

1.1.2 Joule-class Chirped Pulse Amplification Yb:YAG laser at CSU

This section describes the Joule-class, 10 Hz diode pumped Yb:YAG laser utilized as the test bed for all the experiments in the following chapters. Its cryogenically cooled, Yb:YAG CPA amplifiers are capable to output $\lambda = 1.03$ μm, 1.3 Joule pulses that can be compressed to 700 mJ, 5.6 ps.

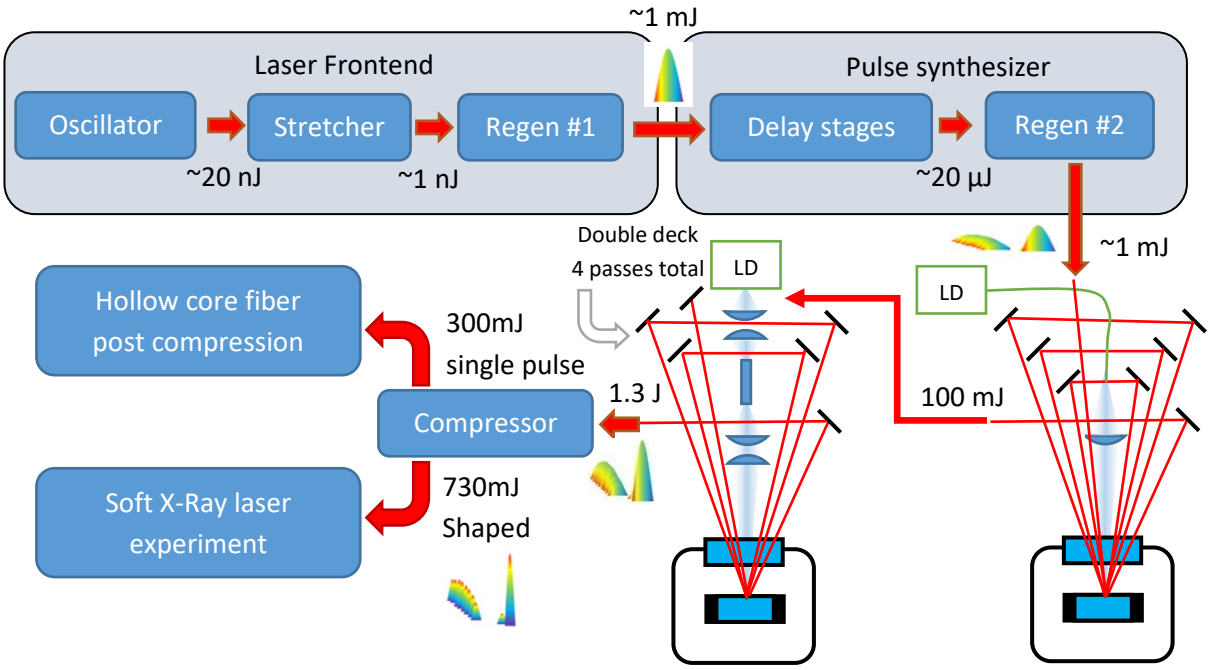

Figure 1.6. Layout of the Joule-class, diode pumped cryogenic Yb:YAG laser at CSU including the sub-systems for the applications discussed in this dissertation.

As shown in Figure 1.6, the frontend of the laser consists of a ytterbium-doped, potassium yttrium tungstate (Yb:KYW) oscillator, a grating stretcher and a room-temperature thin disk Yb:YAG regenerative amplifier. The details are discussed in [20]. Some modifications were made to suit specific needs for the applications that constitute this dissertation. In short, the oscillator is pumped by a 940 nm, 30 W continues wave (CW) diode. Mode-lock is achieved by a 3% semiconductor saturable absorber mirror (SESAM). A -1500 fs^2 chirped mirror is also added to the cavity to compensate the chirp added from the SESAM. The oscillator outputs ~20 nJ, 200 fs pulses at a repetition rate of 52 MHz, corresponding to 1 W average power. The output pulses from the oscillator are stretched to 180 ps by a grating stretcher. The stretched pulses are used to seed a thin-disk, room temperature Yb:YAG regenerative amplifier that is pumped by a 400 W quasi-CW (QCW) laser diode operating at a wavelength of 940 nm [20]. The regenerative amplifier outputs 1 mJ pulses. A clean-up Pockels cell placed after the regenerative amplifiers achieves a contrast of 2.5×10^{-5}.

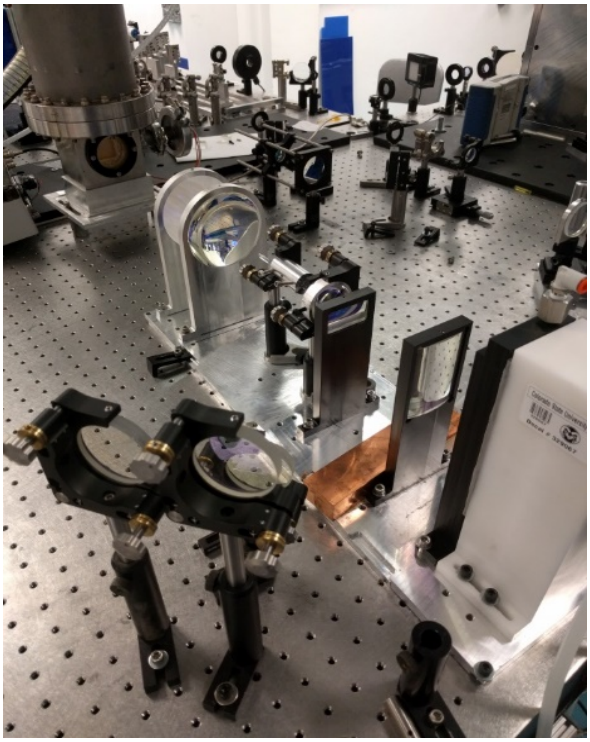

Figure 1.7. Structure of the 3rd stage amplifier. From top left to bottom right is the crystal with cooling tower, imaging system and the homogenizer, imaging system for the pump diode.

The output from the front end of the laser is used to seed a sequence of two cryogenically cooled diode pumped amplifiers. The structures of these amplifiers are described in [22]. Both amplifiers utilizes active mirror design, where a high reflector (HR) coating is put on the back side of the gain medium, and an anti-reflection (AR) coating in front of the gain medium facing the seeding beam. This design doubles the number of passes through the gain medium and allows the gain medium to be made thinner, thus improves cooling performance. The Yb:YAG crystals are cooled on the back side to 77 K by liquid nitrogen. Cr:YAG claddings are put on the side of the gain medium to mitigate parasitic lasing from amplified spontaneous emission (ASE). The 2nd stage amplifier is pumped by a 400 W QCW diode that is coupled to an optical fiber with 600 μm core diameter and then imaged onto the Yb:YAG crystal. This stage outputs ~100 mJ and then seeded into the 3rd stage amplifier, as shown in Figure 1.7, which is pumped by a 6000 W pulsed diode stack. The diode output is imaged into a 4 mm UV fused silica (UVFS) homogenizing rod and then imaged onto the crystal. The maximum output of the amplifier is 1.3 J at 10 Hz with a pulse duration of 200 ps. The output is then compressed by a grating compressor with a 70% efficiency to 5.6 ps and used for different applications. In the following parts of this section will give a brief introduction of the applications discussed in this dissertation and the apparatuses used in the experiments.

1.1.3 Pulse synthesizer for the generation of tailored pulse sequences

In order to achieve a tailored pre-pulse and pump pulse structure for soft X-Ray generation in Chapter 3, an arbitrary pulse synthesizer was designed and put between the frontend of the laser and high power amplifying stages, as illustrated in Figure 1.8. It consists of a controlled delay generator and a second regenerative amplifier introduced with the purpose to regain the lost energy and also to offer a stable mode for the subsequent amplifier chain.

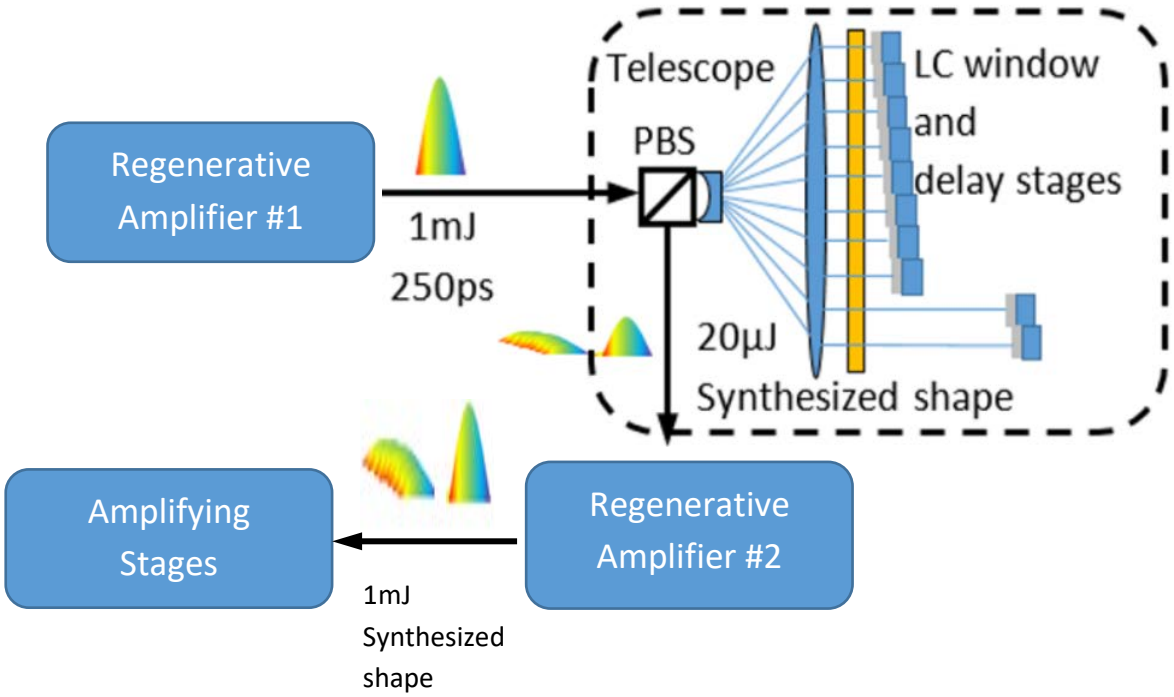

Figure 1.8. Schematics of arbitrary pulse synthesizer and corresponding amplifiers. The amplifying stages are the same plotted in Figure 1.6.

As shown in Figure 1.9, in the pulse synthesizer, the output of a first regenerative amplifier is expanded horizontally by ~ 200× by a series of cylindrical telescopes. A row of liquid crystal windows (12 total, 10 were used in practice during the experiments) controls the intensity of each channel. A delay stage is set after each window and is also on rails such that any arbitrary delay from 0-2 ns can be set individually. A polarizing beam splitter (PBS) separates the output and seeds the output into a second regenerative amplifier.

After the pulse synthesizer, two cryogenic Yb:YAG amplifiers are put in a series and amplifiy the pulse energy up to 1.3 J as described in [22]. After compression, an intensity cross-correlation between the synthesized pulse shape and a single compressed pulse is conducted to verify the pulse shape. Adjustments to the feedback system are made to compensate for the variations and drifts of the system.

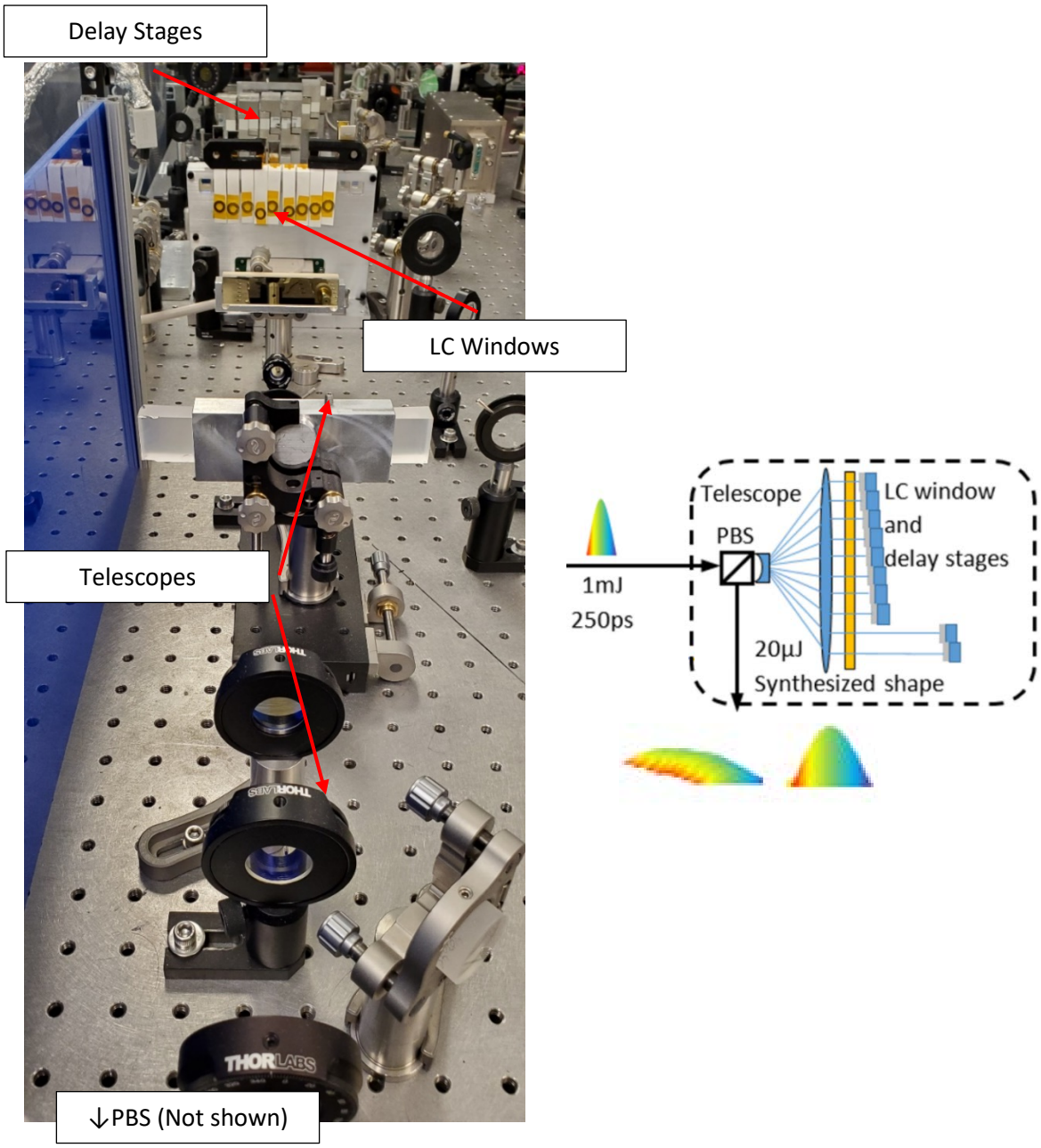

Figure 1.9. Layout of the arbitrary pulse synthesizer. The red arrows points at individual components illustrated in the schematics.

Note that there are certain limitations apply to the delay between the pulses in the synthesized shape. During amplifying, due to the stretched individual pulses have durations of 180 ps and can overlap each other when the delay between the pulses are set lower than ~200 ps, when such pulses are compressed, the resulting pulses are ~10% longer than their transform limits if the two pulses

are of same intensity. If there is a high contrast (> 10:1) between the two overlapping pulses, after compression, the higher energy pulse is usually unaffected while the lower energy pulse is compressed to ~15% longer than its transform limit, when the delay between the two is set at a measureable minimum of 10 ps. This effect gradually decrease when the delay between the pulses increase from 10 ps to 50 ps and becomes immeasurable when the delay is greater than 50 ps. The shaped compressed pulses do not carry significant higher order of dispersion and the grating compressor keeps its 70% efficiency with all different shapes synthesized and used in the experiments. If the pulses are >50 ps apart or with more than 10:1 contrast, the negative effects are minimal. This has been tested for energies from 10 mJ to 1 J for the synthesized shapes. A maximum usable contrast of 2.0×10^{4} is achieved within the compressed synthesized pulse shape and a noise level of 2.5×10^{-5} can be achieved when only one channel is seeding and all other channels are turned off.

1.2 Introduction of Laser induced damage test (LIDT)

1.2.1 Introduction of LIDT in dielectric materials

As discussed in section 1.1, the saturation fluence of Yb:YAG lowers in cryogenic temperature and is comparable to the damage threshold fluence of optical anti-reflection (AR) and high-reflector (HR) films. For efficient extraction, it is critical for those optical films to be able to not get damaged by repetitive exposure to laser pulses of near the saturation fluence of Yb:YAG. It is equally critical for the films to be robust enough to withstand the vacuum, cryogenic environment during operation, and the thermal, mechanical cycles in the cooling processes and the many rebuilding processes in the lifetime of the amplifier. During the development of the laser system described in this dissertation, it has shown that it is important to evaluate the performance of the optical coatings at exactly the conditions in which the Yb:YAG crystals operate. Which leads to the studies described in this section.

Laser induced damage processes in dielectric material from femto-second to nano-second pulses are generally described as a multi-photon ionization followed by electron avalanche ionization, which was proposed by Keldysh in the 1960s [44]. Free electrons are first lifted into the conduction band over the band gap of lattice by multiphoton process. The rate of free electron creation by multi photon ionization is given as $\frac{dn}{dt} \propto I^m$ (material) or $\frac{dn}{dt} \propto I^{On}$ (type n defect), in which n is the density of conduction band electrons, and I is the intensity of the laser pulse, and m, On are the number of photon required to initialize multiphoton ionization across the material bandgap and within a defect of type O. For SiO2 with bandgap E_g~9 eV and $\lambda = 1030\ nm$ or 1.2 eV photon energy, $m = 8$. For Yb:YAG with bandgap E_g~6.5 eV, $m = 6$. This mechanism dominants when the laser pulse is in the fs-sub ps range. An illustration of the SiO2 band structure is in Figure 1.10.

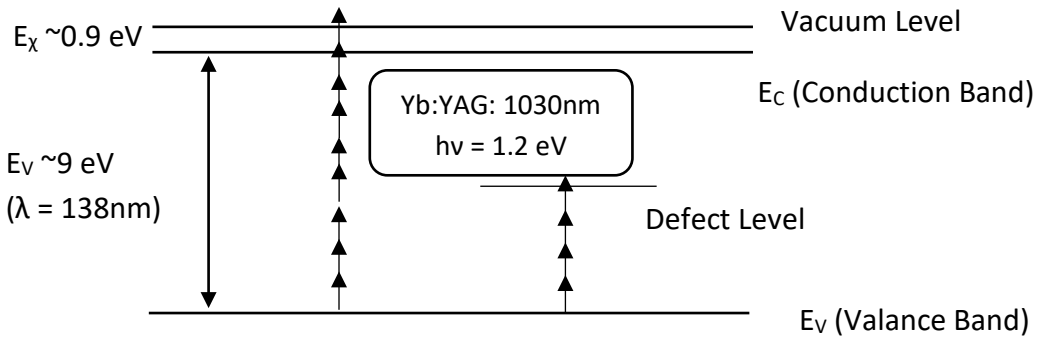

Figure 1.10. Band structure of fused silica, which is the top layer of the optical films used in the cryogenic amplifiers in [18], reconstructed from [45].

When the laser pulse is longer than ~1 ps, electron avalanche that has a $\frac{dn}{dt} \propto nI$ starts to dominate. The total rate equation then can be written as:

$$\frac{dn}{dt} = \alpha nI + \beta I^m \left(1 + \sum \gamma I^{On}\right) - \frac{n}{\tau} \qquad (1.2)$$

in which n is the electron density in conduction band, τ is the relaxation time for conduction band electrons. α, β are the coefficients of electron avalanche and multiphoton processes. And γ is the coefficient of the multiphoton process of individual defect type O_n.

When n reaches the critical density (2×10^{17} cm^{-3}), the material becomes highly absorbent and a large portion of the laser energy is transferred to the lattice, leading to a permeant damage.

1.2.2 Processes and corrections in LIDTs

During damage threshold tests, there is a need to distinguish thin film damage versus possible bulk damage induced by mechanisms such as self-focusing. The latter can be described as follows. The non-linear index of refraction caused by electrostriction is given by [46]:

$$n_2 = \beta\left(\rho\frac{dn}{d\rho}\right)^2 \tag{1. 3}$$

in which β is the compressibility, and ρ is the density of the material. This term is small enough in our test conditions due to the fact that the thin film layers are thin and $\frac{dn}{d\rho}$ for YAG is small. For UV fused silica this term becomes significant at ~25 mm and for YAG is ~140 mm [47], which is much thicker than the test sample and the Yb:YAG gain medium in the amplifiers.

Another more important self-focusing effect is Kerr lensing. For the case of a thin medium of thickness d and a relative long Rayleigh length, assuming a Gaussian beam with optical power P and radius w, the focal length of the Kerr lens is given by [46]:

$$f = \frac{\pi w^4}{4n_2 dP} \tag{1. 4}$$

Note that is n_2 is insensitive of polarization direction given Kleinman symmetry as <111> in YAG[48], which is the cut used in the amplifiers. The detailed calculation are discussed with the experiments described in Chapter 2.

Stimulated Brillouin scattering (SBS) is another factor that could cause bulk material damage in LIDT. This is a photon-phonon coupling process, or light scattering from acoustic waves in the medium. When incident light is strong enough and these Stokes waves see gain, the contribution from stimulated Brillouin scattering has to be considered. SBS is very prominent in bulk LIDT with UV fused silica[49], and can be detected in surface LIDT. The simplified model only consider the SBS beam travelling against the pump beam. Then the SBS gain satisfies:

$$g_B = \frac{k_s k_a n_s k_p p'^2}{2c\rho v_a \Gamma_B} \tag{1. 5}$$

in which k_s, k_a, k_p refer to wave vectors of Stokes, acoustic, pump beam, v_a gives acoustic velocity and Γ_B is the acoustic decay rate. For the gain material used in this dissertation, YAG, both longitudinal elasto-optic coefficient p', and electrostrictive contribution n_2 are small, and the SBS gain $g_B \approx 4.9 \times 10^{-12}$ m/W.

For a Gaussian beam profile and a Gaussian pulse temporal profile, the simplified model to calculate the SBS is to set the gain coefficient to 21 [49], corresponding to an equivalent 10% back reflection to the test beam with our sample geometry:

$$g_B F_{SBS} \tau_p L_m = 21 \tag{1. 6}$$

In which F_{SBS} is the threshold fluence of SBS, τ_p is the duration of the pulse, and L_m is the effective length of the material, which is the thickness of the material when the beam is collimated or near a long focus.

With $\tau_p \approx 200\ ps$ and $L_m = 1\ mm$, for YAG, $F_{SBS} = 85.7\ J/cm^2$, which is much higher than the test fluence and is not significant.

Also note that, in all LIDT tests described in this dissertation, the damages reported are surface damages. Previous studies of bulk laser damage in Yb:YAG crystals which have reported 1-on-1 laser induced damage threshold (LIDT) ranging from (100±10) J/cm^2 with 4 ns, 1064 nm

pulses [50] to over 1 kJ/cm^2 with 10 ns, 1064 nm pulses [51]. When scaled to 200 ps level using the square root of the pulse duration, as described in [52, 53], the bulk laser damage thresholds are significantly higher than the operating fluence of cryogenic Yb:YAG amplifiers (typically one-to-several J/cm^2) and are not the limitation in these systems. Instead, it is laser damage of the Yb:YAG surface that affects the performance of the amplifiers. De Vido et al. have shown the surface LIDT of uncoated, as-received polished Yb:YAG is ~10 J/cm^2 using 10 ns pulses at 1064 nm in a 1000-on-1 test configuration with a beam diameter (1/e^2) of 250 μm at ambient conditions [54]. The surface LIDT of Yb:YAG was improved by ion beam polishing processes [55]. De Vido et al. also showed that the cladding of the Yb:YAG as in an active mirror configuration does not modify the laser damage probability of the crystal [54]. Chapter 2 of this dissertation discusses the measurement of surface LIDT of Yb:YAG and optical coatings used in cryogenic Yb:YAG amplifiers in both ambient and conditions similar to the operating conditions in such amplifiers.

1.3 Laser-pumped plasma-based soft x-ray laser

Soft X-Ray light sources, both incoherent and coherent, are essential to a variety of applications both in fundamental research and in industry. An example is soft X-Ray microscopes, with its much better diffraction limit than optical microscopes, which are capable of imaging detailed cell structures such as chromosomes. Another example is X-ray-matter interactions such as the X-Ray diffraction pattern of DNA obtained by Rosalind Franklin and Raymond Gosling, leading to the discovery of its double helix structure. There are also applications still in development such as soft X-Ray lithography. However, there are certain applications where coherent soft X-Ray sources are needed, such as probing dense plasmas and X-Ray laser interferometers.

Coherent X-Ray emission was first demonstrated in free electron laser (FEL) [56, 57], in which synchrotron radiation from electrons with relativistic speeds is amplified. Since the parameters of FEL is highly tunable, it is able to function as a coherent light source with wide range of

frequencies, from microwaves to X-Ray. The downside of the FELs though, are definitely their size and accessibility. On the other hand, both plasma-based and high-harmonic-generation based soft X-Ray lasers (SXRLs) are also demonstrated, which can be driven by smaller, more accessible table-top laser systems [58-61]. Such techniques benefit from recent developments in diode pumped, high energy chirped pulse amplification (CPA) lasers [62, 63], where both high pulse energy and high repetition rate are obtained.

The conversion efficiency from the pump laser to SXRL emission has been improved by optimizing the pumping scheme to achieve SXRL. A single kilo-Joule class pulse was used to pump Ni-like Mo SXRL demonstrated by B. J. Macgowan in [64]. Soon, significant increase of conversion efficiency was demonstrated by J. Nilsen [65] and H. Daido [66] by adding a nano-second pre-pulse to the main pico-second pump pulse aiding plasma generation. This technique separated the generation and maintaining of the plasma, which required less energy, from pumping the plasma, which required a higher intensity, shorter pulse. The required total laser energy to achieve SXRL reduced to ~100 J level.

The next major leap in the pumping scheme of SXRL comes from utilizing the index of refraction of the plasma to align the gain region of SXRL with the absorption region of the pump. In order to achieve this, the pump laser pulse hits the target in a shallow grazing angle, and the technique is named as grazing incidence pumping or GRIP for short. Is was demonstrated in CSU [67], as shown in Figure 1.11, and later also by J. Tümmler [33]. With a proper GRIP angle, index of refraction change of plasma gradient aligns the turning point of the pump laser with the gain region of SXRL, which improves the absorption efficiency of the pump beam and reduces the pump pulse energy required to Joule level.

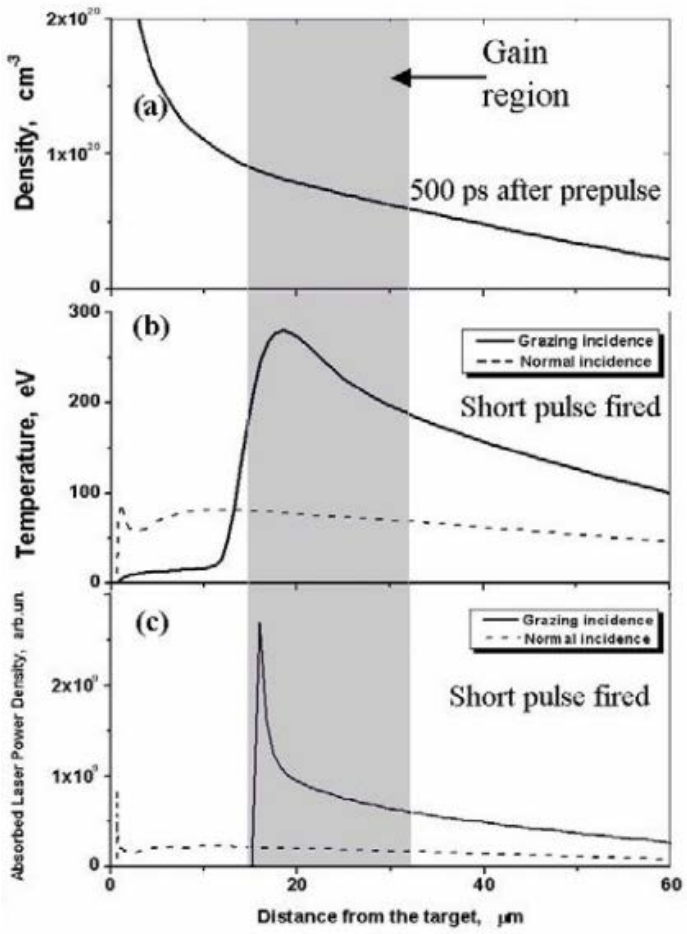

Figure 1.11. Demonstration of the GRIP scheme with the viewing angle along the SXRL gain axis. (a) shows the density of the SXRL ground state ions. (b) shows the electron temperature. (c) shows the absorbed pump laser energy distribution. The main gain region of SXRL is shown as the grey area, the solid and dashed line shows the absorbed pump power density distribution under GRIP and normal incidence pumping. It's clear the majority of the absorbed pump is in the gain region with GRIP [67].

The material chosen for SXRL generation is Molybdenum (Mo, Z=42). To generate SXRL, Mo is pumped to Ni-like (Mo^{+14}) and lasing occurs between the 4d-4p levels. The Ni-like SXRL scheme was proposed by Maxon et al. (1985) [68] and proved to lase by Lawrence Livermore National lab [64]. The energy levels of Ni-like Mo is shown in Figure 1.12. The ground state $|g\rangle$ of Ni-like Mo is $3d^{10}$, is mainly pumped to the upper state $|u\rangle = 3d^9 4d^1$ via collisional pumping

with selection rule ΔJ=0 with no obvious LS mixing, and lasing occurs between the upper sate and $3d^9 4p^1$ with λ = 18.9 nm.

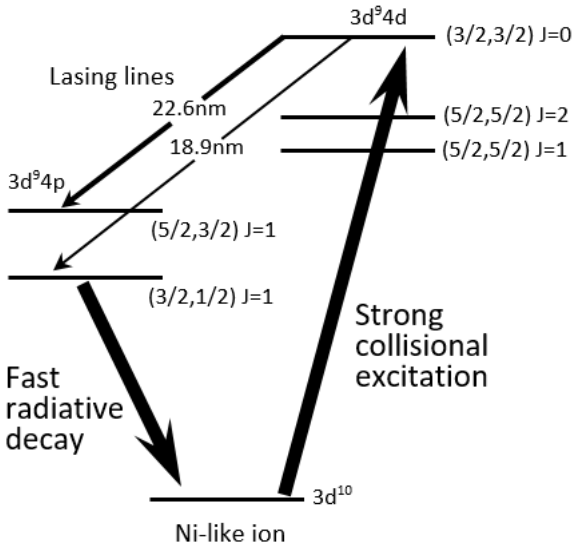

Figure 1.12. Energy levels of Ni-like Mo (Mo^{+14}). The population inversion is achieved between $3d^9 4d^1$ (J=0) and $3d^9 4p^1$ (J=1) levels.

Note that a longer lasing line of 22.6 nm between $3d^9 4d^1$ and $3d^9 4f^1$ with ~1 eV LS mixing is also observed in the experiments. S. Maxon also reported on this line [68], as well as pervious works here in CSU [69], but this chapter only discuss effects of the λ = 18.9 nm line.

The average power output of the SXRL has increased an order of magnitude by the advantage of higher repetition rate of the diode pumped lasers. With the Joule-class diode pumped Yb:YAG laser at CSU, we have previously reported a 0.15 mW average power tabletop SXRL lasing at λ = 18.9 nm with Ni-like Mo [24]. As illustrated in Figure 1.13, A tailored pre-pulse was utilized to improve the SXRL conversion efficiency (CE) by adding a long and weaker (~1.5 ns, 10^{-3} in intensity) and a short and stronger (5 ps, 10^{-1} in intensity) before the main pump pulse arrives. The late pre-pulse is shown on the leading edge of the solid blue line. The advantage of a tailored pre-pulse before the pump pulse in laser-pumped SXRL systems has been reported with different pre-pulse characteristics [70, 71]. Hydrodynamic and atomic physics plasma simulation has shown by

creating and heating the plasma with tailored pre-pulse prior to the arrival of the pumping laser pulse, a lower density gradient of the gain area in the plasma can be achieved, reducing diffraction loss of the linear plasma amplifier. The tailored pre-pulse also provides a better match of the areas with high density Ni-like ions and maximum electron temperature. As shown in the comparison of the pair (b)/(d) versus the pair (f)/(h) in Figure 1.13. Both of which favor a stronger lasing [24, 72]. In Chapter 3, a demonstration of higher conversion efficiency from pump laser to SXRL output, by utilizing both a synthesized early pre-pulse to aid plasma generation and to control plasma density gradient, and a pre-pulse close to the pump pulse for the better match of the collision pumping and ionization states.

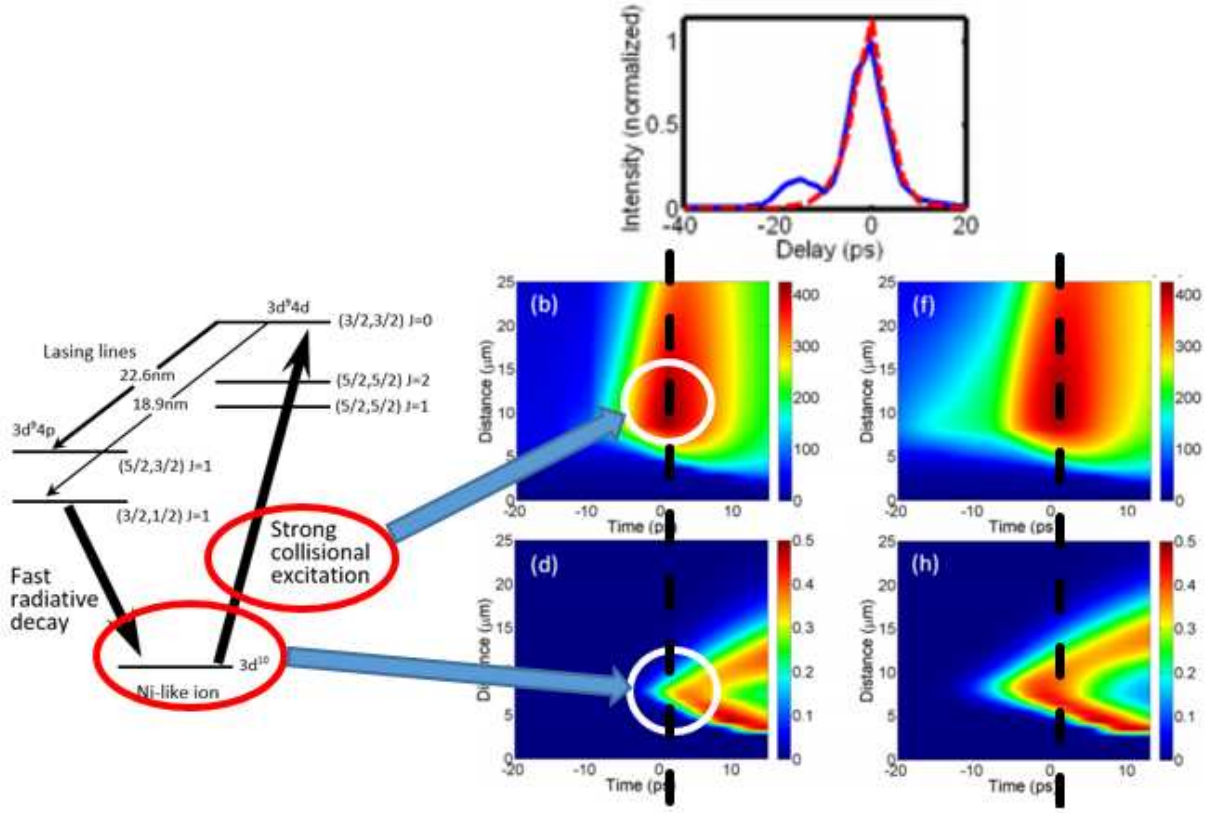

Figure 1.13. An illustration of simulated electron temperature map near the gain region of SXRL (labeled (b) and (f)), and density map of SXRL ground state $|g\rangle = 3d^{10}$ of Ni-like Mo (labeled (d) and (h)). (b) and (d) describe the case of single pump pulse (red dashed line in the pump scheme), while (f) and (h) describe the case with a tailored pre-pulse ~15 ps prior to the main pump pulse. With the tailored pre-pulse, there is a better match between the denser region of SXRL ground state around the region with high electron temperature. [20, 24]

1.4 Post-compression of Yb:YAG laser with hollow core fiber

This section of the dissertation will give a brief introduction of the background of non-linear processes in material and how they broaden the spectrum of laser pulses. The simulation and experimental results are presented in Chapter 4.

1.4.1 Self-phase modulation (SPM) and stimulated Raman scattering (SRS)

Self-phase modulation was first described as a frequency broadening effect in liquids with short pulse by F. Shimizu [73] in the 1960s. In the simplest model, SPM can be described as a result of Kerr effect, which is the variation of the index of refraction with intensity:

$$\Delta n = n_2 I \tag{1. 7}$$

in which I is the intensity of the beam and n_2 is the nonlinear index. Thus an intensity profile $I(t)$ will lead to the index of refection of material being:

$$n(t) = n_0 + n_2 I(t) \tag{1. 8}$$

This will lead to a time-dependent phase shift, where a positive chirp (or up-chirp, positive chirp will be used in this dissertation) will be added to the pulse. Hence, a transform limited or positively chirped pulse would acquire more chirp, and broaden its spectrum by propagating through a non-linear medium. The classic picture of SPM is that when the material has an instantaneous response $\Delta n(t) = n_2 I$, the output pulse would carry a self-phase modulation of:

$$\Delta\phi(t) = \frac{\omega}{c} n_2 I L. \tag{1. 9}$$

in which ω is the frequency of the injected pulse, n_2 is the non-linear index of refraction, and L is the length of the medium; and in which the frequency modulation is:

$$\Delta\omega(t) = -\frac{\partial(\Delta\phi)}{\partial t} \tag{1. 10}$$

which offers a broadened spectrum. The output spectrum is then given by the Fourier transform [46]:

$$|E(\omega)|^2 = \left|\int_0^{\infty} \mathcal{E}(t)\exp(-i\omega_0 t + i\Delta\phi(t))\right|^2 \tag{1. 11}$$

in which $\mathcal{E}(t)$ is the electric field in time domain and $E(\omega)$ is its Fourier transformation in frequency domain. This can be roughly described as a semi-periodic spectrum structure with a peak and valley pair for every 2π phase added. As shown in Figure 1.14 (a reconstruction from fig. 17.13 in [46]), when Fourier transformed back to frequency domain, new frequencies are generated on both sides of the initial frequencies by the phase modulation.

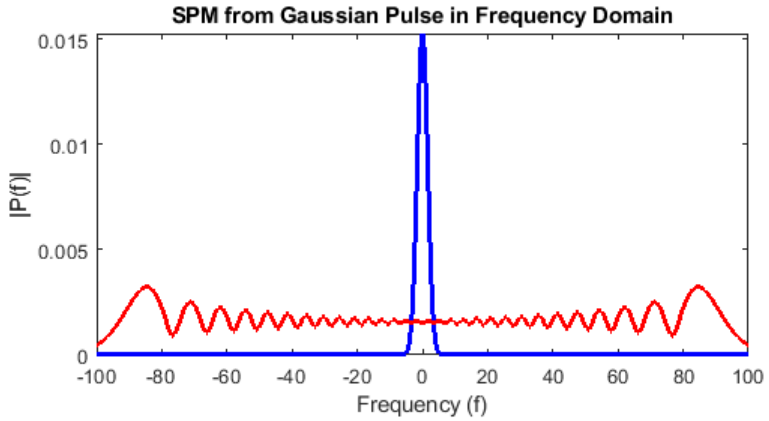

Figure 1.14. A Gaussian spectral profile before broadening (blue). Fourier transmission of the pulse with 30π phase delay generated by SPM (red). (reconstructed from fig. 17.13 in [46]).

The semi-classic picture of the SRS though, would require solving rate equations for the Stoke dipole oscillations corresponding to different energy levels, which is a different mathematical form than the SPM calculation. In order to simplify the simulation of the HCF broadening process, we take advantage of the fact that SPM and SRS processes are both $\chi^{(3)}$ non-linear processes. We start with writing the expansion of polarization in the material by the optical electric field:

$$\vec{P} = \varepsilon_0(\chi^{(1)}\overrightarrow{E(t)} + \chi^{(2)}\overrightarrow{E(t)^2} + \chi^{(3)}\overrightarrow{E(t)^3} + \cdots) \quad (1.\ 12)$$

in which the linear susceptibility $\chi^{(1)}$ is responsible for refraction and absorption, and the corresponding parts of third order susceptibility $\chi^{(3)}$ are associated with non-linear refraction and absorption. Since the two processes we discuss in this dissertation, SPM and SRS, belong to the same $\chi^{(3)}$ group, and we only consider two distinct frequencies with a specific order as shown in the top left of Figure 1.15, this simplifies the math by dropping the time dependent terms and terms describing other processes [74]:

$$\frac{8P(\omega_4)}{\varepsilon_0\chi^{(3)}} = \sum_{i=1,2,3} 3E_i^2E_i^* + \sum_{\substack{i,j=1,2,3 \\ i\neq j}} 3E_iE_jE_j^* \quad (1.\ 13)$$

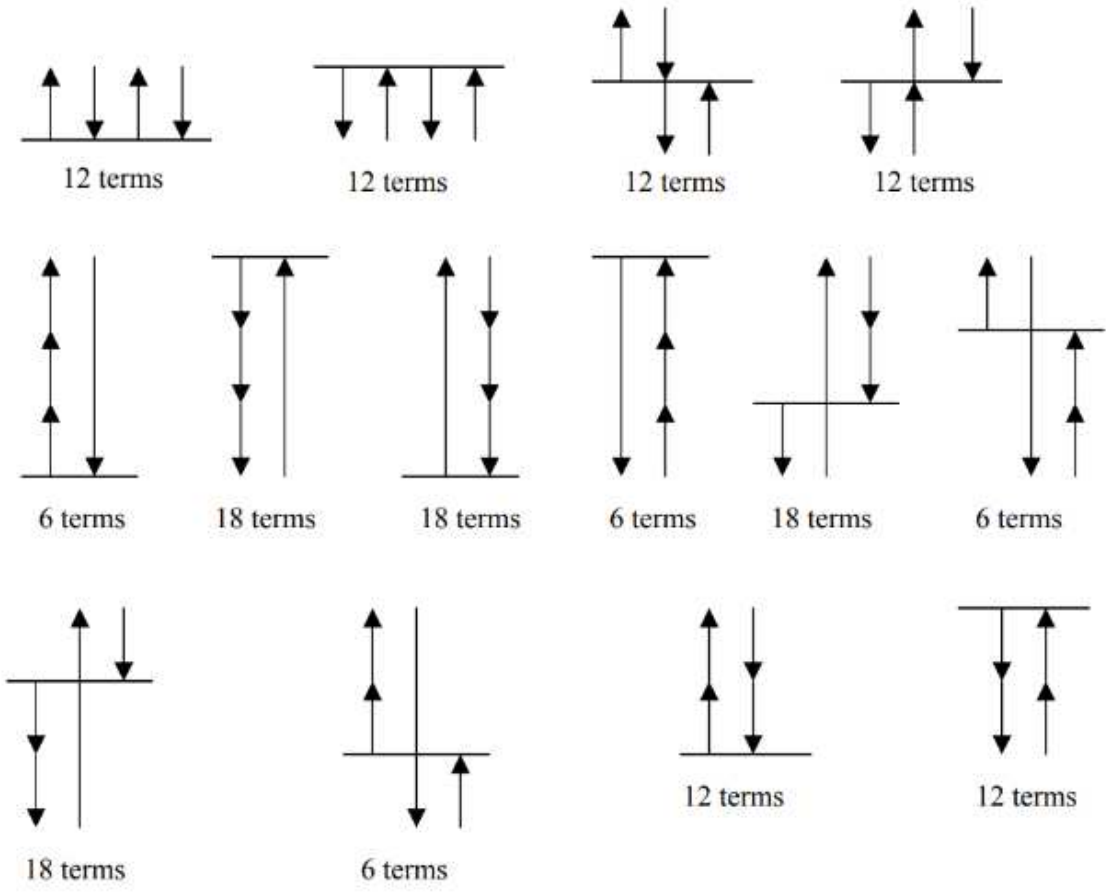

Figure 1.15. All the processes with different sign combinations in the $\chi^{(3)}\overrightarrow{E^3}$ non-linear term. From [74].

A complete assessment of $\chi^{(3)}\overrightarrow{E^3}$ term would require a full quantum mechanics picture expansion of all permutations of the electric fields of four-proton processes which include a total of 14 possible sign combinations and 168 terms [75, 76], as illustrated in Figure 1.15. Since both SPM and SRS are $\chi^{(3)}$ processes with an absorption/emission pair that follows the top left case in Figure 1.15. Such a generalized discussion of all these processes is not necessary and in the simulation, the two processes can be written in the same mathematical forms and can be calculated in the same loop. Although only SPM and SRS are the major contributors in the media and in the current simulation are the only two terms considered, there are also other possible cascade $\chi^{(2)}$ or $\chi^{(3)}$ processes occurs in the hollow core fiber. During experiments with nitrogen a weak magenta emission can be observed occasionally at the fiber exit with no apparent plasma generation or transmission loss in the fiber, indicating up to third order generation (THG) process or weak plasma generation can present, they are not major contributors and can generally be avoided. Therefore, for simplicity, THG will not be discussed in the simulation, while plasma generation and self-de-focusing will only be briefly discussed later in Chapter 4.

1.4.2 Mathematical model for SPM and SRS in the simulation

Now we construct the mathematical model for SPM and SRS in the simulation. Consider two groups of interacting photons that have frequencies of ω_a and ω_b, and only consider absorption/emission process such as SPM/SRS, like in the example shown in Figure 1.16. The total polarization can be written as [74]:

$$P(\omega_a) = \varepsilon_0 \left[\frac{1}{2}\chi^{(1)}(\omega_a)E_a + \frac{3}{8}\chi^{(3)}(\omega_a, \omega_a, -\omega_a)E_a^2 E_a^* + \frac{6}{8}\chi^{(3)}(\omega_a, \omega_b, -\omega_b)E_a E_b E_b^*\right] \quad (1.\ 14)$$

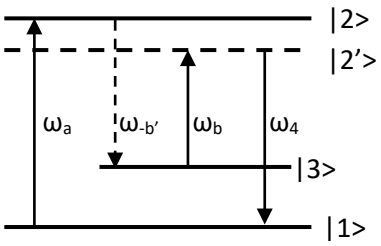

Figure 1.16. Quantum picture of a $\chi^{(3)}$ process. A total of 3 photons generate the 4th photon.

Note that in this dissertation we consider SPM and transient SRS processes being our only contributors in the non-linear processes hence the form of equation, if we define a complex index of refraction with an effective susceptibility χ_{eff}:

$$n + i\kappa = \sqrt{1 + \chi_{eff}} \tag{1. 15}$$

assume that all the non-linear terms are small, and only take first order of the Taylor series:

$$n + i\kappa \cong n_0 + \Delta n + i\frac{c}{2\pi\omega_a}(\alpha_0 + \Delta\alpha) \tag{1. 16}$$

in which the real part $n_0 + \Delta n$ describes the non-linear change of the index of refraction, and the imaginary part $\alpha_0 + \Delta\alpha$ describes the non-linear change of absorption/gain in the medium.

Also if we assume the perturbation of E_a from E_b is small in equation (1. 14), then χ_{eff} can be written as:

$$\begin{aligned}\chi_{eff}(\omega_a) = \chi^{(1)}(\omega_a) + \frac{3}{4}\chi^{(3)}(\omega_a, \omega_a, -\omega_a)|E_a^2| \\ + \frac{6}{4}\chi^{(3)}(\omega_a, \omega_b, -\omega_b)|E_b^2|\end{aligned} \tag{1. 17}$$

Substituting equation (1.17) into (1.15) we can write all the non-linear terms with related $\chi^{(3)}$ terms:

$$n_2(\omega_a, \omega_a) = \frac{3}{4\varepsilon_0 c (n_0)^2} \Re e \chi^{(3)}(\omega_a, -\omega_a, \omega_a) \tag{1. 18}$$

$$n_2(\omega_a, \omega_b) = \frac{3}{4\varepsilon_0 c n_0(\omega_a) n_0(\omega_b)} \Re e \chi^{(3)}(\omega_a, -\omega_b, \omega_b) \tag{1. 19}$$

$$\alpha_2(\omega_a, \omega_a) = \frac{3\pi\omega_a}{2\varepsilon_0 c^2 (n_0)^2} \Im m \chi^{(3)}(\omega_a, -\omega_a, \omega_a) \tag{1. 20}$$

$$\alpha_2(\omega_a, \omega_b) = \frac{3\pi\omega_a}{2\varepsilon_0 c^2 n_0(\omega_a) n_0(\omega_b)} \Im m \chi^{(3)}(\omega_a, -\omega_b, \omega_b) \tag{1. 21}$$

By defining irradiance:

$$I = \frac{1}{2} c \varepsilon_0 n_0 |E^2| \tag{1. 22}$$

the non-linear index of refraction and absorption terms can now be written as:

$$\Delta n(\omega_a) = n_2(\omega_a) I_a + 2 n_2(\omega_a, \omega_b) I_b \tag{1. 23}$$

$$\Delta \alpha(\omega_a) = \alpha_2(\omega_a) I_a + 2 \alpha_2(\omega_a, \omega_b) I_b \tag{1. 24}$$

in which the I_a term describes the local phase dispersion of the pump frequency leading to SPM and GVD processes; the I_b term describes the frequency shifting processes such as SRS.

At this point we have built the foundation of math of the simulation by making the SPM and SRS terms sharing same mathematical form such that we do not have to solve separate rate equations. Furthermore, by treating the Stoke-shifted I_b terms in the same form as I_a but also separate, they can be linked to absorption of the system that can be measured in various conditions. In the simulation, they can be stored in separate variables so energy conservation is automatically fulfilled. Section 4.2 of the dissertation covers how the transmission of HCF is modeled, the individual process contribute to spectrum broadening and their integration into transmission model, and how they are modeled in the simulation. The whole Chapter 4 describe both simulation and experimental results of the HCF broadening effect.

1.5 Brief outline of the following chapters

Chapter 2 describes the research towards the performance of the optical thin film used in the cryogenic Yb:YAG amplifiers. Since the saturation fluence of cryogenic Yb:YAG amplifier is close to the damage threshold fluence with the pulse width of 100-300 ps, the performance of such optical films, especially in vacuum and under cryogenic temperatures where the crystals operate, is critical for development of cryogenic Yb:YAG amplifiers. Ion beam sputtering (IBS) coatings have high potential in dealing with harsh environmental conditions due to its dense structure. The chapter describes the experimental measurement of laser damage fluence conducted in vacuum and cryogenic conditions with laser pulse width same as in the Yb:YAG amplifiers. Minimum loss of performance change of IBS coating in such conditions was demonstrated.

Chapter 3 demonstrats an improved technique of soft X-Ray laser generation with Yb:YAG laser. With an arbitrary pulse shape synthesizer, tailored pre-pulses both nano-second and pico-second prior to the main pump pulse can be generated and compressed by the CPA system. This pump scheme, together with grazing incidence pumping (GRIP), take both advantages of the lower density gradient in the X-Ray emitting plasma and a better match of collision pumping and correct level of ionization in the plasma. A 50% conversion efficiently increase from the pump laser energy into 18.9 nm soft X-Ray laser energy is reported compared with a single pre-pulse pump scheme.

Chapter 4 describes a recent development of the high energy cryogenic Yb:YAG laser system. In order to reach higher peak intensities in such lasers, broader bandwidth and shorter compressed pulses are required. Utilizing a hollow core fiber (HCF) charged with gas medium, 300 mJ, 10Hz, 0.28 nm, 8ps pulses from Yb:YAG amplifier are broadened to 3.7 nm and re-compressed to 460 fs by a grating compressor. The chapter discusses both a simulated HCF transmission with high energy pulses and non-linear effects and the experimental results of HCF broadening with high energy pulses from cryogenic Yb:YAG amplifiers.

Chapter 2 Laser induced damage in coatings for cryogenic Yb:YAG active mirror amplifiers

2.1 Introduction

This chapter reports results of a study of the laser induced damage threshold (LIDT) behavior of ion beam sputtered HfO_2/SiO_2 multilayer coatings on Yb:YAG. The LIDT tests were conducted with ISO:21454 laser induced damage test (LIDT) standard [77] and 1-on-1/N-on-1 protocols. In a 1-on-1 test, each test site is exposed to a single laser pulse with a set fluence and spot size, and then examined to verify whether permanent damage to the optical coating can be detected. Many sites (50 used in this work) are exposed to the same fluence and the results are presented as a damage probability at this fluence. By scanning the test fluence from low to high, the resulting damage probability, initially 0%, will gradually increase to 100%, showing the whole statistical behavior of the coating damage. During the N-on-1 test in this work, each test site is repeatedly exposed to the laser pulses with the set fluence until damage is identified by the *in-situ* microscope and image processing algorism. If damage is detected in the process, the number of shots to damage is recorded. If no damage is detected after N=1000 exposures, the site is then categorized as "no damage". As discussed in section 1.1.1, the saturation fluence of Yb:YAG at cryogenic temperatures is comparable to the laser damage threshold fluence of the optical thin films used in the amplifiers, thus optical films with higher damage threshold would offer better extraction efficiency and higher output energy in cryogenic Yb:YAG amplifiers as described in section 1.1.2.

Ion beam sputtering (IBS) coatings, due to its dense structure, are highly stable to environmental conditions such as temperature cycles. To evaluate the performance of such coatings in cryogenic amplifiers, LIDT tests were conducted at ambient, vacuum, and cryogenic conditions using 280 ps pulses at λ = 1030 nm. The 1-on-1 LIDT of antireflection (AR) stacks is found to be only slightly reduced under vacuum and cryogenic conditions, while that of high reflectivity (HR) stacks is

insensitive to environmental conditions within the uncertainty of the measurements. Cryogenic N-on-1 tests show the LIDT of the HR coating, 20.4 J/cm^2, is almost the same as in the 1-on-1 tests. Conversely, the cryogenic N-on-1 test of the AR coating shows damage at ~13 J/cm^2, a fluence lower than the of 1-on-1 tests. The AR damage behavior is found to be affected by imperfections at the Yb:YAG surface. By polishing the Yb:YAG substrate to a better finish with surface roughness of 0.15 nm root mean square (RMS) the N-on-1 LIDT has shown a more deterministic behavior and an increased onset damage threshold, when compared to the 5.8 nm RMS roughness measured from a 20-10 scratch-dig standard surface quality. Other surface treatment that improve the surface quality of the Yb:YAG can also be potentially used to improve the performance of the IBS coatings in the cryogenic Yb:YAG amplifiers. These findings show that high surface quality is required to increase energy extraction from active mirror laser amplifiers.

2.2 LIDT setup and damage site assessment techniques

The LIDT setup is shown in Figure 2.1. The Yb:YAG test laser generates 280 ps pulses at λ = 1030 nm. A single f = 30 cm lens focused the laser to test spot size $w_0 = 100 \pm 3$ μm (as e^{-2} irradiance) at normal incidence. Our measurement procedures followed ISO: 21254 laser induced damage test (LIDT) standard [77] and 1-on-1/N-on-1 protocols. A detailed description of the scanning technique is previously described in [78]. The pulse energy was varied by a half wave plate and a high-energy polarizing beam splitter. The pulse energy and w_0 were measured on every shot with a CCD camera located at a plane equivalent to the focal plane of the sample using a beam splitter. An energy calibration was performed with a calibrated power meter to determine the beam energy from the total number of counts on the image within w_0. The error bars on the fluence were computed taking into account the fluctuations in the laser pulse energy, the power meter accuracy, and the error in determining w_0.

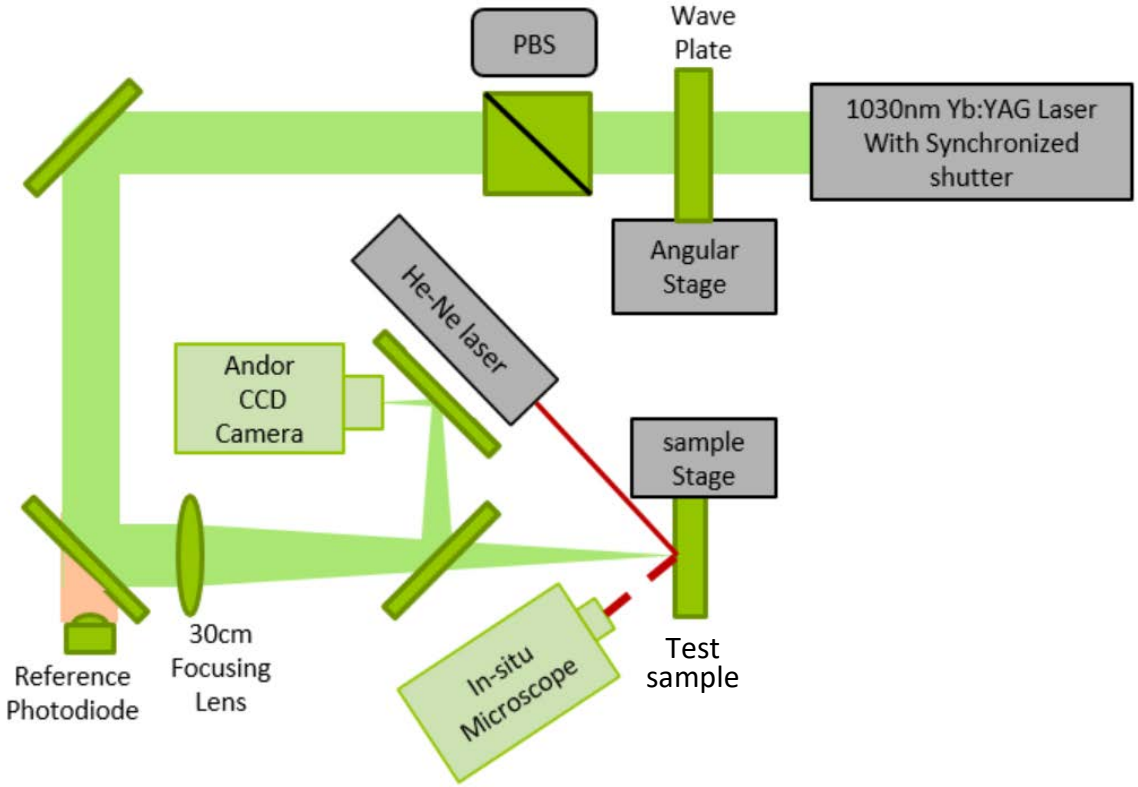

Figure 2.1. Layout of LIDT setup. The system follows the ISO:21254 test standard, the images captured by in-situ microscope is processed by the automatic damage site categorizing algorism described below.

An image of test site was recorded after each laser shot by an *in-situ* 100x, long working distance microscope. A control program utilizing a deep learning algorithm [16] analyzed each snapshot from the microscope and determined the damage status, as shown in Figure 2.2. The algorithm was trained from the previous damage test images categorized by human operators. A total of 60,000 pairs of damage site images taken before and after damage being detected were used in the training. The trained networks, as well as the control algorithm can be found in Appendix I. The results from the damage detection algorism were also verified *ex-situ* with a Nomarski microscope as the ruling criterion.

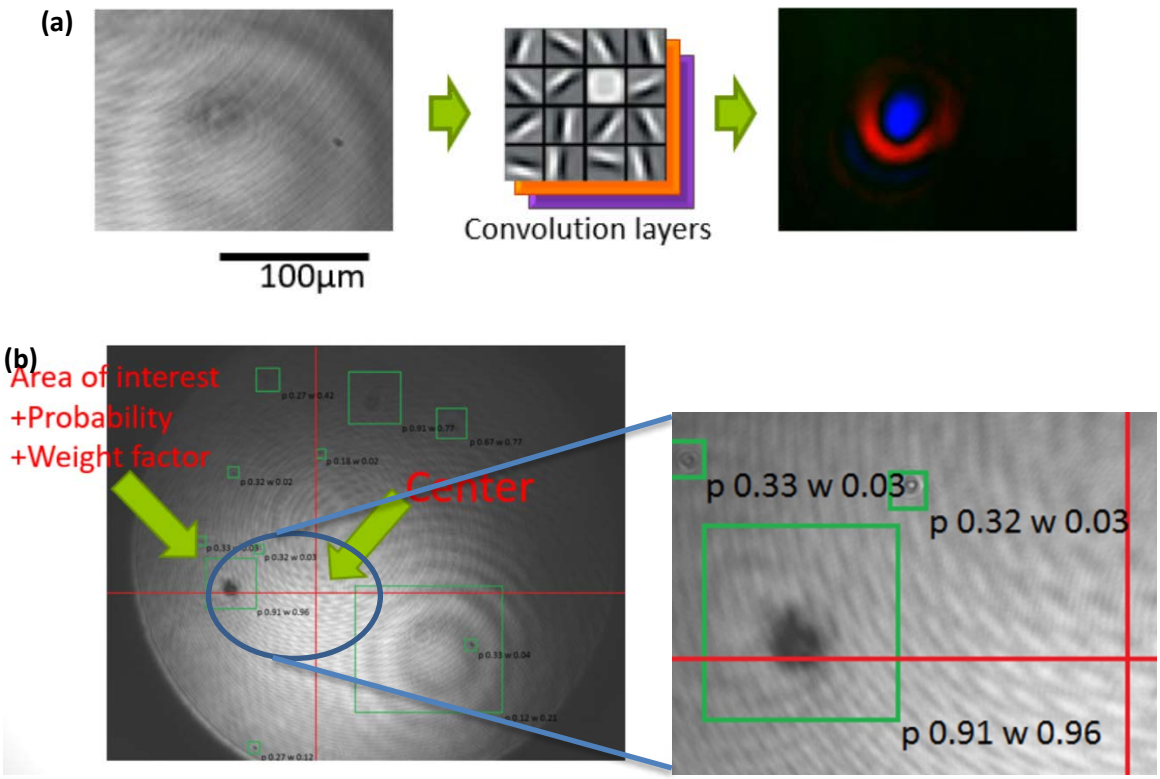

Figure 2.2 Illustration of the deep learning damage detection algorism. (a) The image from the in-situ microscope is processed by a convolution layer and then put through a neural network trained by previously manually categorized damage site images. A probability map is generated around each detected site, shown as the fake color image to the right. (b) Processed in-situ microscope image with each detected site boxed and plotted with evaluated probability and weight factor.

Surface damage is registered when any new feature, including a crater, color center or a crack is detected in the microscope images and confirmed by the human operator. In N-on-1 tests, consecutive shots are incident on one test site until damage occurs, then both the image of the damage site and the shot number at which damage occurred are recorded; or, when 1000 shots are reached and no damage is detected. A minimum of 20 sites were tested at any given fluence with 500 μm spacing following a raster scan from the bottom to the top of the sample to minimize cross site contamination from possible ablation materials.

2.3 LIDT experiment of Yb:YAG and coatings in various conditions.

The measurements were performed on <111> cut, 10 mm diameter, 1 mm thick Yb:YAG disks, with 3% doping density. The Yb:YAG crystals, manufactured by Scientific Materials Corporation, were polished to λ/20 surface flatness at 1030 nm, 20-10 scratch dig and measured 5.8 nm root mean square (RMS) surface roughness. Some of the crystals were super-polished to obtain a 0.15 nm RMS surface roughness. HfO_2/SiO_2 AR and HR coatings were deposited by ion beam sputtering (IBS) at conditions that result in an absorption loss at 1030 nm of about 10 ppm [79]. The coating structure along with the simulated electric field distributions are detailed in Figure 2.3 (b) and (c).

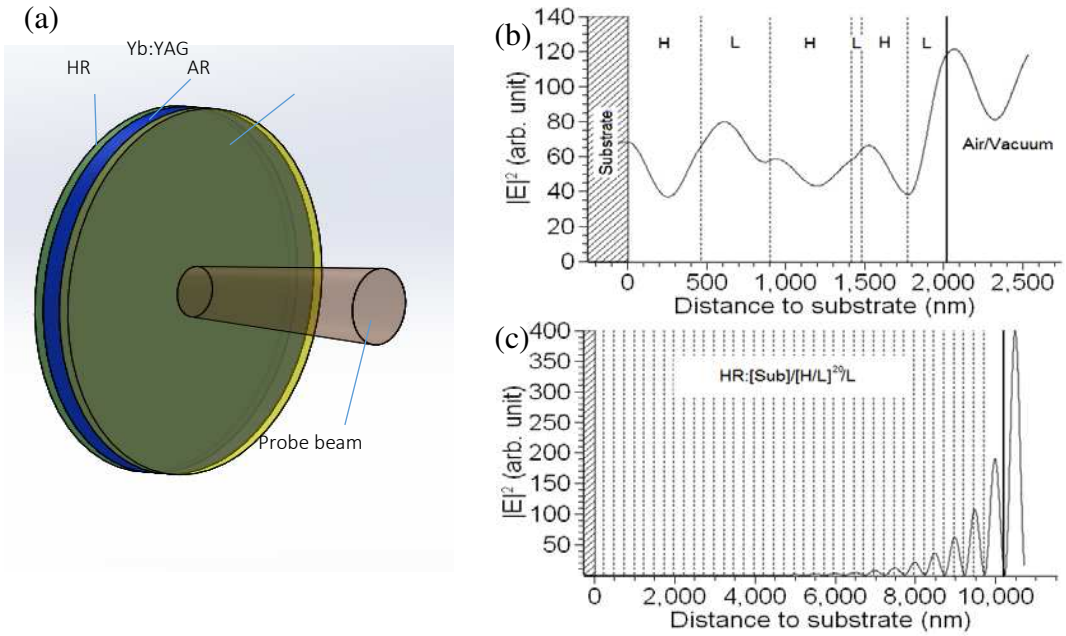

Figure 2.3. (a) Schematic of the damage tests on a coated Yb:YAG crystal. The designs of the AR and the HR stack are shown in (b) and (c), where H and L represent layers of high (HfO_2) and low (SiO_2) index of refraction. (b) and (c) also show the simulated AR and HR electric field distribution respectively.

The testing fluence was in the range of 0-60 J/cm^2. The discussion in section 1.2.2 already showed neither an index of refraction change caused by electrostriction nor Stimulated Brillouin

scattering (SBS) play a significant role in YAG based material under such fluence and pulse duration, but since the test sites are relatively small at $w_0 = 100 \pm 3$ μm, Kerr lensing correction had to be considered. From the discussion in section 1.2.2, for the case of a thin medium, the focal length of the Kerr lens is:

$$f = \frac{\pi w^4}{4 n_2 d P} \qquad (1.\ 4)$$

The test material Yb:YAG has a non-linear index of refraction $n_2 = 7.0 \times 10^{-20}$ m^2/W, both obtained with our own LIDT apparatus and also in [80, 81]. With test sample thickness $d = 1\ mm$, and maximum test fluence of 60 J/cm^2, the Kerr focal length is 5.3 cm. This equivalent lens slightly focuses the beam and leads to a +1.8% correction on the fluence for HR tests at the AR side, and a +3.7% correction on the reflected pulse in AR tests, which are implemented in the results later in this chapter.

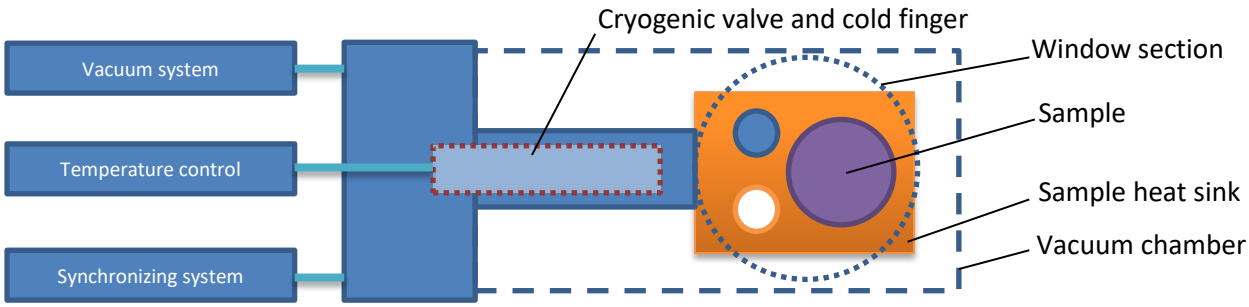

Figure 2.4. Structure of the cryogenic LIDT setup. The cold head is sealed in a vacuum chamber and the test sample is mounted on a copper heatsink. A through hole and a stainless steel insert are mounted in the same sample plane for calibrating laser pulse energy and microscope position.

The sample was mounted on a cryogenically cooled head in a small vacuum chamber mounted onto a 3-axis stage with 5 μm spatial resolution. The construction of the cryogenic cooling head/sample mount is shown in Figure 2.4. The incidence window on the vacuum chamber is AR coated on both sides offering 98.5% total transmission at λ=1030 nm, which is accounted for in the results. This window is set a few centimeters from the sample to avoid damage and to eliminate

self-focusing. The cryogenic head cools the sample to 77 K, and at this temperature the pressure in the chamber is (2.5×10^{-5}) Torr. Adequate damping time is added prior to a test to prevent the purging of the cooling head interfering with testing. A control damage test for each of the coatings deposited on UV Fused Silica (UVFS) was also performed at ambient conditions using the same setup.

2.4 Results and discussion

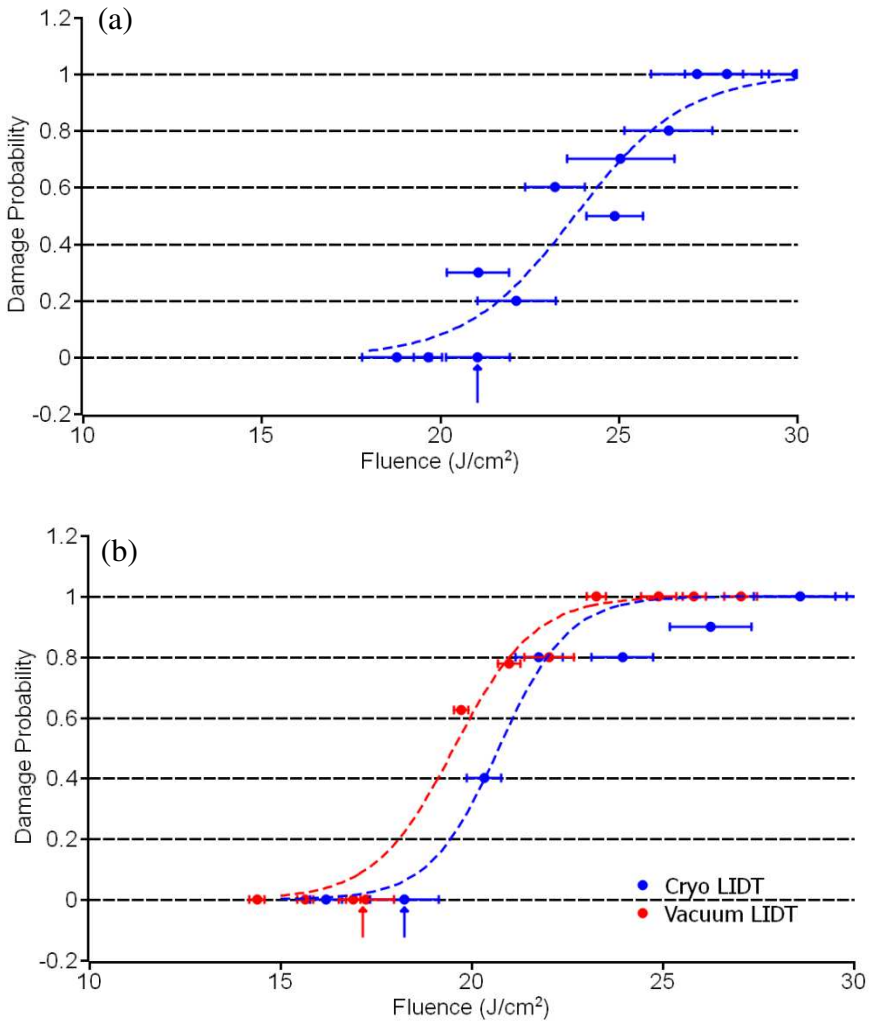

Figure 2.5. 1-on-1 damage probability curves for the standard polished Yb:YAG thin disk in: (a) air, (b) vacuum and cryogenic conditions. The arrows indicate the onset LIDT fluence. The fitted curves are visual guidelines.

Figure 2.5 shows the 1-on-1 damage probability of uncoated Yb:YAG crystals of 5.8 nm RMS surface roughness in air (a), vacuum and cryogenic (b) conditions. The surface LIDT of Yb:YAG in air was observed to occur at (21.1±1.1) J/cm^2. The LIDT drops to (17.2±0.9) J/cm^2 in vacuum, and remains at a similar value, (18.3±1.1) J/cm^2 at cryogenic conditions. The LIDT of the reference nearly superpolished fused silica (UVFS) substrates tested along with the Yb:YAG showed similar behavior. The UVFS LIDT reduced from (45±1) J/cm^2 in air to (38±1) J/cm^2 at cryogenic vacuum conditions. The LIDT values measured here are lower than those reported in the literature for 1-on-1 tests on bulk YAG with longer pulse duration [50, 51] when scaled to 280 ps using the square root of the pulse duration, as described in [52, 53]. The LIDT at the peak power level of the experiments can be reduced by Kerr lensing or stimulated Brillouin scattering. However in our case, neither one of these processes was observed due to the fact that in the 1 mm thick Yb:YAG samples the peak power level after Kerr lensing correction can not reach either the damage threshold of a bulk crystal or the threshold for stimulated Brillouin scattering [50, 51, 82].

Figure 2.6 shows the 1-on-1 damage probability curves for the AR and HR stacks deposited on the standard-polished Yb:YAG crystal tested at atmospheric ((a), (d)), vacuum and cryogenic conditions ((b), (e)). The AR has an LIDT of (20.1±0.4) J/cm^2 when tested in air and of (22.6±0.6) J/cm^2 and (20.4±0.6) J/cm^2 in vacuum and cryogenic temperature respectively. By comparison the LIDT of the AR coating deposited on a 5-10 UVFS is higher at (25.7±0.4) J/cm^2. This result suggests that the LIDT of the AR coating on Yb:YAG is affected by that of Yb:YAG substrate. In the AR the $|E|^2$ distribution is almost constant throughout the coating (Figure 2.3(b)), thus coating/crystal interface effects are important. A similar reduction of the LIDT of electron beam evaporated AR coatings on Yb:YAG respect to fused silica was observed by H. Wang et al. [83]. [83] also showed a ~50% decrease in the LIDT of the electron beam evaporated AR on Yb:YAG at cryogenic temperatures, in contrast to our results on the IBS AR on Yb:YAG.

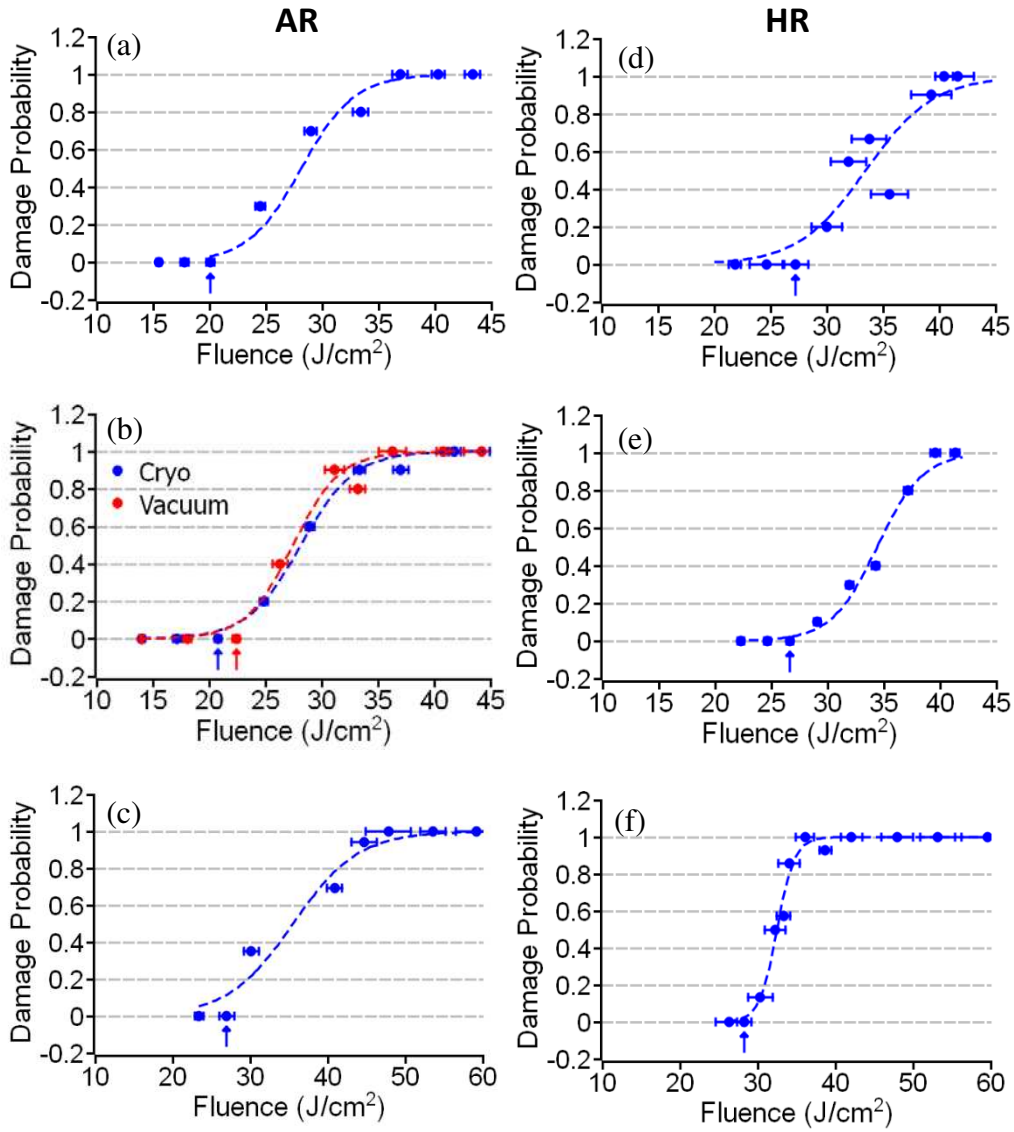

Figure 2.6. 1-on-1 damage probability curves for: AR coatings on Yb:YAG in (a) air, (b) vacuum and cryogenic conditions; and HR coatings obtained in (d) air and (e) cryogenic conditions. (c); (f) Control AR and HR on UVFS in air. The LIDT fluence is indicated by arrows. Dotted lines are guides to the eye.

The 1-on-1 tests of the HR films on Yb:YAG and on the control UVFS were conducted from the coating side, as otherwise the AR-coated surface damaged first. The HR coating LIDT was determined to be (27.4±1.3) J/cm^2, independent of the substrate and of the environmental conditions. In the HR, the amplitude of the electric field is maximum at the air/surface interface

and negligible at the coating/crystal interface (Figure 2.3(c)), making the LIDT insensitive to the substrate surface conditions.

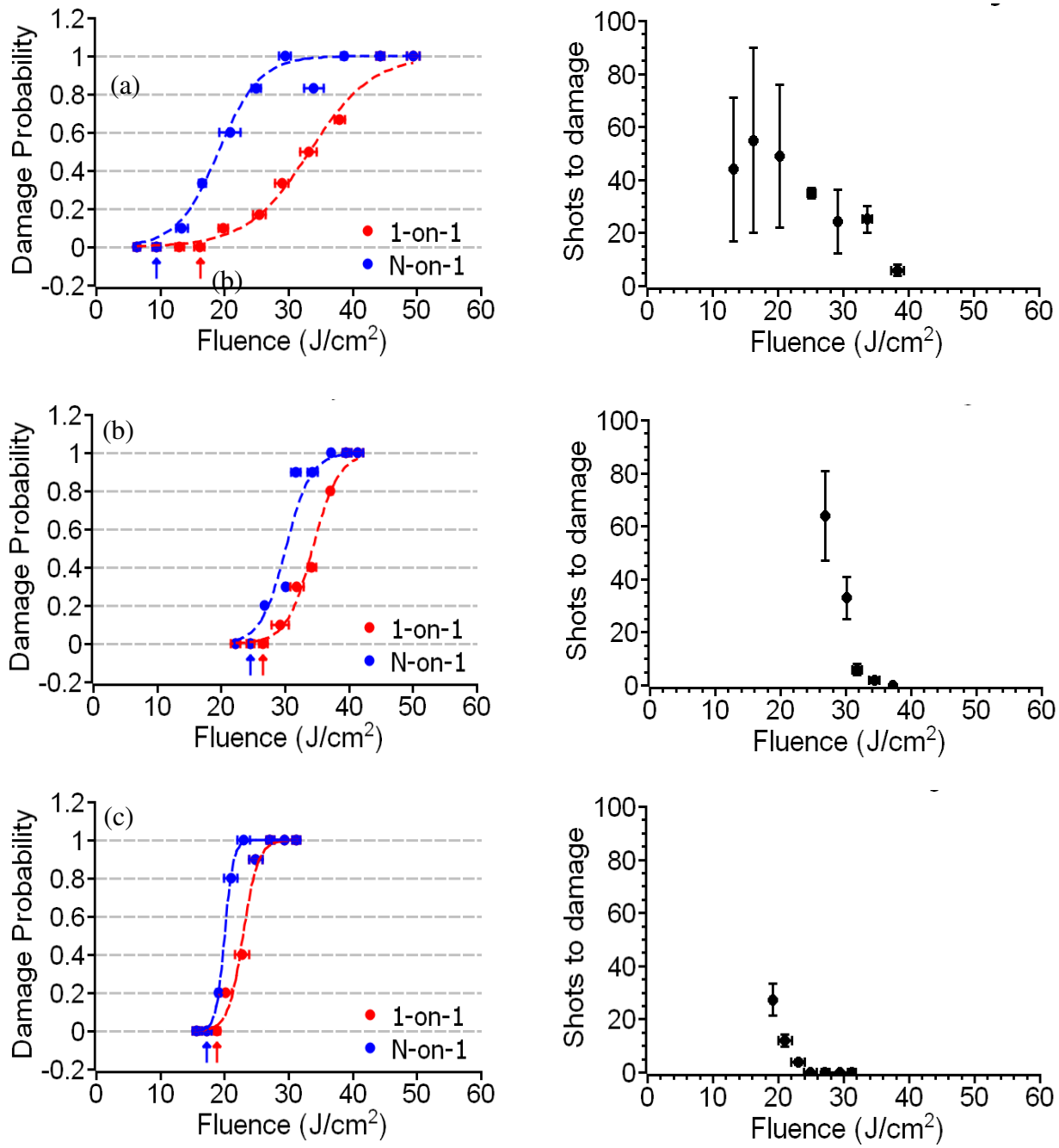

Figure 2.7. Damage probability vs fluence comparing 1-on-1 to N-on-1 damage behaviors at 77 K for (a) AR and (b) HR coatings deposited on standard polished Yb:YAG; (c) standard polished Yb:YAG. The number of shots to damage are plotted on the corresponding graphs on the right. The error bar represents the standard deviation of the number of shots before damage at the tested fluence.

The damage probability vs fluence behavior for N-on-1 tests on the Yb:YAG, AR on Yb:YAG and HR on Yb:YAG at 77 K contrasted to the 1-on-1 results are shown in Figure 2.7. The cumulative effect of multiple exposures before optical breakdown is observed in all three surfaces [84]. However, the N-on-1 onset of damage (the fluence where the damage probability transits from 0% to non-zero) in the HR films and bare standard Yb:YAG crystals is close to the 1-on-1 LIDT. It takes ~30 shots at ~20 J/cm^2 on Yb:YAG and ~70 shots at ~27 J/cm^2 on the HR on Yb:YAG to observe the onset of damage during the N-on-1 tests. In both cases a sharp decrease in the number of shots to damage as a function of fluence is observed. Conversely, the behavior of the AR on standard Yb:YAG shows a wider difference between single (18 J/cm^2) and multi-shot damage thresholds (13 J/cm^2) and a greater variation in the number of shots before damage from site to site in multi-shot tests, as illustrated by the wide error bars. The large error bar is due to a unique bimodal behavior in which the AR films would damage within 2-3 shots or could sustain ~ 60 shots before damage. Comparison of the damage behavior of AR and HR coatings on N-on-1 tests supports the conclusion that the AR LIDT is highly statistical and largely dominated by random defects on the coating/crystal interface.

The role of polishing-related defects at Yb:YAG/AR interface is evidenced from the cryogenic N-on-1 test of AR damage of Figure 2.8. In a standard polished Yb:YAG with 5.8 nm RMS surface roughness the variations in the number of shots to damage of the AR coating at a given fluence are large, as shown by the wide error bars in the figure. Instead when the Yb:YAG surface is polished to 0.15 nm RMS roughness, the AR coating damage behavior becomes more deterministic. The average number of shots for the damage to occur in across the N-on-1 test fluence are higher with lower standard deviation. The change in statistics indicates the better polish of the Yb:YAG substrate removed a high portion of the type of defects causing damage within a couple of shots after the N-on-1 test started, which is also the major failure mode of such coatings installed in an amplifier.

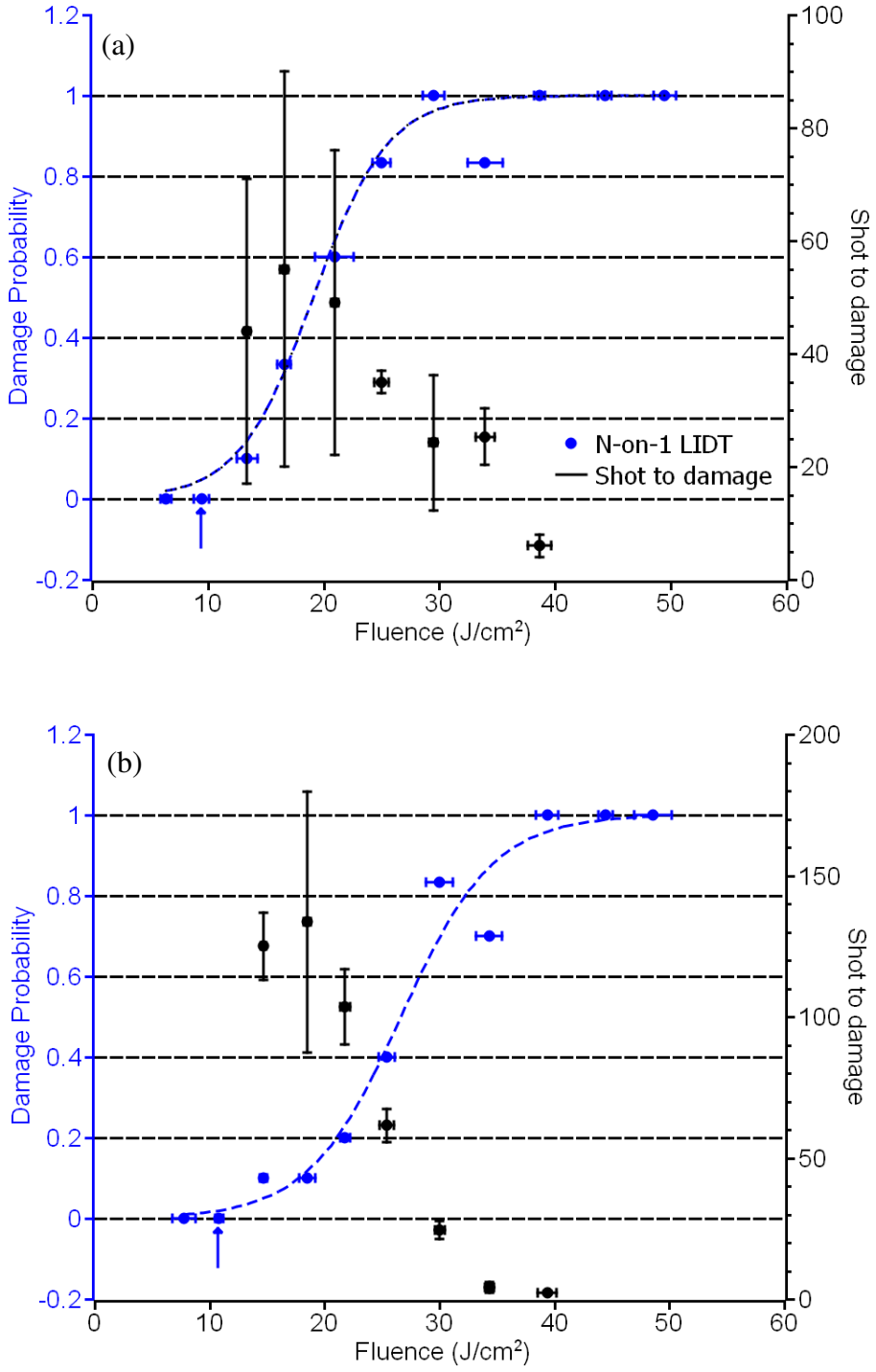

Figure 2.8 N-on-1 cryogenic results showing the damage probability vs fluence (blue symbols) and the number of shots to damage (black symbols) for the AR coating deposited onto (a) standard polished and (b) nearly super-polished Yb:YAG.

2.5 Discussion

While the cryogenic N-on-1 tests are more representative of the operation of the HR/Yb:YAG/AR structure in the active mirrors of high energy solid state amplifiers and present lower damage threshold, there can be other factors that influence the performance of an amplifier besides the number of shots. The results show that the quality of the Yb:YAG/coating interface has a significant effect on the onset damage of the AR coating, which is the weakest component in the active mirror. This was also observed by H. Wang et al. [83]. Recent results also showed that the N-on-1 LIDT of IBS AR coatings deposited on adhesive-free bonded crystalline Yb:YAG damage at the same fluence as the monolithic uncoated structure [54]. Imperfections at a coating/substrate interface cause local field intensification that, as shown in single layers of HfO_2 deposited on UVFS substrates, are environmentally dependent and reduce the LIDT [85].

The results of this chapter are significant in that they show environmental conditions do not significantly affect the LIDT behavior of IBS coated Yb:YAG crystals when tested at 280 ps pulse duration. Moreover, the results identify the surface preparation of the Yb:YAG as critical to raise the LIDT of Yb:YAG cryogenic active mirrors. Strategies that would remove subsurface defects from the Yb:YAG, such as ion bombardment and chemical polishing [55, 86] or that prepare the first coating layer by sequential deposition and etching steps [87], may be beneficial to increase LIDT. In combination, these strategies will contribute to improve the laser damage resistance of Yb:YAG cryogenic active mirrors to achieve higher energy extraction from solid state Yb:YAG amplifiers.

Chapter 3 Optimized laser-pumped plasma-based soft x-ray laser with a pump pulse synthesizer

3.1 Introduction

This chapter discusses the demonstration of a tabletop SXRL driven by a compressed, picosecond CPA laser with fully synthesized temporal profile pulses. For this purpose we modified our diode pumped Yb:YAG to be able to generate pulses of arbitrary shape. The synthesizer is capable to synthesize waveform of 0-4 ns duration formed by 10 individual channels with 10^4 contrast. When fully optimized, the synthesized pump pulses increased the optical to SXR conversion efficiency from a Ni-like Mo SXRL lasing at λ = 18.9 nm by 50%. A best of 2.4 ± 0.3 uJ EUV output was recorded with 730 mJ of pump energy on target. The added synthesizer will open new applications to existing SXRL system since it could increase the EUV output of a plasma amplifier without the need of increasing the required pump energy.

Among the table-top soft x-ray sources, plasma-based soft x-ray lasers (SXRLs) have the advantage of producing high pulse energy that allows for example single shot imaging of dynamic phenomena [12, 13, 88], ablation for nanoscale resolution atomic and molecular composition imaging [89] and nanomachining. Table-top laser-pumped collisional SXRLs are implemented using solid targets [90]. They have the advantage of reaching shorter wavelengths [61, 91, 92]. A particularly advantageous implementation of solid target table-top SXRLS is the use of transient excitation [93] at grazing incidence [69, 94]. In this scheme a pre-pulse is used to create a plasma containing highly charged ions (Ni-like or Ne-like) that is allowed to expand to reduce the plasma density gradient before it is rapidly heated by a picosecond pulse to generate a transient population inversion by collisional electron impact excitation, and gain. Grazing incidence pumping allows to use refraction of the pump pulse to efficiently heat the plasma region with optimum density and density gradient for SXRL amplification, with the additional advantage of providing quasi-

traveling wave excitation of the short lived laser upper levels. It was demonstrated that instead of using a single pre-pulse, the addition of long pre-pulse pedestal, or of an additional picosecond pre-pulse closely preceding the main pump pulse [70, 90, 95] can significantly improve the SXRL output. This additional picosecond pre-pulse allows to speed up the ionization such that a large population of the lasing ion specie of interest (Ni-like of Ne-like) is present at the time of maximum electron temperature, which occurs shortly after the arrival of the main picosecond pump pulse. Having larger density of lasing ions at the time of maximum electron temperature results in higher gain, leading to increased SXRL output pulse energy. It is foreseeable that additional degrees of freedom in shaping the pumping pulse will result in further SXRL performance improvement.

Here we explore pumping plasma-based soft x-ray lasers with pulses of arbitrary shape where optimization can further increase the SXRL output pulse energy and efficiency. With this purpose we introduced an arbitrary pulse shape synthesizer into our CPA pump laser. The synthesizer is capable to create tailored waveforms within a time span between 0-4 ns by adjusting the amplitude and relative delay of 10 individual channels with 2.0×10^4 contrast. When optimized, a 50% increase in conversion efficiency (CE) was achieved in a Ni-like Mo SXRL laser operating at $\lambda = 18.9$ nm, as compared with our previous reported result obtained with the same pump pulse energy. The use of synthesized pulses has significant further potential to increase the output of laser pumped plasma-based SXRL without the need of increasing the pump laser energy. This in turn could open new opportunities for the use of SXRL systems both in technological and research applications, The approach demonstrated here is also applicable to plasma-based SXRL with different gain medium, including those that produce lasing at shorter wavelengths [91].

3.2 Experiment

The SRXL used in this demonstration operates at a wavelength of 18.9 nm in the $4d^1S_0$ - $4p^1P_1$ transition of Ni-like Mo by irradiation of a Mo slab target at grazing incidence. The pump laser is a 10 Hz repetition rate diode pumped, $\lambda = 1030$ nm, CPA Yb:YAG laser, schematically represented

in Fig. 1 and described in [96]. The seed pulses from a mode-locked Yb:KYW are stretched to about 300 ps and amplified to ~1 mJ by a room temperature Yb:YAG regenerative amplifier. These pulses are in turn used to seed an arbitrary pulse shape synthesizer. The pulse synthesizer shapes the pulses by separating the beam through up to 10 channels. Each channel has its own delay stage that allows for the selection of arbitrary delays between 0-4 ns. A set of liquid crystal windows controlled by a computer program is placed in front of each channel to regulate the intensity with 10^4 contrast and ±5% stability. The outputs of the different channels are then combined to seed a second regenerative amplifier in order to recover the lost pulse energy and obtain good beam quality. The second regenerative is tuned such that the strongest pulse in the synthesized group is amplified to ~60% of saturation to make sure its sensitivity to the pulse shaping. This second regenerative amplifier ensures that all the individual pulses within the synthesized waveform share the same spatial profile, can be equally compressed by the optical grating compressor, and can all be focused to form a single narrow line focus. The pulse train is subsequently amplified by a cryogenic Yb:YAG pre-amplifier to energies up to 100 mJ. In order to be able to pump a SXRL, a 2^{nd} cryogenic amplifier further amplifies the synthesized pulse to 1.1 J, before they are compressed to 7.1 ± 0.6 ps FWHM by a grating compressor. The compression limit is up to ~ 20% longer than the transform limit depending on the pulse shape selected, due to the alteration in the spectral profile during amplification, during which the individual stretched pulses have pulse width of ~300 ps and overlap in time. Figure 3.1 (a) shows the construction of the pulse synthesizer and (b) shows how the pulse synthesizer is inserted in the laser system. The input seed pulse from the 1^{st} regenerative amplifier is expanded ~100x in the horizontal direction by the two-stage cylindrical telescope and then is rotated in polarization by the combination of the liquid crystal windows and the waveplate. The polarizing beam splitter then selects the synthesized pulse train and is used to seed the 2^{nd} regenerative amplifier for recovery of the lost energy and better beam quality. Technical details of the pulse synthesizer can be found in [96].

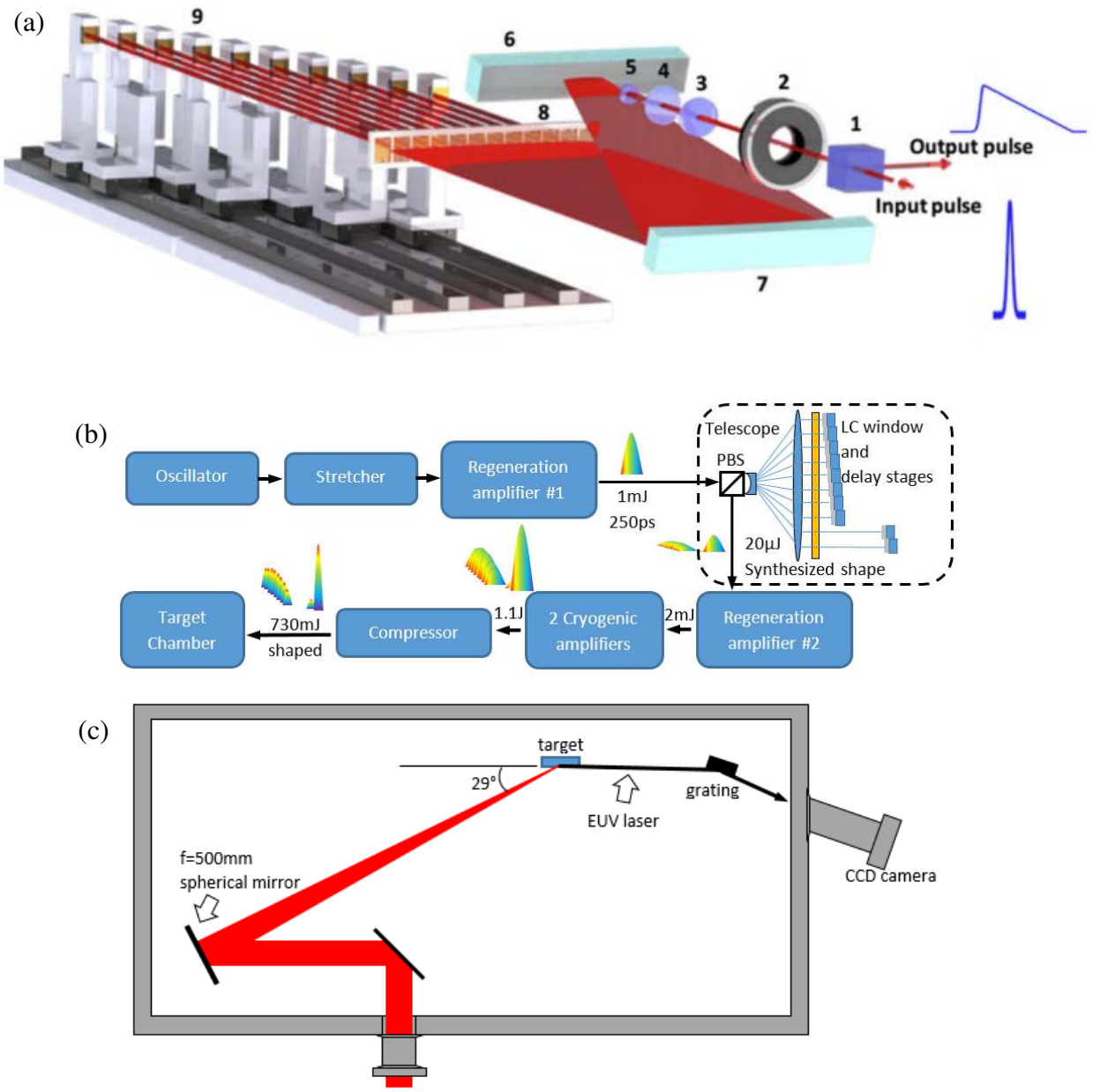

Figure 3.1. (a) A 3-D schematic diagram and side view of the pulse synthesizer [97]. 1: Polarizing cube, 2: half-wave plate, 3-4: cylindrical telescope, 5: positive acylindrical lens, 6: fold mirror, 7: concave cylindrical mirror, 8: liquid crystal windows, 9: delay mirrors. (b) Schematics of the laser system with pulse shape synthesizer (top right). The amplifying pathway demonstrates a synthesized pre-pulse train and a main pump pulse being amplified in the CPA laser. PBS denotes polarizing beam splitter. (c) Pump beam focusing and target configuration of the SXRL.

The compressed synthesized pulses from the compressor has a beam diameter of 40 mm and are focused by a f = 500 mm spherical mirror and are made to impinge at a 29° grazing incidence

angle onto a polished Mo target, as shown in Figure 3.1 (c), forming a 4 mm long and 32 μm FWHM wide line focus. This pumping geometry provides quasi-traveling wave excitation and utilizes the beam refraction in the plasma to enhance the pump energy deposition efficiency into the plasma region with optimum density for amplification [69, 94]. The target is motorized to expose a new surface to each consecutive laser shot. The SXR emission of the plasma column along the line focus axial direction is spectrally resolved by a 1200 lines/mm variable spacing gold-coated diffraction grating placed at 3 degrees gracing incidence angle and is detected by a back-thinned CCD. Selected thin film Zr and Al filters are positioned in front of the grating to block visible/ultraviolet emission from the plasma from reaching the detector.

The temporal profile of the synthetized SXRL laser pump pulses was measured by an intensity autocorrelator with a potassium dideuterium phosphate (KDP) doubling crystal. Also generated by the pulse synthesizer, a separate low-energy pulse with ~1% energy and a +1 ns delay from the main pump was used as a reference pulse. Intensity profile was measured by cross-correlating the reference pulse with the synthesized pulse profile. The latter was tuned down to 1% of its energy to get the best possible resolution for the pump pulse. The maximum nanosecond contrast is measured to be 2×10^{4}.

The arbitrary pulse synthesizer offers a vast parameter space to be tested, as the delay and intensity of each pulse in the pulse chain can be programmed individually. In this work we focused our effort on generating pre-pulses with various shapes and report the corresponding SXRL output pulse energy. As an example, Figure 3.2 shows the temporal profile of one of the synthesized pump pulses used in the experiment. In this case a train of pre-pulses is set at 900 ps prior to the main pump pulse forming a pre-pulse envelop containing 5% of the total pump pulse energy. A long pedestal with a relative intensity of $\sim1\times10^{-3}$ is also added between the pre-pulse and the main pump pulse to keep the plasma heated while during its expansion, which is crucial in achieving a high gain by ensuring a large density of Ni-like ions is present at the time of maximum gain [24]. This pedestal has programmable intensity achieved by tuning the timing of a cut-off Pockels cell respect

to the arrival of the regenerative amplifier pulse. A pair of secondary pre-pulses were set at 35 ps and 70 ps prior to the main pump pulse arrival with a combined energy of 15% of the main pump pulse energy.

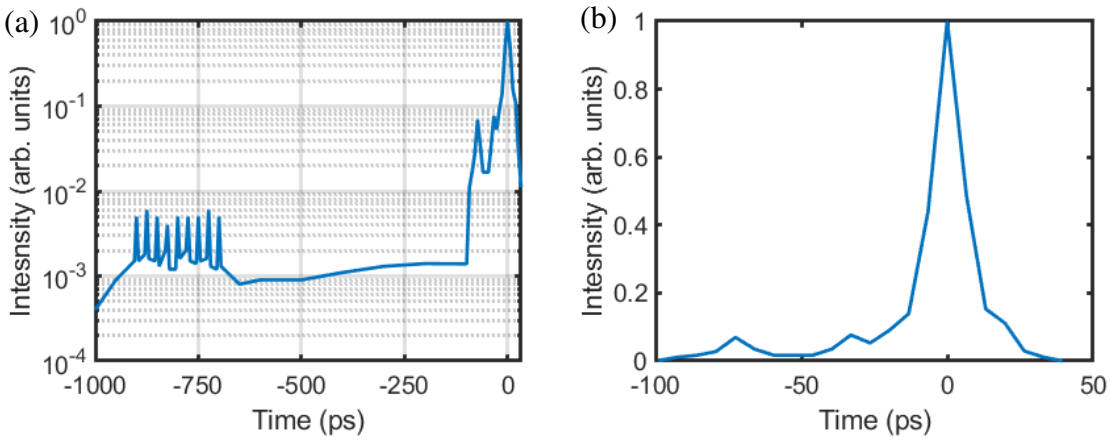

Figure 3.2. Example of synthesized pump pulse shape with a total 730 mJ compressed output pulse energy. (a) The overall temporal profile of a pump pulse consisting of a train of 8 pre-pulses of the same intensity at 25 ps intervals, positioned 900 ps prior to the main pump pulse. The early pre-pulse train contains a combined 5% of the total pump energy in a 1×10^{-3} pedestal, and is followed by a secondary picosecond pre-pulse sequence consisting of 2 closely spaced pre-pulses at -35 ps and -70 ps from the main pulse, containing a combined 15% of the total pump energy. (b) Zoomed-in view near the main pump pulse plotted in linear scale to show the construction of the secondary picosecond pre-pulse pair.

The role of the early pre-pulse was investigated first. Figure 3.3 (a) shows the measured SXRL output corresponding to the different early pre-pulse envelopes illustrated on top of the figure. The total pump pulse energy onto the target was 730 mJ. The plots on top of each bar shows the structure of the first pre-pulse in the synthesized pump pulse plotted in a linear scale. The early pre-pulse consisted of 9 individual pulses at 25 ps intervals. The delay between the first pulse in the pre-pulse sequence to the main pump pulse was set at 900 ps. In all cases the combined energy of the early pre-pulse sequence was kept at 5% of the main pulse energy. The 9 pulses in an up-ramp envelop have relative energy of 1.0, 2.0 ... to 9.0 units. A down-ramp has the same profile in reverse order. The triangular envelop consists of pulses with relative energy of 1.4, 3.4, 5.4, 7.4,

9.4, 7.4, 5.4, 3.4, 1.4 units. The square envelop consists of 9 pulses all with 5.0 units of energy. The individual pulses under the envelop all have a 2.5% accuracy in energy. The histogram plots the mean values of the SXRL output energy and the shot-to shot standard deviations obtain for each early pre-pulse sequence. Fifty measurements were averaged for each synthesized pump pulse. A maximum output pulse energy of 1.24 ± 0.22 μJ was recorded with the "square" envelop. The "up-ramp" envelop offered similar output at 1.20 ± 0.20 μJ, while the "triangular" and "down-ramp" envelop had a relative low SXRL output. This result stablished the use of train of pulses of equal intensity for the rest of the study.

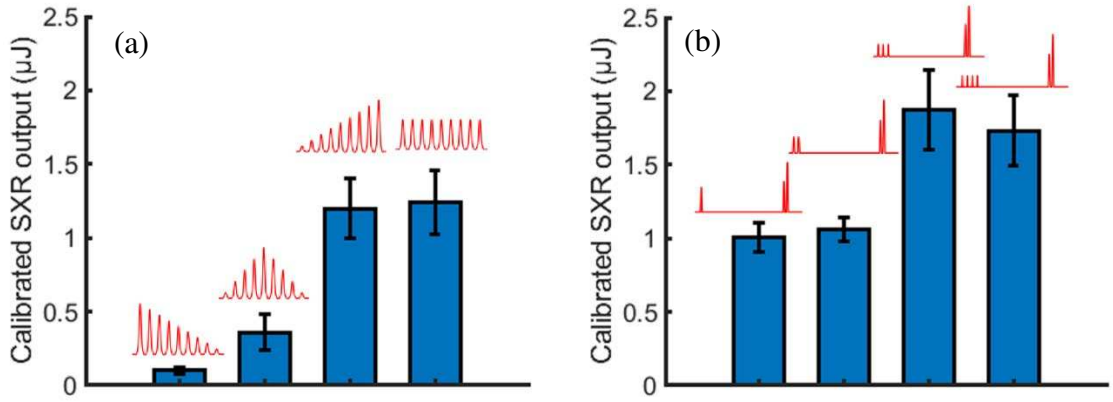

Figure 3.3. (a) Average SXRL laser output and standard deviation with ramp, triangular and square pre-pulse shape. A maximum output of 1.24 ± 0.22 μJ was recorded with the "square" envelop. (b) SXRL laser output with 1 to 4 "discrete" pre-pulses in the early pre-pulse train with 70ps interval between pulses. A maximum output of 1.87 ± 0.27 μJ was recorded for the pre-pulse consisting of 3 "discrete" pulses.

Figure 3.3 (b) shows the SXRL output energy corresponding to various early pre-pulse sequences each composed of a different number of pulses with the same intensity and a separation of 70 ps. Shown in the small plots over each bar, plotted along the main pulse of the complete synthesized pump pulse plotted in logarithm scale. Early pre-pulse trains with 1 to 4 individual pulses separated by 70 ps intervals are shown from left to right. In all cases the combined energy of the early pre-pulse is set to be 5% of the main pump pulse. In all 8 experiments, a single

secondary pre-pulse with 10 % of the energy of the main pulse is set to arrive 5 ps prior to the main pump pulse. The highest output SXRL energy obtained using these "discrete" type of pre-pulses, 1.87 ± 0.27 uJ, corresponds to the test with 3 discrete pre-pulses. The intensity of this SXRL pulse, computed assuming ~5 ps pulse duration and near field spot size of ~30 µm [98] exceeds the gain saturation intensity [69].

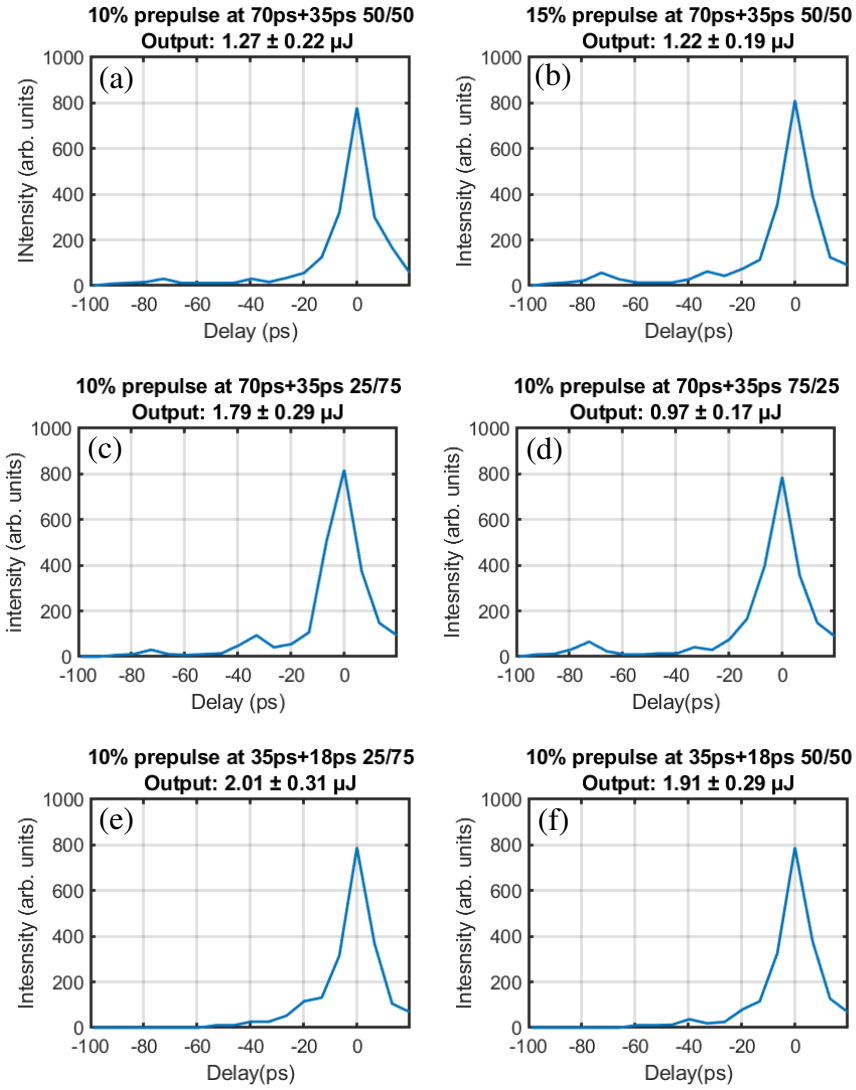

Figure 3.4. Various picosecond pre-pulse structures with same main pump pulse energy, and the corresponding resulting SXL pulse energy: (a) 2 ps pulses at -70 ps and -35 ps, with 10% combined energy and 50/50 energy split, (b) 2 ps pulses set at -70ps and -35 ps, with 15% combined energy and 50/50 energy split, (c) same condition as (a) with 25/75 energy split, (d) same condition as (a) with 75/25 split, (e) 2 ps pulses at -35 ps and -18 ps, 10% combined energy with 25/75 energy split, (f) 2 ps pulses at -35 ps and -18 ps, 10% combined energy and 50/50 energy split. In all of the experiments the early pre-pulse is fixed as the best condition in Figure 3.3.

Examples of the optimization of the SXRL output by tuning the late picosecond pre-pulse sequence with the pulse synthesizer are shown in Figure 3.4. Previous simulation and experiments have shown that a single picosecond pre-pulse set at several tens of picoseconds prior to the main pump pulse can significantly increase the SXRL output [90]. With the pulse synthesizer we were able to explore more complicated structures of the picosecond main pump pulse. By testing a wide range of pulse delays and energy split combinations, we found, as shown in Figure 3.4 (e), that if a picosecond pre-pulse with 10% total energy is set within 35 ps prior to the main pump pulse with an up-ramp yields high output. If the start of the laser picosecond pre-pulse sequence is set earlier than 50 ps prior to the main pump pulse, or if its intensity is too weak, the output of the SXRL is rapidly reduced. The highest SXRL output pulse energy was achieved with a pair of picosecond pre-pulses set at 15 ps and 18 ps prior to pump pulse, with a 25%/75% energy split and with a total combined energy of 10% respect to the main pump pulse.

Starting with the combination of the previous best early pre-pulse structure with a train of 3 early pre-pulses followed by a secondary picosecond pre-pulse set at -35 ps and -18 ps, further optimization was conducted. In order to search for the best SXRL output, three parameters were scanned: the delay of the early pre-pulse respect to the main pump pulse, the energy fraction of the early pre-pulse train, and the energy of the picosecond pre-pulses respect to the main pump pulse. Measurements of the synthesized waveform were taken after each parameter was changed, to ensure the energy ratio of all individual pulses is not altered. The results are summarized in Figure 3.5. The highest output pulse energy achieved with 730 mJ of total pump pulse energy was 2.4 ± 0.3 μJ. The SXR conversion efficiency is more than 50% increased respect to our previous work, in which we reported 1.5 uJ output for the 18.9 nm the Ni-like Mo SXRL pumped by with same total pump pulse [24]. As described in section 1.3, the best condition for the X-ray lasing requires a good overlap of the regions with high concentration of Ni-like Mo ions, high electron temperature, and relatively low density gradient. The first pre-pulse generates the plasma and give it adequate time to cool and expand to decrease the density gradients while the secondary pre-pulses heats the

plasma in the region with a high abundance of NI-like ions. It has shown by the experimental data that a small change in the synthesized pulse can lead to large variations to the output of the SXRL. This is because the gain depends exponentially from the population inversion and therefore is highly dependent on the plasma parameters. A feedback loop between simulation and experiments with the synthesized pulses can lead to farther optimization of the SXRL.

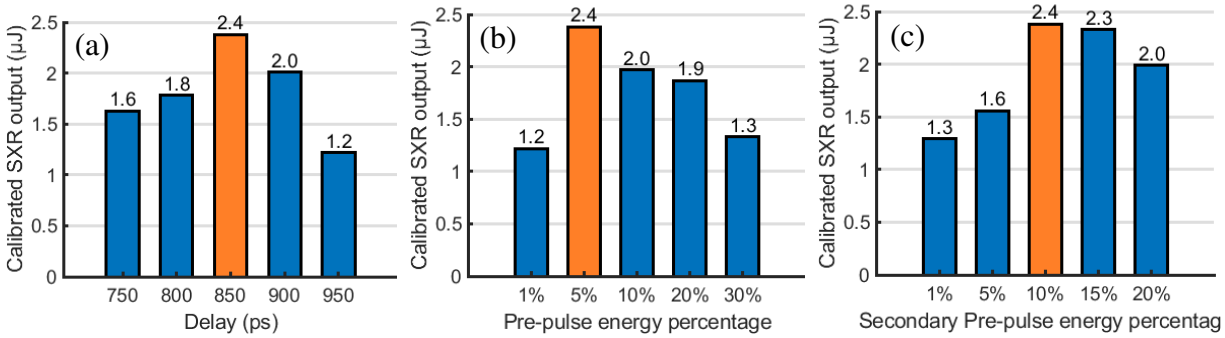

Figure 3.5. SXRL output pulse energy dependence on: (a) pre-pulse delay respect to the main pump pulse. (b) Energy of the early pre-pulse train with other parameters set to the best result in (a). (c) Energy of picosecond pre-pulse group with other parameters set to the best in (b). The synthesized pump pulse is composed of and early pre-pulse sequence of 3 discrete pulses early pre-pulses and the optimized pre-pulse structure of Figure 3.4 (e).

3.3 Conclusion

This section of the dissertation demonstrates an 18.9 nm tabletop SXRL driven by a CPA laser with the capability to synthesize pump pulses of arbitrary temporal profile. The wide range of synthesized pre-pulse temporal structures investigated shows the plasma amplifier is very sensitive to both the early pre-pulse structure and that of the main picosecond pump pulse. When optimized, the synthesized pump pulse increased the SXRL output pulse energy by ~ 50% respect to the best previously used pump pulse sequences when using the same total pump pulse energy. A best of 2.4 ± 0.3 uJ SXRL output was recorded for a 730 mJ of pump energy on target. The pump pulse sequences explored are only a very small fraction of the possible pump pulse parameter space. The combination of simulation and experiment with synthesized pulses, along with genetic algorithms

and machine learning techniques can be expected to significantly further increase the output pulse energy and the efficiency of plasma-based SXRLs.

Chapter 4 Pulse compression of high energy picosecond Yb:YAG laser pulses to femtosecond range with a gas-filled hollow core fiber

4.1 Introduction

Yb:YAG is one of the best choice as a gain medium for high-energy, high average power, solid state laser systems [41]. In recent years cryogenic Yb:YAG CPA laser systems have been demonstrated and have shown the capability to generate Joule-level output energy at kilo-watt average output power [28] [42] [20] [22]. Yet, at cryogenic temperatures the gain bandwidth of Yb:YAG is usually sub-nanometer which limits the pulse duration of compressed to pico-second level, limiting their use in applications requiring femtosecond pulse duration, such as laser wakefield particle accelerators [38]. In chapter 1 we have discussed the characteristics of Yb:YAG as laser gain medium. At room temperature conditions Yb:YAG has enough bandwidth to support ~1 ps pulses. However, the high saturation fluence and thermal properties of room temperature YAG are disadvantages to obtain high output pulse energy from Yb:YAG amplifiers. While cryogenically cooled Yb:YAG amplifiers significantly lessen these limitations and have generated pulse energies exceeding 1 J at 1 kHz repetition rate [18], their output bandwidth is limited to ~ 0.35 nm that corresponds to transform limited pulsewidth of 3.1 ps level ($sech^2$) [22, 25].

Several methods of spectral broadening utilizing non-linear effects in different medium have been investigated in different type of lasers, including self-phase modulation in fibers, multi-pass cells [99-102], laser plasma filaments [103] and external cavities [104]. Among all the spectral broadening techniques, optical fiber holds a few potential advantages over others such as overall system simplicity and a consistent output mode. Post compression was first demonstrated with glass core single-mode optical fibers, in an experiment in which 50 fs pulses were compressed to 6 fs [105]. However, the energy of the pulses was limited to the nJ level due to unstable high order

non-linear effects and material damage in the fiber core. M. Nisoli et al. first demonstrated pulse compression utilizing high pressure noble gases in a hollow core fiber (HCF) as the dispersive element [106]. Spectral broadening was purely achieved by self-phase modulation (SPM) in the gas media, enabling higher energy (mJ level) to be used.

With more advanced optical coupling and pumping technique for non-linear gas media, higher intensity, higher energy and higher average power have been achieved by HCF broadening and post compression. For results of milli-Joules level or above with Ti:Sapphire laser systems, S. Sartania et al. demonstrated post compression by compressing 0.5 mJ, 20 fs Ti:Sapphire pulses down to 5 fs, at 1-kHz repetition rate. Ouillé et al. has demonstrated 10 mJ, 24 fs pulses compressed to 5 mJ, 3.5 fs with a 2.5 m long HCF charged with helium [107]. Hort et al. has demonstrated 75 mJ, 55 fs pulses compressed to 10 mJ, 10 fs with short HCF/capillary charged with helium working in heavy ionization regime [108]. Various improvements to the HCF technique have also been reported. For example, M. Giguère [109] and A. Suda et al. [110] have shown that increased stability in mode and transmission can be achieved by having a pressure gradient in the HCF. Hoffmann et al. demonstrated spectral broadening by the mixing effect of SPM and stimulated Raman scattering (SRS) for ~ 1 mJ pulses in an SF_6 charged HCF [111], showing the possibility to further broaden spectrum in a HCF using the Raman non-linearity.

HCF post compression results on Yb-based laser systems with milli-Joule and higher pulse energies have also been reported. Viotti et al. demonstrated compression of 0.8 mJ. Nagy et al. have demonstrated compression of 5.8 mJ, 300 fs pulses to 10 fs level with a 6 m, 400 μm core HCF charged with argon [112]. Pulses of 200 fs duration and up to 70 mJ from a Yb:CaF_2 amplifier have been shown to be compressible to 40 mJ, 25 fs with a 2.8 m, 1 mm core hollow core fiber charged with neon, as demonstrated by Fan et al. [113], although the repetition rate was not reported. However, bandwidth broadening with HCF of pulses with pico-second pulse duration, where the output of cryogenic Yb:YAG amplifiers sits, is more challenging. Since SPM is intensity driven, a long temporal pulse width of ~5 ps level requires higher (hundred to several hundreds

mJ) pulse energies to initiate sufficient SPM. This can make coupling into the fiber, along with controlling the non-linear processes, more challenging. In this chapter, we demonstrate 3.7 nm broadening of 300 mJ pulses by SPM, reaching a post compression ratio > 16:1.

4.2 Simulation of HCF transmission with non-linear effects.

4.2.1 Non-linearly processes in HCF

Two of the most major non-linear processes in optical fibers are self-phase modulation (SPM) and stimulated Raman Scattering (SRS). The physics for both processes in single mode glass fiber were well studied back in the 1970s [114, 115]. In the experiment described in this dissertation, the HCF is charged with a gas medium which has a much lower non-linearity than solid materials, but that can also be driven with a much high energy pulse. The physics describing the pulse transmitting through the much longer HCF and the de-focusing caused by possible plasma generated in the HCF can significantly complicate the mathematics. However, much of the same fundamental physics can be applied to these very different scenarios.

Chapter 1 discussed the $\chi^{(3)}$ non-linearity in general, and the mathematical model of the SPM/SRS processes. This section of the dissertation will first describe a few details of the physics of SPM and SRS processes in HCF, along with Stokes walk-off from transient group-velocity dispersion (GVD) processes aiding to spectral broadening of the short pulse. This section also describes the numerical simulation of pulse transmission in HCFs.

If we take as a zeroth order assumption making the laser pulse with wave vector k transmitting through a section of HCF as a perfect cylinder with length L, and considering that the wave packet has intensity profile $I(t)$, the phase φ_{nl} accumulated by SPM can be written as:

$$\varphi_{nl} = kLn_2I(t) \tag{4. 1}$$

The Fourier transformation from the time domain into the frequency domain writes:

$$P(f) = \int_{-\infty}^{\infty} I(t) e^{-2\pi i t f}\, dt \tag{4. 2}$$

in which f is the frequency, as t is measured in seconds, f is measured in Hertz. $P(f)$ is the Fourier transformed function in frequency space.

A phase shift $\varphi(t)$in Fourier transformation writes:

$$P(f) = \int_{-\infty}^{\infty} I(t) e^{-2\pi i t f + i\varphi(t)}\, dt \tag{4. 3}$$

With the phase shift described in (4. 1),

$$P(f) = \int_{-\infty}^{\infty} I(t) \exp(-2\pi i t f) \exp(kLn_2 I(t))\, dt \tag{4. 4}$$

which is illustrated in Figure 4.1 for an assumed Gaussian intensity profile with red and green lines indicating the case of $kLn_2 = 3\pi$ and $kLn_2 = 5\pi$.

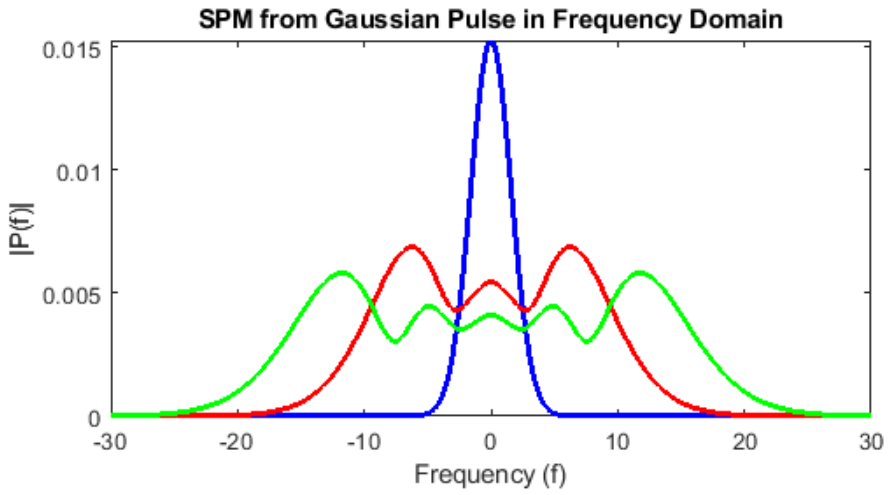

Figure 4.1. Fourier transformation of 0π, 3π and 5π phase modulation plotted in frequency domain. A frequency lobe is generated on each side of the initial pulse.

Since in the simulation both the step size or L in (4.1) per iteration, and the size of the individual wave packets in the rays are small, the simulation discussed in this section treats SPM linearly and

only calculates the phase modulation and wave vector change from the local intensity for each ray. The wave vector of each ray in the beam is calculated for every iteration by computing the local $n_0 + n_2$ and its nearest two neighbors for a 5-point average, a new k-vector is generated, and the phase shift over time is accumulated and stored in an array variable belonging to the particular ray.

Another major contributor of the spectrum broadening effect is stimulated Raman scattering (SRS). Below we discuss the case of nitrogen, which is the non-linear medium that produced the best results in the HCF experiments discussed in this dissertation. The experimental results are discussed in section 4.3. Various $\chi^{(3)}$ non-linear effects in nitrogen gas have been both measured experimentally and modeled. G. Tartar et al. offered a model of cascade growth of free electrons leading towards optical breakdown in nitrogen with 1 μm photons, for pulse widths up to nanoseconds [116], C. Peters et al. offered detailed results in modeling various N_2 transitions pumped by femtosecond multiphoton processes [117]. For the SRS process, N_2 has only one fundamental vibrational-rotational band. The first Stokes on the $S(6)$, $S(8)$, $S(10)$ rotational lines are at 59, 75, and 91 cm^{-1} with intensity ratio of 4:6:1 [118-120], but it is also reported that the $S(6)$ line will significantly weaken with higher intensities. Therefore in the simulation we use a single 75 cm^{-1} line for simplicity. When pumped with 1030 nm from a Yb:YAG laser, this leads to a first Raman scattering peak at 1038 nm. Further Raman scattering peaks require a much higher intensity of the pump laser and will not be discussed in this chapter.

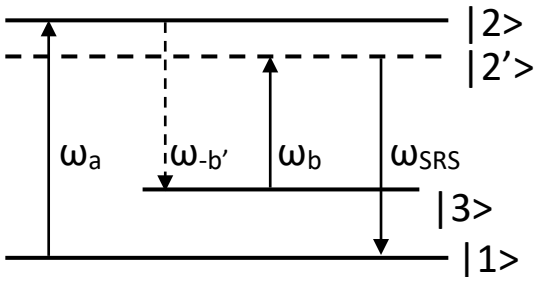

Figure 4.2. Quantum picture of SRS. A total of 3 photons generate the 4th photon via a $\chi^{(3)}$ process. In the condition of utilizing N_2 as non-linear medium, ω_a, ω_b indicate the photons with pump and Stoke-shifted frequencies, as discussed in Chapter 1, and ω_{SRS} is the generated photon with frequency shift from SRS.

Figure 4.2 illustrates a typical frequency shift schematic of (Stokes) SRS. When a photon is absorbed to drive a transition from level |1> to |2> in the material, after some relaxation time, the quantum state |2> drops back to a different lower state |3> releasing a photon with a different frequency. The |2> state could have a slight energy variation and drift to the |2'> state, and another absorption/emission pair completes the $\chi^{(3)}$ process, generating ω_{SRS}. The lower intensity of the newly generated Stokes pulse at the leading edge of the pulse sees lower effective index of refraction, leading towards a group velocity dispersion (GVD) process causing a walk-off effect [121]. The combined effect of SRS and GVD depletes the leading edge of the pulse and makes a steeper slope, adding more chirp to the leading edge through SPM. Note that the stimulated Raman scattering occurring in the HCF is non-resonant, which means we do not discuss the effective $\chi^{(3)}$ from the cascaded $\chi^{(2)}$ non-linear process. The onset effect of SRS would be an unsymmetrical spectral broadening [122]. Such broadening effect was observed in N_2 gas by Eimerl et al. [123] and further investigated and modeled by G.S. McDonald [124], who in his work discussed the behavior of the delay generated in the medium by SRS in the transient regime, which is also applicable in this work.

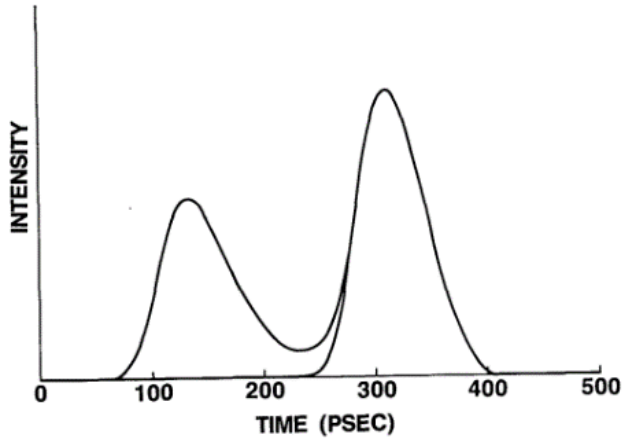

Figure 4.3. high-speed photodiode temporal measurement of a 1064nm pump (right peak) and its Stokes-shift 1120 nm pulse from a single mode fiber with 145 m length. The Stokes shifted pulse pulls a total of 205 ps lead over the pump pulse. Please note the GVD in this example (from[121]) is significantly stronger than in the experiments described in this dissertation.

From equation:

$$\Delta n(\omega_a) = n_2(\omega_a)I_a + 2n_2(\omega_a, \omega_b)I_b \quad (1.\ 24)$$

We can see that while Raman conversion efficiency rises from zero, the initial Stokes-shifted Raman peak would see a lower effective index of refraction and start to pull a temporal lead from the pump pulse, as shown in Figure 4.3.

And as illustrated in Figure 4.4 [125], the Stokes-shifted pulse would start to be created at the leading edge of the pulse, and due to its lower intensity, and thus lower n_2 contribution and higher group velocity, it will gradually pull an increasing lead over the pump pulses and will start to see less Raman gain. During the process of this lead creation, the Raman conversion from the leading edge of the pump is higher than that from the trailing edge, effectively reshaping the pump pulse and making the leading edge sharper.

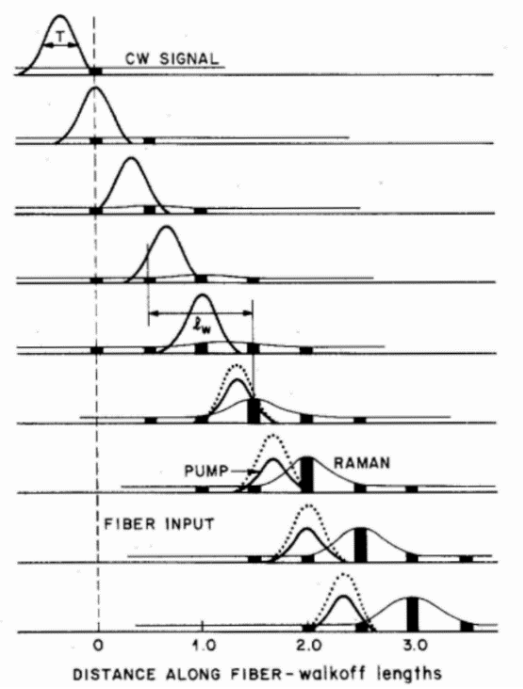

Figure 4.4. schematic of Stokes-shifted pulse leading the pump while amplified via SRS through the GVD process [125].

Combining this phenomenon and SPM, we can see that when the SRS/GVD process co-exists with SPM, the sharpened leading edge will get more dispersion as the Stokes-shifted pulse pulling the lead [121, 122, 124], creating a asymmetric broadening profile. Figure 4.5 shows how the SRS/GVD gradually being added by increasing pump power and its contribution to the broadening of the spectral profile.

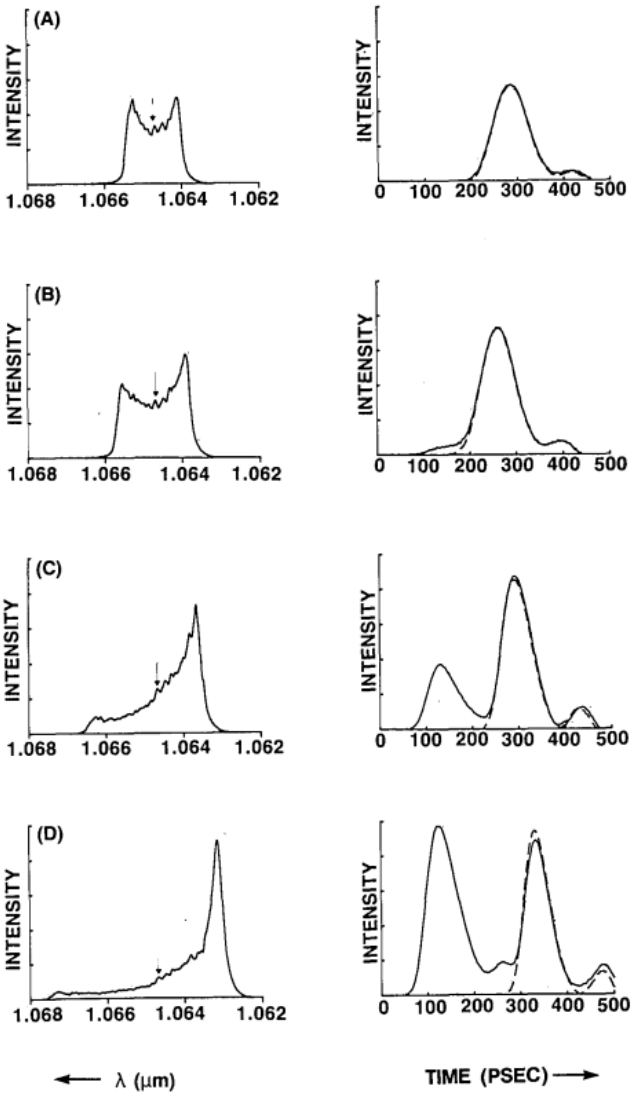

Figure 4.5. Asymmetric broadening from SRS/GVD process in a single mode fiber. From (A) to (D) shows cases with Raman conversion ratio being 0%, 11%, 35%, and 60%. The output spectrum is plotted on the left. The right plots corresponding temporal intensity profile of the resulting beam (solid line) versus pump beam with Stokes filtered out (dashed line) [121].

However, during the HCF experiments described in section 4.3. As described below, we added only a minimum amount of SRS/GVD to further broaden the spectrum. The use of differential pumping limits SRS generation to only the HCF section close to the output of the fiber. It was found that too much SRS added to the system causes an instable chirp and makes compression difficult. Efforts are made to prevent such conditions.

4.2.2 Simulation of laser pulse transmitting through HCF with non-linear processes

The solution to the Maxwell equation of the travelling wave in a cylindrical waveguide takes the form of Bessel series. To simulate the laser pulse transmitting in the fiber, we first choose the ideal Bessel beam series:

$$E(r,\phi,z) = \sum_{n=0}^{\infty} A * \exp(ik_z z) J_n(k_r r) * \exp(\pm in\phi) \tag{4. 5}$$

In which k_z and k_r are wave vector along direction (z) of the fiber and radial direction (r).

With a flat-top laser beam profile, the beam pattern at the focal plane would be an Airy-disk, which is also the lowest order Bessel beam J_0. Writing equation (4. 5) into its integral form, and replacing $r^2 = x^2 + y^2$:

$$E(r,\phi,z) = \frac{A}{2\pi}\exp(ik_z z)\int_0^{2\pi} \exp[ik_r(x\cos\phi + y\sin\phi)]\, d\phi \tag{4. 6}$$

If we further define:

$$\theta = \arctan\left(\frac{k_r}{k_z}\right) \tag{4. 7}$$

This breaks the initial condition of the Bessel beam into an infinite series of plane waves angled θ away from the axial direction of fiber. By measuring the actual coupling angle used in the experiments, we choose $\theta = 0.005$ as the equivalent numerical aperture for the coupling. This

greatly simplifies the calculation of the pulse wave packet, since under the assumption of a straight fiber, it's possible to ray-trace just a plane wave travelling through the fiber, and integrate over angle to get the intensity profile. This method is also much less computationally expensive than solving the conversion coefficients between the Bessel modes in the fiber per iteration.

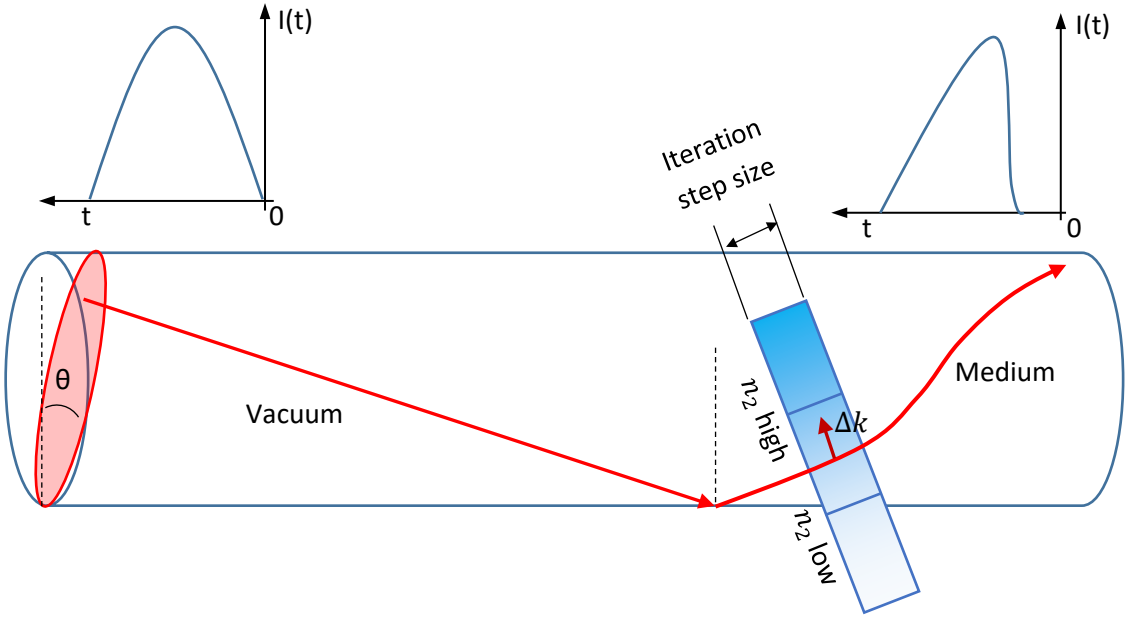

Figure 4.6. Illustration of the ray tracing process in the HCF. The sizes, profiles and angles are exaggerated to show the details. The cylinder in the illustration represents the HCF inner wall. The red disk represents the plane wave derived from (4. 6) (4. 7). Individual rays are generated from a grid on the plane wave with initial k-vector, as illustrated by the red arrow. Each ray carries an intensity profile I(t), as shown on top of the illustrated HCF. Reflection and non-linear-processes calculated per iteration, change of k-vector and I(t) are made accordingly.

This initial condition is illustrated in Figure 4.6. The plane wave described by (4. 6) (4. 7) with $\theta = 0.005$, $\phi = 0$ is plotted at entrance side of the HCF. A grid with pixel size of 1.0 μm is applied to the wavefront of the plane wave and breaks the plane wave down to individual rays. Each ray on the grid is given an initial k-vector perpendicular to the wave front and 8 ps Gaussian intensity profile I(t) based on the measured pulse temporal profile. With each ray carrying 1 nJ of energy, the total energy of the input pulse is 79 mJ.

A simplified picture of the ray tracing algorism is also illustrated in Figure 4.6. For plotting clarity, the illustration only shows one ray and one reflection. For this individual ray, the part prior to the reflection describes transmission in vacuum, where the non-linearity is zero, and the k-vector remains unchanged until a reflection is detected. When occurring, the reflection is simulated by mirroring the k-vector over the normal to the HCF wall. The part post reflection describes transmission in the non-linear medium, where the local intensity profile generates a gradient of index of refraction, and hence a change of k-vector, Δk, is generated per iteration, and added to the ray. Also per iteration, SPM phase accumulation and Stoke shifting are also calculated from the local n_2. This phase data and the modification to the intensity profile are saved into the data carried along the ray, as illustrated by the output I(t) profile plotted near the output of the HCF in Figure 4.6.

The intensity profile is generated by first integrating the plane wave over ϕ from 0 to 2π, as in equation (4. 6). To reduce the calculation load, the integration is implemented by summing over 100 steps with a 3.6 degree step size. A 3-D grid size of 50 μm is chosen and rays within the cube of each grid pixel are counted and the intensity in the grid is calculated by summing over the I(t) profiles of every ray inside the cubical pixel. This intensity profile is then used to calculate all the non-linear processes. Figure 4.7 compares the intensity profile from the ray tracing model at $z = 400\ mm$ in vacuum, which is near the first node in the HCF, to that obtained by directly calculating the Bessel coefficients up to J_4 term, plotted in red. The answer from the ray tracing model is within ±2.1% of the Bessel solver, while only requires ~10% of calculation time of the Bessel solver**.** For a 5 m fiber with many reflections, this computational advantage become significant. The advantage of the faster calculation by the ray tracing model makes it possible to do additional calculations per iteration, other than just accumulating the phase delay from SPM, such as keeping track of the k-vector and intensity profile per ray as mentioned in Figure 4.6, which are necessary to simulate the SRS process.

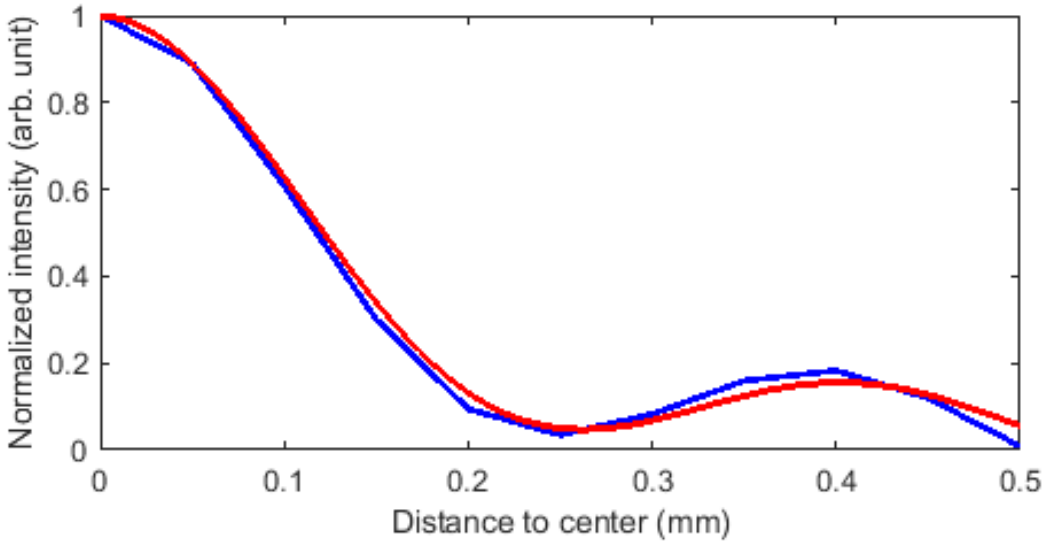

Figure 4.7. 1-D intensity profiles at $z = 400\ mm$ into the HCF obtained by the ray tracing model (blue) and by solving the Bessel coefficients from the reflection up to the J_4 term (red). The Bessel solver cutoff is set low to prevent inconsistency caused by dividing small numbers. The ray tracing model is within ±2.1% of the solution of the Bessel solver.

The 1 mm hollow core diameter fiber used in the experiments can carry a significant number of higher order modes [30], especially when n_2 is high enough for the SRS/GVD processes to step in. Figure 4.8 shows the 2-D intensity profile generated by ray-tracing at z = 5000 mm, which corresponds to the exit of HCF used in the experiment described in next section, for different N_2 pressures. In all 4 cases, the input energy is 300 mJ with 530 μm spot size at $1/e^2$ taking a form of airy disk, and the core size is 1 mm. In Figure 4.8 (a), the HCF is in vacuum; while in (b), (c), (d) the HCF entrance pressure is 120 Torr, and the exit HCF pressure is 300 Torr, 400 Torr, 600 Torr, respectively. A linear pressure profile is assumed in the HCF. Reshaping the output mode of the HCF by the combined influence of all non-linear processes is clearly seen from the result, especially when both the intensity and the pressure are high enough for the SRS process to become relevant. The comparison of Figure 4.8 and Figure 4.9 shows SRS strongly de-focuses the beam inside HCF and couples more energy into the higher order modes of the HCF. This is a double-edge sword, as discussed in Chapter 1 and also demonstrated later in this Chapter: while SRS

broadens the spectrum further and offers a shorter pulse when compressed, the introduction of too much SRS introduced also deteriorates the output beam profile and the stability of transmission.

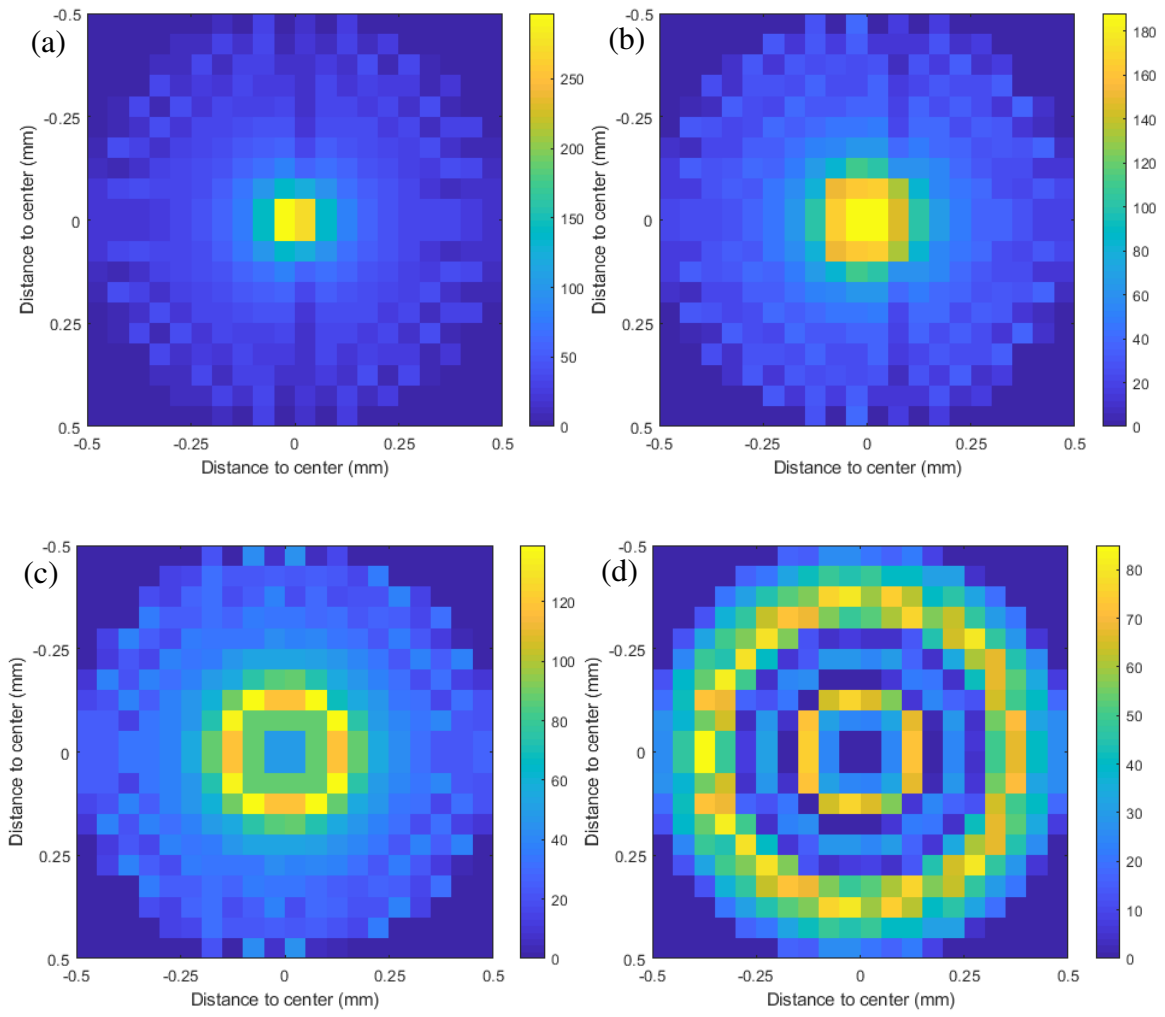

Figure 4.8. Ray-tracing example of the output of a 1 mm diameter, 5000 mm long HCF with 300 mJ input energy. The initial plane wave is set with $\theta = 0.005$, $\phi = 0$, The grid size for intensity profile is 0.050 mm, i.e., each pixel in the figure represents a 50 μm × 50 μm area at the exit of HCF. (a) is the vacuum condition for reference, where no SPM or SRS is present; while in (b), (c), (d), the input of HCF is set at 120 Torr N_2, while the pressure linearly increase to 300, 400, and 600 Torr, respectively. In the case of 400 Torr N_2 the de-focusing from SRS is visible, and causes the beam to diverge more quickly in the 600 Torr case, where the majority of the energy is coupled into higher order modes.

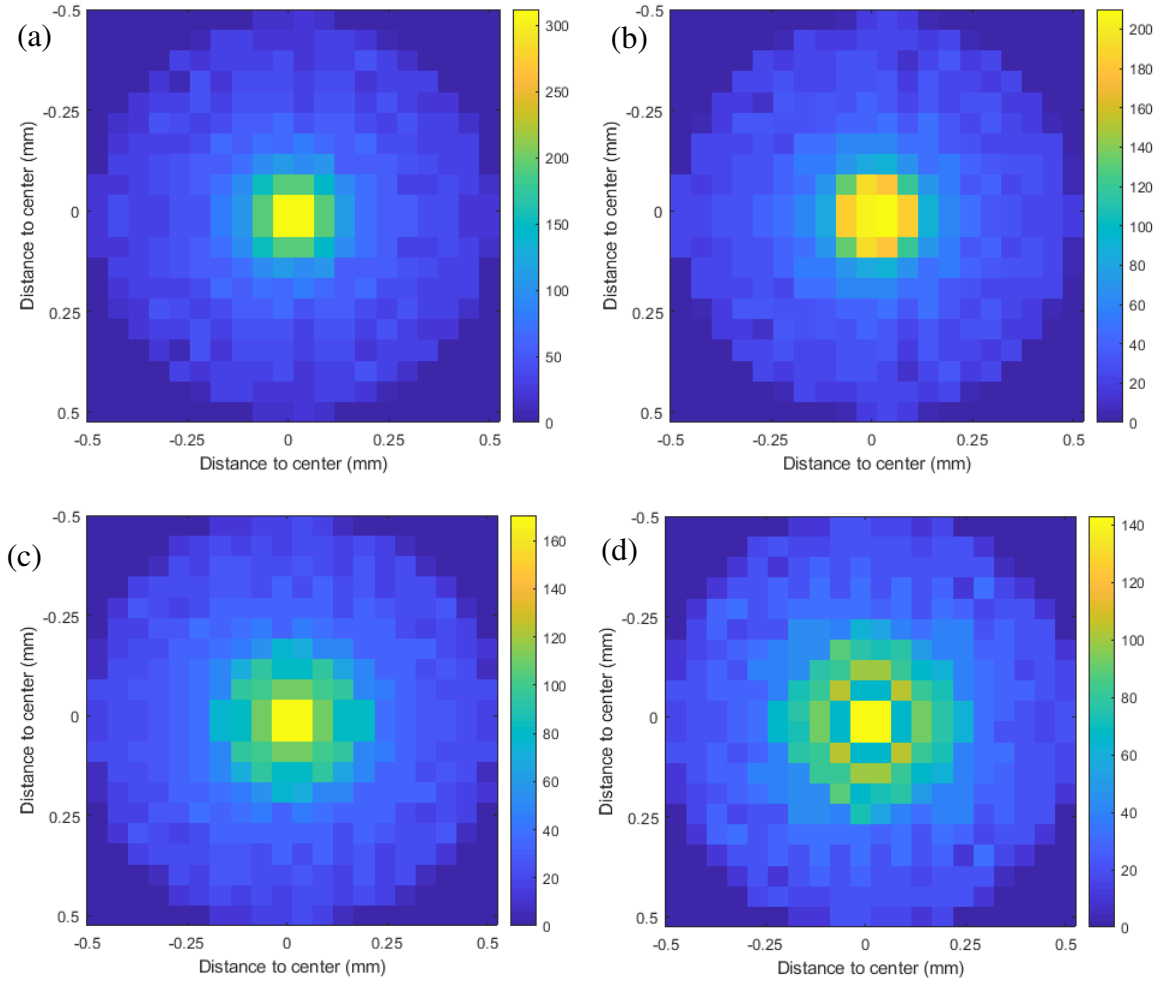

Figure 4.9. Ray tracing results for the same laser pulse energy and pressure conditions as in Figure 4.8, with coefficients of SRS terms set to zero to show only the contribution of Kerr lensing effect modifying the HCF output mode. In all cases, the ratio of energy coupled into the higher order modes is lower, and the order of most populated of Bessel modes are also lower. Note that this result is a demonstration of a case where the contribution of SRS is deliberately taken away, and does not represent the actual behavior of the nitrogen gas filled HCF.

Also, since the parameter space that can be tested is large, although a detailed model of spatially SPM was fairly easy to implement, modelling Raman scattering effects in the HCF from the dipole interactions has proved unnecessarily sophisticated. To get an order-of-magnitude result for aiding the experiments, a simplified approach utilizing the Kramers-Kronig relations was implemented.

From the Keldysh model and also from experimental measurements, nitrogen, along with other diatomic molecules, has a transition from a fast electronic nonlinearity when pumped with < 100 fs pulses; to a slow, orientational nonlinearity when pumped with ~1 ps or longer pulses [126]. With our laser pulse set at ~7.5 ps in the simulations, a nitrogen non-linear index of refraction $n_2 = 7.9 \times 10^{-20}\ cm^2/W$ is used [126, 127]. From transmission measurement with high pressure nitrogen (>300 Torr) and taking the assumption of the initial transmission loss is solely due to SRS, from integrating (1.13) we estimate a maximum Stoke shift gain of 2.0 ± 1.0 cm/TW. Since the laser bandwidth is small (~4 nm), both n_2 and the Stoke shift gain are assumed to be a constant across the bandwidth in the simulation.

Within each iteration, a grid of 25×25×25 μm is set within the pulse volume, for each sub-volume Δn is obtained, and for each ray, a new k-vector is calculated and the added SPM amount is stored. Phase delay from the propagation itself is not considered since the fiber is long (5 m) and large in diameter (1 mm) relative to the laser wavelength, many 2π delays will be added with even one reflection inside the fiber core, The simulation assumes a well-mixed phase at the output of the fiber.

SRS is modeled in a similar fashion, by expanding the electric field E in series of plane waves:

$$E(z,t) = \frac{1}{2}\sum_n P_n(z,t)\exp[i(\omega_n t - k_n z)] \tag{4. 8}$$

We use the same plane wave from the Bessel expansion, and from equations (1.13) and (1.22):

$$\frac{dI_a}{dz} = -\alpha_0 I_a - \alpha_2(\omega_a,\omega_a)I_a^2 - 2\alpha_2(\omega_a,\omega_b)I_a I_b \tag{4. 9}$$

We numerically solve this equation to match the fiber transmission measurement with observable SRS asymmetrical broadening under the assumption that during the transient onset of SRS, SRS is the only contributing term of absorption of the pump beam. Then from Kramers-

Kronig relation and assuming small bandwidth, the change of index of refraction can be described as the integration of all shifted frequencies ϖ:

$$n_2(\omega_a, \omega_b) = \frac{c}{\pi}\int_0^{\infty} \frac{\alpha_2(\varpi, \omega_b)}{\varpi^2 - \omega_a^2} d\varpi \tag{4. 10}$$

By summing over the rays with both pump frequency and Stoke-shifted frequency within each sub-volume, SRS/GVD can be obtained locally and stored in individual rays. At the exit, the combined accumulated phase shift is Fourier transformed and is shown in Figure 4.10. At lower pressures SPM is the governing mechanism. As pressure increases, SRS gradually becomes the dominating factor, and as discussed in Chapter 1, creates more broadening in the leading/red side of the beam, as shown by the increasing asymmetry from Figure 4.10 (b) to (d).

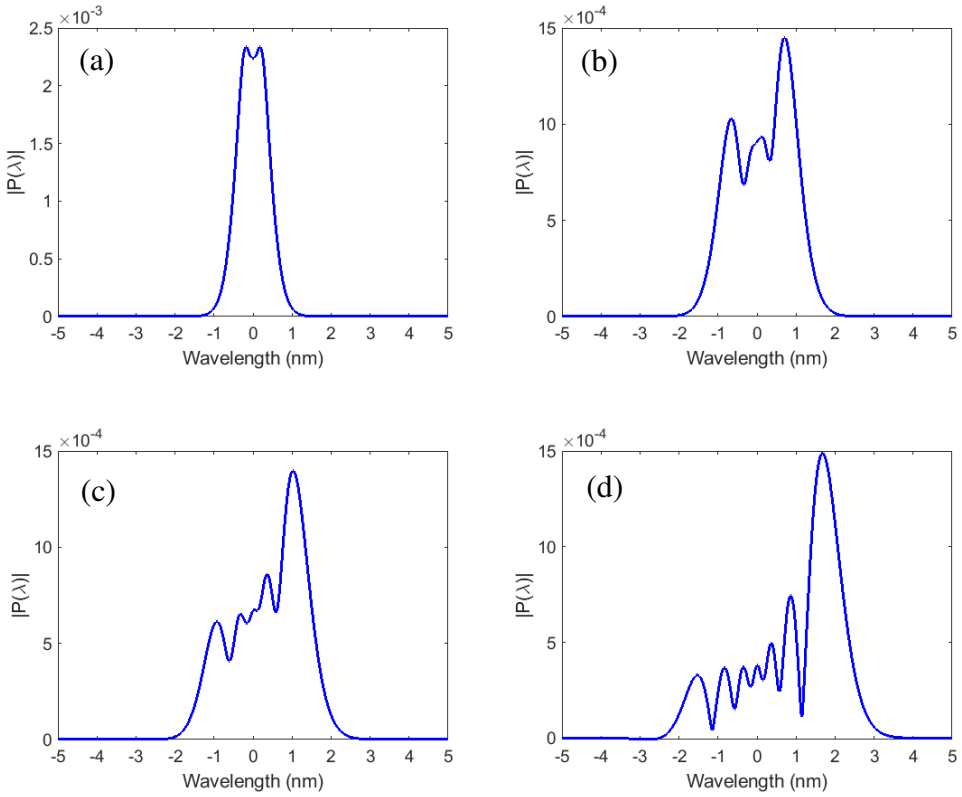

Figure 4.10. Simulated HCF output spectrum for 300 mJ input pulses and different exit pressures. From (a) to (d), exit pressure: of 100, 200, 300, 400 Torr N_2. Bandwidths of 1.7, 2.4, 3.1, 4.5 nm are generated, corresponding to transform limited pulse widths of 920, 650, 504, 340 fs. The fraction of pump energy that is Stoke-shifted is: <0.5%, 2%, 7%, 24%, respectively.

Simulations were conducted with different pressure parameters. As shown in Figure 4.11, an SRS limit of 650 mJ with 600 Torr nitrogen is expected, as beyond this condition no more energy is transmitted in the fundamental J_0 Bessel mode. However, this limit is higher than the highest energy coupled in the fiber tip before ablation occurs so it is not relevant to the experiment.

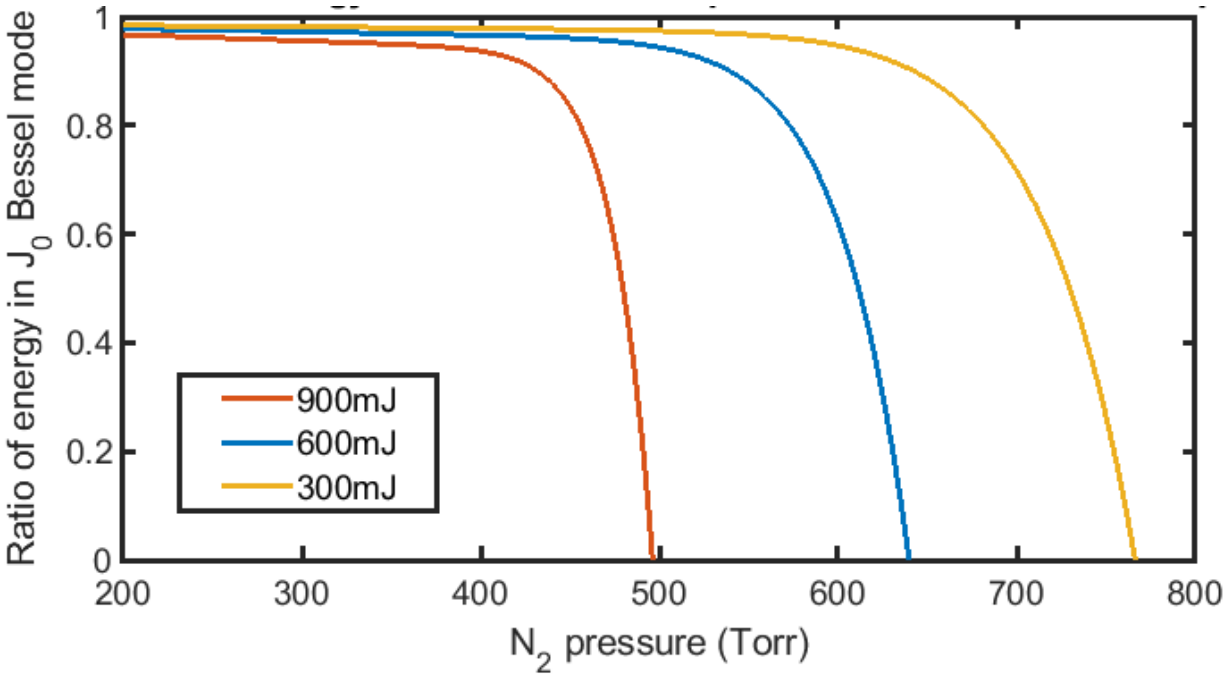

Figure 4.11. Simulated amount of energy in the fundamental (J_0 Bessel) mode reconstructed at the exit of the HCF. SRS de-focusing becomes extreme for nitrogen pressures greater than the SRS threshold at the exit of the HCF, as shown by the fast decline.

The simulation of the amount of energy that is Stoke shifted and contributes to the SRS/GVD process is plotted in Figure 4.12. At the working condition of the broadening experiment described in next section, pulse energy between 200-300 mJ and pressure of 300 Torr of N_2, 5-15% of the energy is computed to be Stoke shifted, but since the 75 cm^{-1} line is too far to be connected to the broadened spectrum, this portion of energy is not compressible.

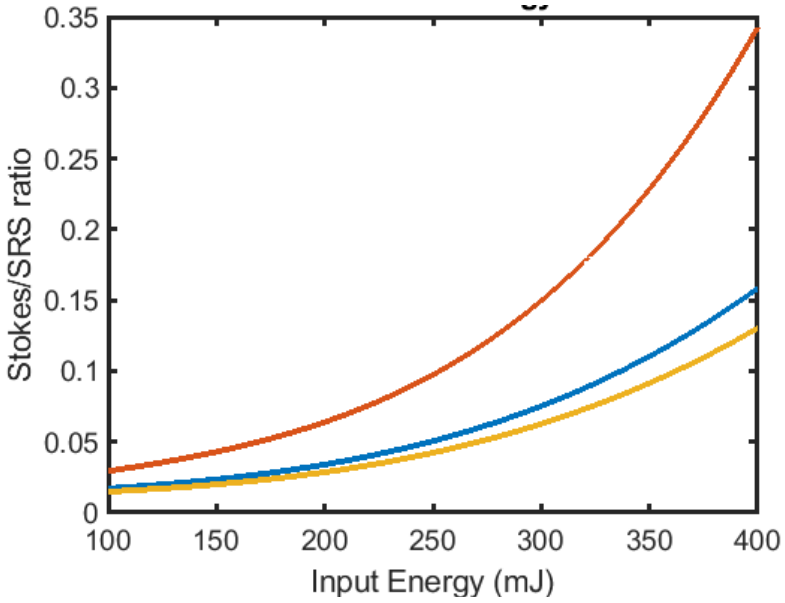

Figure 4.12. Computed energy fraction that is Stokes shifted and contributes to the SRS/GVD process for the case with 300 Torr N_2 at the exit of HCF with differential pumping. The colored lines show the cases of: highest (red), 5-point average (blue), and lowest local $n_2(\omega_a, \omega_b)$ (orange) among the nearest neighbors of each simulation grid point being-chosen for simulating the SRS process.

There are both technical and computational limitations to the simulation. Since the simulation is based on ray tracing, it does not provide an analytic result of mode propagation, and only a rough estimate to the SRS/GVD process due to the change of k-vector is based on a finite grid size. Also, it does not account for ionization and plasma generation in the media. The latter can be observed experimentally with a much tighter focus at the entrance of the HCF (~150 μm), but was not observed with a >500 μm spot size used in the experiment. These simulated results (Figs (4.8-4.12)) offer guidelines for the experiment in choosing the non-linear media and working conditions such as energy and pressure range, as well as diagnosing mode output of HCF. The next section will discuss the experimental results of post compression.

4.3 Experiment of HCF broadening and post-compression

The layout of the HCF pulse broadening and compression experimental set up is shown in Figure 4.13. The HCF is used has a hollow core diameter of 1 mm and a length of 5 m. The entrance of the fiber consists of a conically shaped high grade alumina piece designed to minimize ablation by the laser. Both ends of HCF are initially evacuated with a turbomolecular pump to a pressure of $< 2 \times 10^{-5}$ Torr. A mass flow controller is used to inject gas into the system**.** A constant N_2 gas pressure in the range of 0-600 Torr can be maintained at the exit of the HCF while the entrance is always pumped to better than 3×10^{-2} Torr. When the pressure at the fiber exit is set at 300 Torr of nitrogen, the pressure at the front tip is both simulated and measured experimentally to be 120 Torr. The simulated pressure pattern across the HCF as shown in Figure 4.13 (b). The dimensionless critical pressure ratio $\frac{p_d}{p_u}$ between the downstream pressure and upstream pressure equation is given by [128]:

$$\frac{p_d}{p_u} = \left(\frac{2}{\gamma + 1}\right)^{\frac{\gamma}{\gamma - 1}} \tag{4. 11}$$

in which γ is the heat capacity ratio of the gas and for nitrogen at 25°C, $\gamma = 1.40$. Assuming ideal gas behavior and $\gamma = 1.40$, steady-state choked flow takes place when $\frac{p_d}{p_u} < 0.528$. This implies the HCF is in choked flow condition, from the simulated pressure pattern shown in Figure 4.13 (b), the choke occurs at ~800-1000 mm from the high pressure side. The choke creates a high pressure gradient at the end of HCF and the majority of the length post choking point stays at a consistent low pressure. Since both SPM and SRS are positively correlated to pressure, this hinders SPM to utilize the whole length of HCF, also forces the SRS to occur within a short length, causing instability as shown later in the chapter.

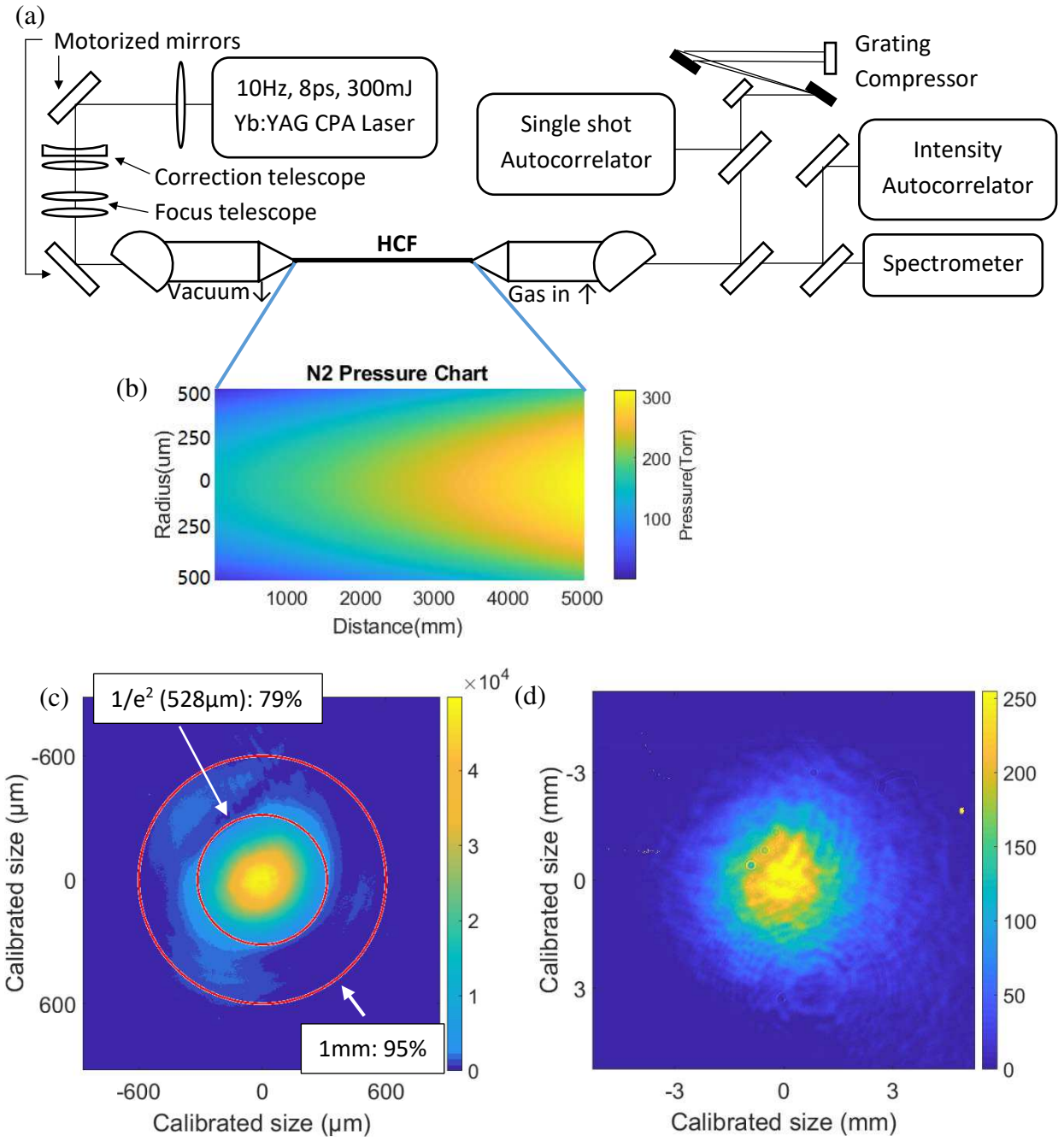

Figure 4.13. (a) Schematic of the HCF pulse compression set up; (b) Simulated N_2 pressure profile in the 1 mm diameter, 5000 mm long HCF with 300 Torr on the beam exit side; (c) laser beam profile at the input of the HCF. The Yb:YAG amplifier has a flat-top beam profile that focuses into an Airy-disk pattern. The focal spot has a $1/e^2$ spot size of 528 μm with 90% of the total energy contained within the first Airy ring. The rings in the input beam pattern shows the integrated energy within the circle diameter; (d) output beam profile at 2 m from the exit tip of the HCF. Almost all energy is in its fundamental mode.

The cryogenically cooled chirped-pulse-amplification Yb:YAG laser used in these experiments was operated at 10 Hz repetition rate to produce pulses that have a bandwidth of 0.28 nm, corresponding to a transform limited pulse of 5.6 ps. For this experiment, a 15% positive chirp is added to the pulse to prevent too much energy being drained into stimulated Raman scattering (SRS) processes as discussed in Chapter 1. The input pulse duration of HCF is set at 8.0 ps, measured by a scanning intensity autocorrelator with resolution of 50 fs and range up to 300 ps. The beam profile at the output of the amplifier chain has a flattop profile that is focused with a single f = 10 m lens forming an Airy pattern in the focal plane at the entrance of the fiber. A pair of cylindrical lenses of f = 500 mm is added to correct astigmatism and a 1:1 telescope with f = 1.5 m lenses is set to fine-tune the position of the focus respect to the HCF input. Cameras are installed at both the input and output of HCF to monitor the beam profile. The images from these cameras also drive an auto-align system with two motorized mirrors placed in the focusing chain to compensate for pointing drift of the laser beam during operation. A vacuum compressor with a 1200/mm grating compresses the output of the HCF. The spectrum at the output of HCF is monitored by a fiber-coupled grating spectrometer with 0.11 nm resolution. A single shot autocorrelator measures the post-compressed pulses. The single shot autocorrelator has a sample beam diameter of 6 mm and has a crossover angle of $2\phi = 24°$, offering 5.5 fs resolution and 2 ps range. All the diagnostics are synchronized with the laser in order to characterize individual pulses.

The optimal mode size for maximum transmission in the 1 mm hollow fiber tested to be 600 μm. However a spot of such size has an Airy disk type profile in which 12% of the pulse energy falls outside the fiber core. Under this condition 300 mJ laser pulses are observed to cause ablation at the entrance of HCF. This degrades transmission and leads to poor stability with large shot to shot energy fluctuations at the exit of the fiber. A slightly smaller diameter of 528 μm is chosen as a balance between good transmission, stability, and good output mode. The laser beam pattern at the entrance of HCF is shown in Figure 4.13 (c). It has a $1/e^2$ spot size of 528 μm and has with 90% of the total energy contained within the first airy ring versus the theoretical 91%.

79% of the energy is measured to fall within the area defined by e^{-2} of the peak intensity, compared to 81% for an ideal flat top beam. In this case 95% of the energy falls within the fiber core area. Ablation of the fiber entrance still takes place under this condition, but as discussed below its detrimental effect can be mitigated with gas flow. The corresponding output beam profile at 2 m from the fiber exit is also shown in Figure 4.13 (b). Almost all energy in its fundamental mode. Figure 4.14 compares the simulated and measured intensity distribution at a distance of 2 m from the exit of the fiber. The spot size, divergence and shape of simulated and measured spot are all in good agreement.

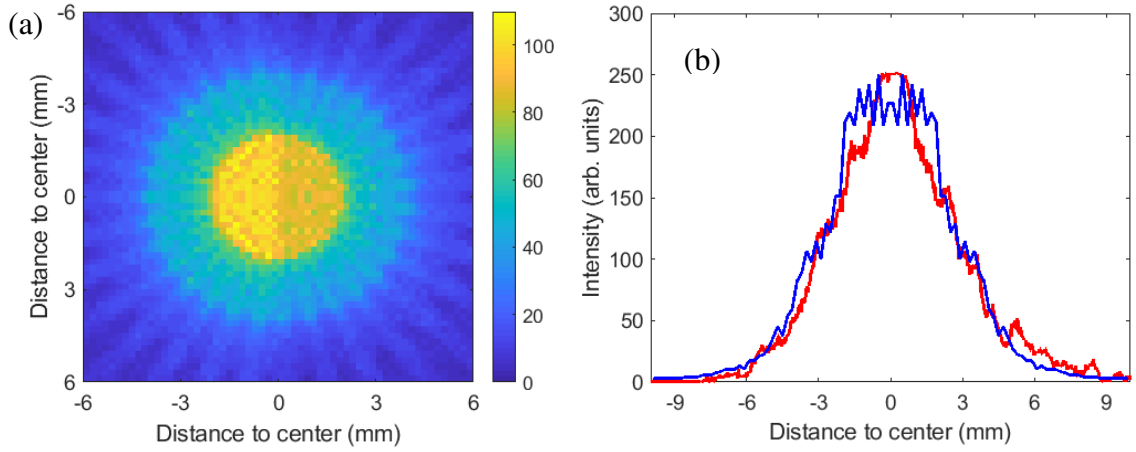

Figure 4.14. (a) Simulated pulse profile at 2 m away from the HCF output with 300 mJ input, 300 Torr of N_2 at the exit of the HCF with differential pumping, derived from Figure 4.8 (b). (b) Comparison of ~~a~~ vertical cuts of the simulated and measured spot at 2 m from the fiber exit.

Nitrogen was chosen as the non-linear medium for a balance between n_2, flow, and the ability to offer some stimulated Raman Scattering (SRS) at the intensity of our experiment to further broaden the spectrum. Figure 4.15 shows the measured laser pulse transmission through the HCF as a function of N_2 pressure and input pulse energy. In vacuum 300 mJ pulses can be transmitted with 78% efficiency. The transmission of these pulses remains the same as the pressure increased to 150 Torr but decreases to 72% when the pressure reaches 300 Torr, and further decreases at higher pressure as an increased amount of the energy is Stokes shifted. As shown in Figure 4.12,

for 300 mJ pulses and 300 Torr N_2, between 5%-15% of the pulse energy is Stoke shifted and contributes to adding dispersion by the GVD process [121]. Ionization is found not to be the major limitation. The ADK[129] model predicts initial ionization occurs at 3.3×10^{14} W/cm^2 with 600 Torr of N_2 [130] which corresponds to ~ 4 J input pulse energy at our focus condition. At this intensity with 8 ps pulse duration, a cascade avalanche ionization leading to plasma generation in HCF is expected, This value is much higher than the fiber tip ablation threshold observed, therefore it is outside the scope of this experiment.

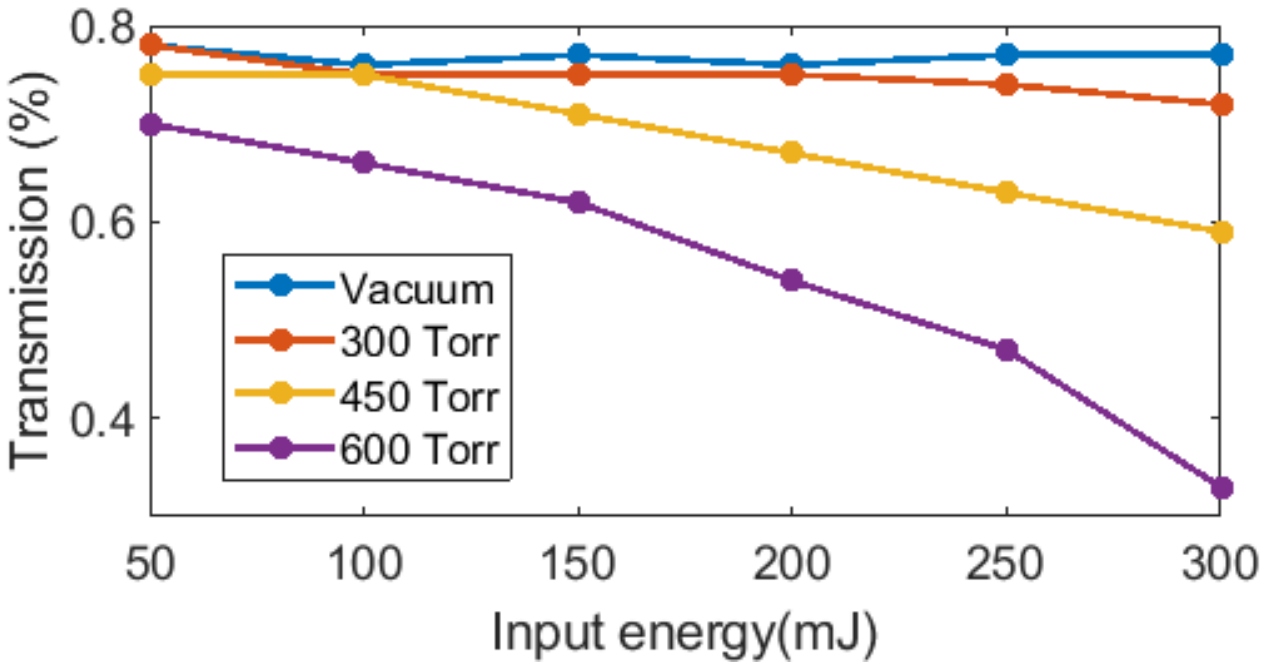

Figure 4.15. Measured HCF transmission efficiency of 300 mJ pulses as a function of N_2 pressure at the fiber while the entrance of HCF is constantly pumped to ~ 2×10^{-2} Torr vacuum. The pressure inside HCF immediately before the tip is ~120 Torr due to the fact that the HCF is heavily choke flowed. The difference of transmission between 150 Torr N_2 and in vacuum is less than 1%, therefore only the vacuum case is plotted as a reference.

For the pulse compression tests the input end of the fiber vacuum was constantly pumped with a 300 l/min scroll pump and N_2 was injected into the exit end of the fiber to stablish a gas flow to help clear material that might be occasionally ablated from the fiber tip. Figure 4.13 (b) shows the computed gas density distribution along the fiber when the pressure at the fiber exit is 300 Torr.

At pressures below 250 Torr the transmission stays relative constant and only SPM broadening is observed when pulses of up to ~300 mJ energy are injected into the HCF. At higher pressures the Raman effect becomes relevant. It de-focuses the beam and drives energy into higher order modes of the HCF as discussed in chapter 1, while also some energy is Stokes-shifted. Additional broadening from SRS is observed while the transmission drops slightly and the output mode of the fiber deteriorates. When driven harder (than 300 mJ), occasionally, plasma is generated from avalanche ionization near the exit of HCF and the emission spectrum of N_2 with plasma de-focusing can be observed in the output. Such conditions are avoided for the experiment, since at this condition the transmission of HCF is both low and inconsistent. For an input energy of 300 mJ a N_2 pressure of 300 Torr was found to offer the largest amount of broadening with a minimal transmission loss. Stability of the HCF transmission in such condition is illustrated in Figure 4.16.

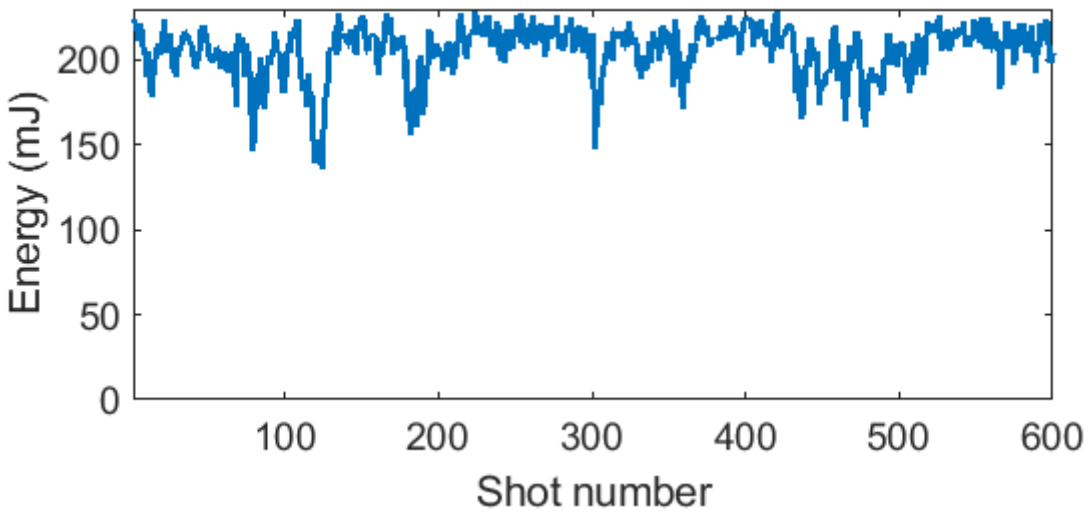

Figure 4.16. Stability of transmission of HCF with 300 Torr at exit of HCF with differential pumping and 300 mJ at input of HCF. During the test the laser runs at 10 Hz.

The output spectra of HCF under the condition of charged with 100, 200, and 300 Torr of N_2 with differential pumping mentioned above, with input laser pulse energy from 100 mJ to

300 mJ, are shown in Figure 4.17. In each pressure condition a spectrum measured when HCF is in vacuum is also shown as reference.

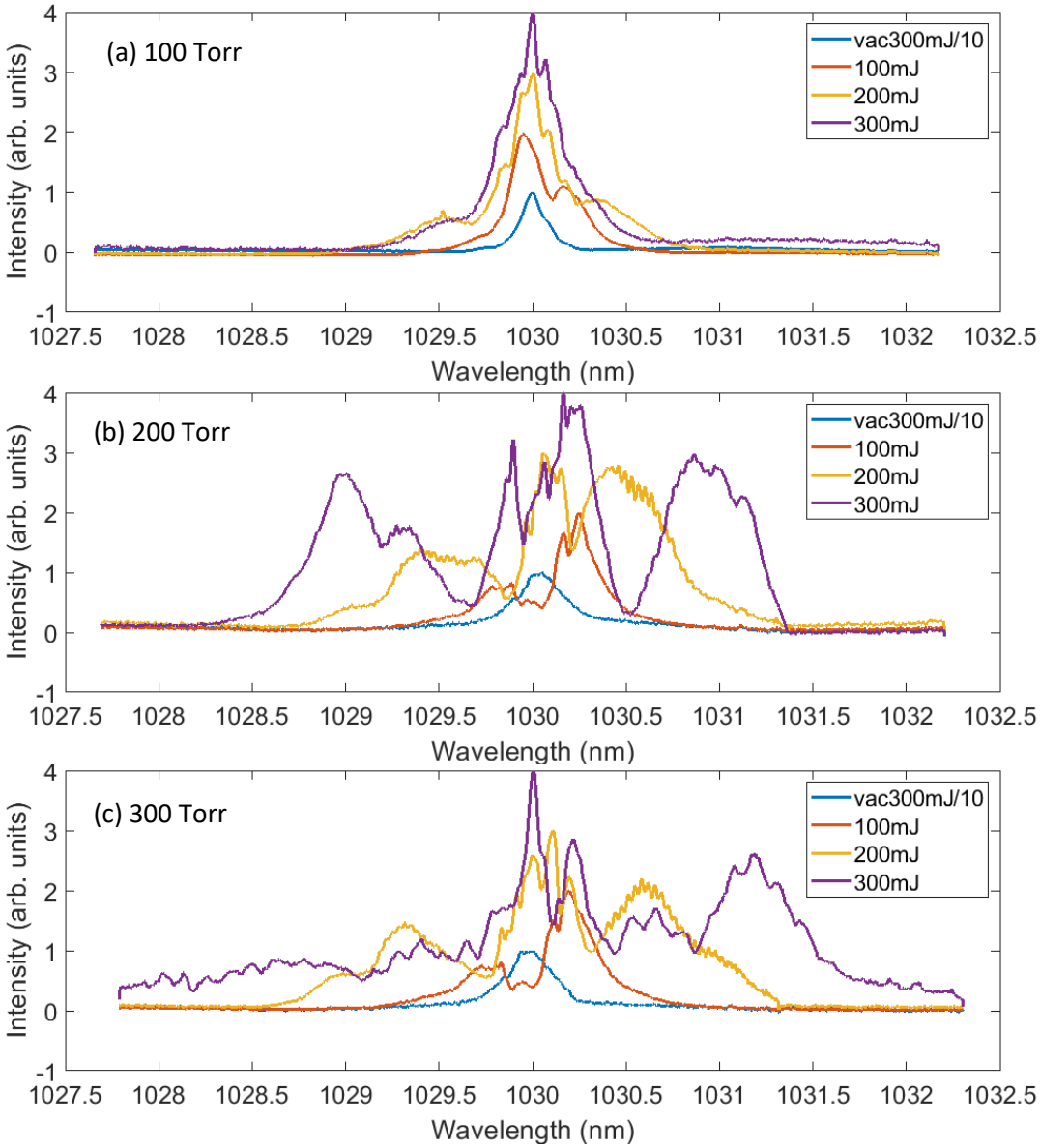

Figure 4.17. Spectra of the HCF output for pressures of: (a) 100 Torr; (b) 200 Torr, and (c) 300 Torr of N_2. The blue, red, orange, purple lines plots the spectrum of input energy of: vacuum with 300 mJ, 100 mJ, 200 mJ, 300 mJ. Pure SPM can be observed in almost all cases, apart from the 300 Torr, 300 mJ case, where the asymmetrical broadening of SRS/SRS effect is apparent.

The most broadened spectrum with pressure/energy combination for which SPM is still the dominating non-linearly is shown in Figure 4.18. With 300 mJ input energy and 250 Torr N_2

charged to the exit side of HCF, a spectrum with FWHM = 2.71 nm is achieved, offering a transform limit of 575 fs. The output of the HCF was compressed by a grating compressor with a pair of 1200/mm line density gold coated diffraction grating. The pulses were re-imaged to a size of 6 mm and after attenuation by reflection on a set of wedges were then characterized by a single shot autocorrelator with a resolution of 5 fs. The compressed profile of this spectrum is shown in Figure 4.19. An average of 590±6 fs was measured by the single shot autocorrelator.

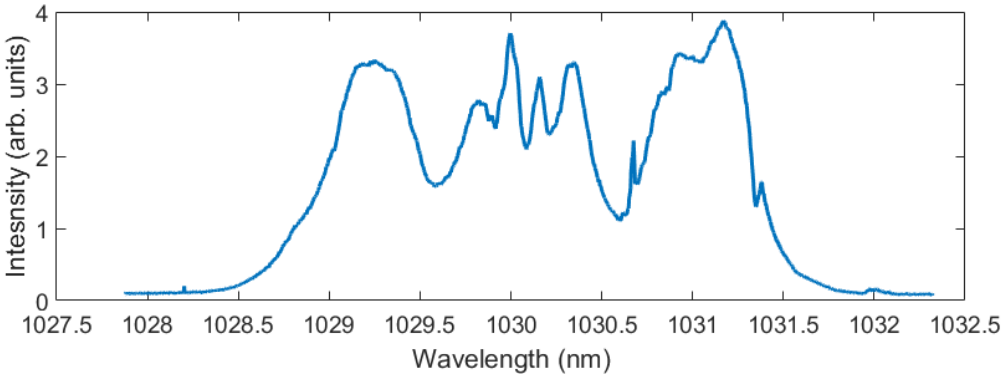

Figure 4.18. Most broadened spectrum obtained before the SRS effect becomes apparent. The pulse input energy is 300 mJ and the HCF exit pressure is set at 250 Torr. A spectrum with FWHM = 2.7 nm is achieved with only SPM, as shown by its symmetrical shape. Both the measured bandwidth and compression are consistent in this condition.

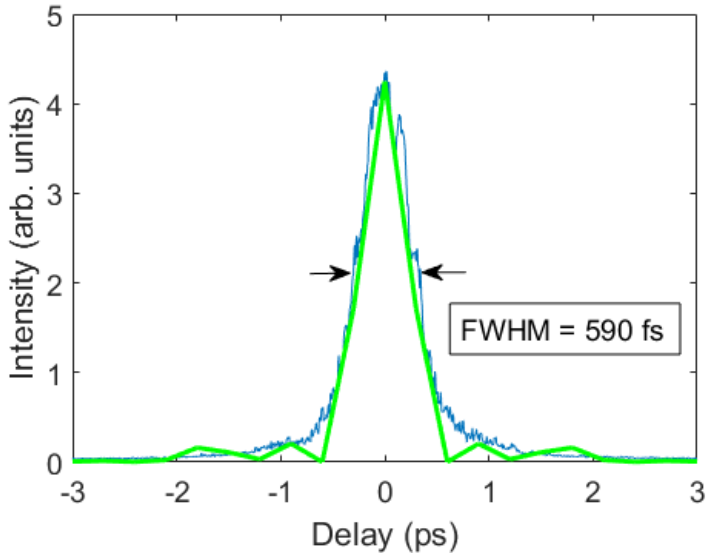

Figure 4.19. Single shot autocorrelation of compressed pulse corresponding to the spectrum in Figure 4.18. The compressed pulse has a FWHM pulse duration of 590±6 fs. The green line indicates the Fourier transform of the corresponding spectrum offering a FWHM of 575 fs.

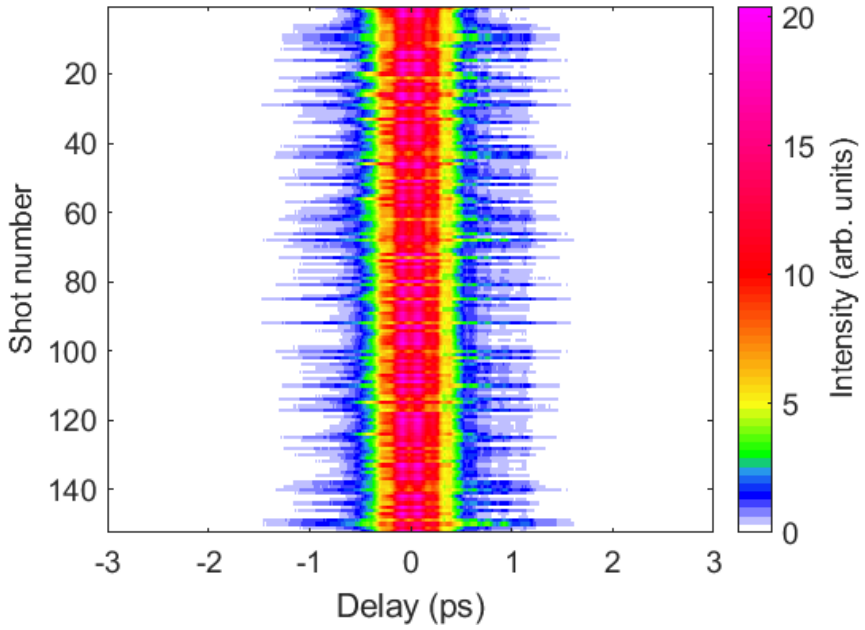

Figure 4.20. Sequence of single-shot autocorrelator measurements showing 152 consecutive shots of compressed HCF output in the condition described in Figure 4.18 and Figure 4.19. Each horizontal line represent a measurement same as Figure 4.19 with the color map showing the intensity. Red in color map marks half of the peak intensity, so the two edges of red marks the FWHM of the pulse duration. Each color change towards the low side on the color bar (or contrast change in black and white) marks half of the intensity of the previous color. The average and standard deviation of the sequence is 590±6 fs, the median is 587 fs, and the two extremes are 577 fs and 610 fs.

As the N_2 pressure and the energy increase up to the combination of 200 mJ and 300 Torr, or 300 mJ and 250 Torr, SPM is the dominating $\chi^{(3)}$ non-linearity. Up to ~ 9π phase delay is accumulated, which offers SPM lobes with ~2.7 nm broadening with minimum transmission loss. Figure 4.20 plots 152 consecutive shots being compressed from the output of HCF with 300 mJ input, 250 Torr exit pressure of N_2 and 74% transmission. The plot is normalized to the maximum intensity of all the pulses. As shown in Figures 4. 16 to 4. 18, in the condition of most broadening is achieved by pure SPM, both the broadening and compression are consistent. As the input energy rises to 300 mJ with 300 Torr N_2, enough energy is Stokes shifted and SRS/GVD processes are significant enough that would help further broaden the spectrum but also cause the spectrum to lean towards the leading edge, which is the red/long wavelength side, as described in Chapter 1.

The simulated energy ratio in the Stokes shifted energy for SRS broadening effect to be significant is ~5%. This is also consistent with the ~3% energy loss observed experimentally, as shown in Figure 4.11 and the 300 Torr case in Figure 4.15. When energy or pressure of N_2 is increased further, the output mode and SRS broadened spectrum become unstable and are difficult to compress.

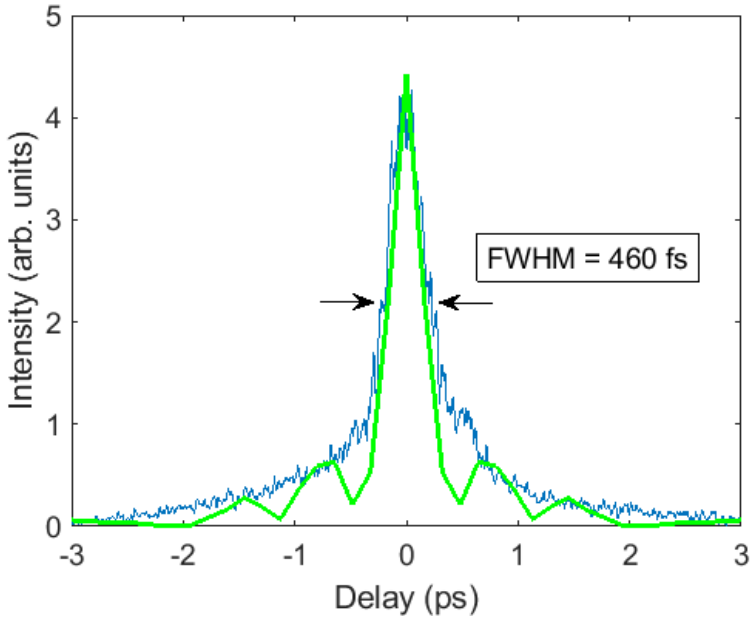

Figure 4.21. Single shot autocorrelation of compressed 300 mJ pulse corresponding to the spectrum in Figure 4.17 (c). The output of HCF is compressed by a grating compressor with 1200/mm line density. The pulse FWHM is measured to be 460 ± 17 fs. The green line shows the Fourier transform of the corresponding spectrum which has a FWHM of 420 fs.

Figure 4.21 shows the temporal profile of the compressed HCF output for the 300 mJ input pulse energy condition in Figure 4.17 (c). The measured compressed FWHM pulsewidth is 460 fs. For comparison the green line in this figure shows the Fourier transform of the corresponding spectrum. The transform limited pulse width of the given spectrum is 420 fs. There is a good agreement on the majority of the temporal profile, yet some high-order dispersion that is not well compensated by the grating compressor is still present in the pulse. This is the result of GVD adding arbitrary high order dispersion to the leading edge of the pulse, as discussed in Chapter 1.

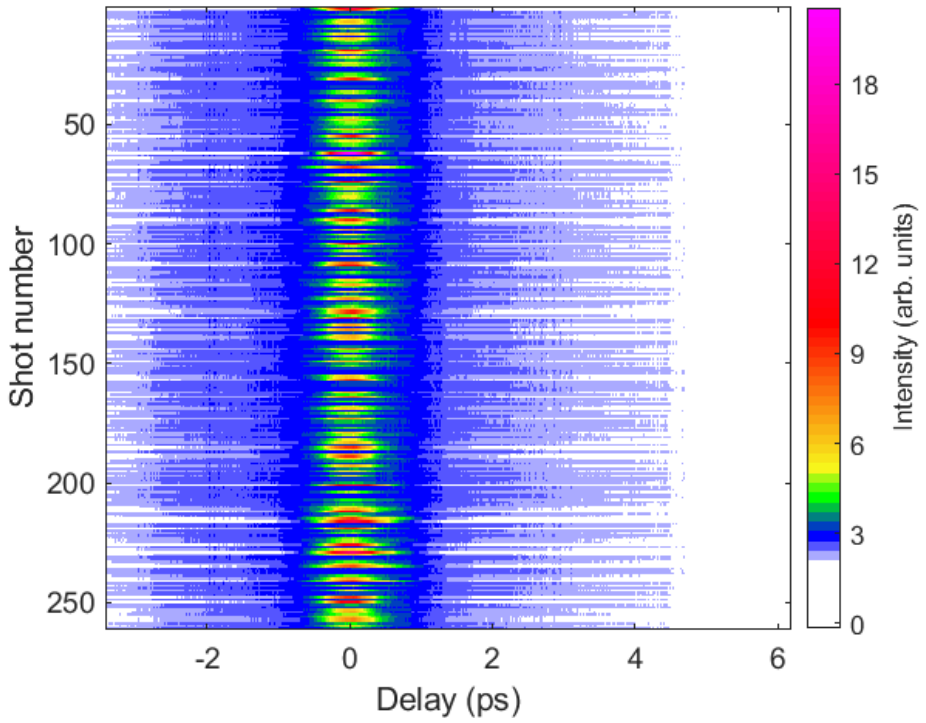

Figure 4.22. Sequence of single-shot autocorrelator traces for 261 consecutive HCF post-compressed laser pulses with spectrum described in Figure 4.17 (c) with ~ 15% broadening added by SRS. Each horizontal line in the plot is a measurement same as Figure 4.21 with the color map showing the intensity. The average and standard deviation of the sequence is 460±17 fs, the median is 455 fs, and the two extremes are 433 fs and 910 fs. 92% of the pulses are compressed to sub 600 fs.

Figure 4.22 shows the statistics of femto-second intensity profile acquired by the single shot autocorrelator. A total of 261 consecutive shots were taken with the single shot autocorrelator. The plot is normalized to the maximum intensity. The additional bandwidth created by SRS offers a lower transform limit but also introduces inconsistency. The output pulse energy from the HCF during this measurement is 215±10 mJ, with an input pulse energy of 300±19 mJ. At this condition, ~3.2 nm of bandwidth is generated by SPM and additional 5-15% broadening is generated by SRS. This additional dispersion from SRS is linked to the amount of energy that is Stoked-shifted and is leaning to the leading edge of the pulse. When the post-HCF compressor is optimized for the best bandwidth, the grating angles and distance are tuned for a specific dispersion profile. Since

the additional broadening from SRS consists of different high-order dispersion ratios, the optimized compressor angle for different broadened bandwidth is also different. As shown in Figure 4.22, the best-compensated pulses not only have the shortest compressed pulse width, but also a greatly reduced ps level background. This leads to reduced compression consistency versus the case in Figure 4.20 where the broadening is purely achieved by SPM. In this SPM/SRS mixed broadening case, with an average and standard deviation of the sequence is 460±17 fs, a total of 38% of shots are compressed to sub 500 fs and 92% of the pulses are compressed to sub 600 fs. As described earlier in the chapter, the HCF is under heavy choked flow condition, causing a steep pressure gradient near the exit of the HCF. This leads to most of the SRS broadening to be generated in a relative short distance. Thus, minor instabilities in the laser can cause jitter in the Raman-broadened spectrum, resulting in inconsistent compression. This could be mitigated with pumping methods that distributes the gas medium more evenly throughout the HCF, for example mixing different gases.

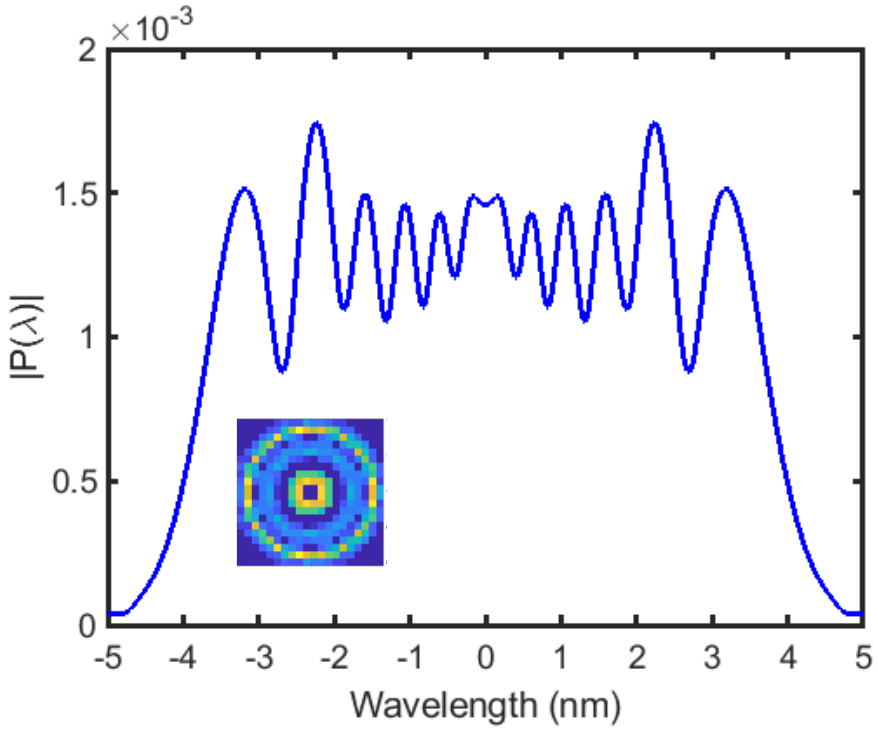

Figure 4.23. Simulated output spectrum of the HCF 100 Torr He is chosen as the non-linear medium, with 650 mJ input energy, 8 ps pulse duration and 150 um input spot size. Insert: Corresponding simulated HCF output profile.

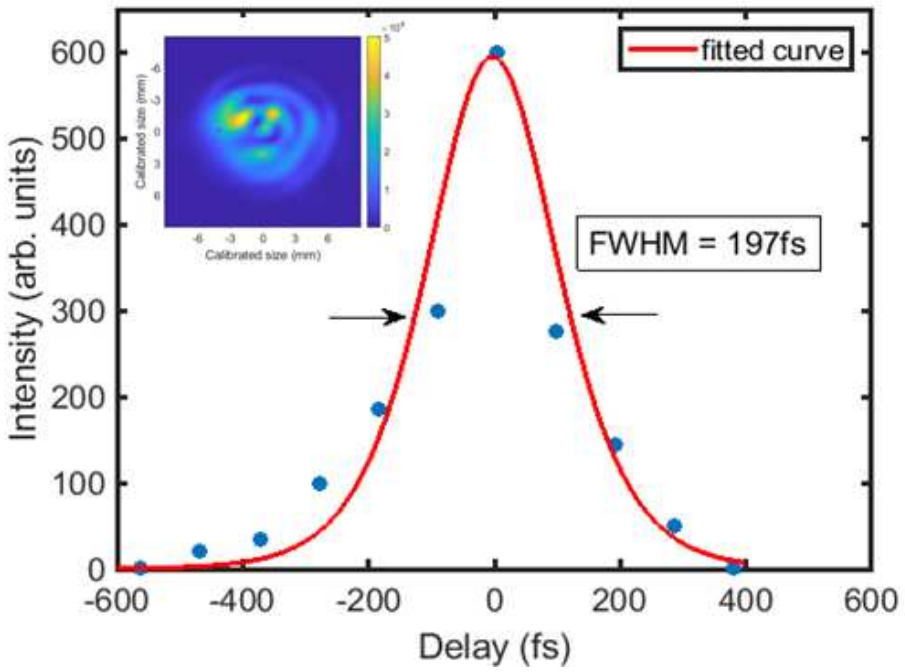

Figure 4.24. Scanning autocorrelator measurement of the compressed pulse profile for a 1 mm core HCF charged with 100 Torr of He. The input/output energy of HCF are 670 mJ/550 mJ. Each dot represents a 50-shot average of the amplitude. The curve represents a $Sech^2$ fit to the autocorrelation data. Insert: output beam profile at 2 m from the exit tip of the HCF charged with 100 Torr of He. The input/output energy of HCF are 670 mJ/550 mJ. The divergence angle is much higher due to the higher order modes, and less than 5% of the energy remains in the fundamental mode. The structure of the beam varies heavily shot-to-shot.

While our best results to date have been obtained using N_2, it might be possible that He, which has the advantage of a higher ionization potential, or Ar, may prove a better choice for use as non-linear medium. Both gases, in particular He, have the advantages of an increased flow rate and a lower pressure differential across the HCF. However, their lack of additional broadening from SRS and lower n_2 offers less SPM and therefore requires operation at higher intensity slope, which can be obtained by increasing the pulse energy and decreasing the spot size at the fiber entrance. Simulations and initial experiments for utilizing He as non-linear medium were conducted. Figure 4.23 shows the predicted spectrum for the case of using 670 mJ pulse of 8 ps duration focused onto a 150 μm diameter spot at the entrance of a fiber filled with 100 Torr of He. It has a bandwidth approaching 8 nm (< 200 fs transform limited pulsewidth). An initial experiment conducted at

these conditions showed good agreement with simulations, as shown in Figure 4.24. The smaller spot size populates higher order Bessel modes, thus further increases the peak intensity in the HCF and significantly reducing HCF tip ablation, aiding SPM. The reduced tip ablation allows for higher energy to be coupled into the HCF: up to 670 mJ were successfully coupled with 82% transmission. Up to ~ 8 nm bandwidth was achieved, in agreement with simulations. Pulses of 197 fs FWHM duration were measured as shown in Figure 4.24 from 50 shots averages per position on a scanning autocorrelator. However, the output modes in such condition (Figure 4.24 insert) are observed to be very sensitive to laser pulse variations and alignment conditions which lead to large shot-to-shot variations, and are difficult to reproduce. Since the ionization threshold and flow characteristics of He are superior, further understanding of mode propagation of high energy pulses driving SPM with high-order Bessel modes in HCFs merit further investigation.

4.4 Conclusion and further discussion.

This Chapter reports the demonstration of a high pulse energy post-compression HCF scheme applied to a cryogenic Yb:YAG laser. A 17:1 compression ratio was demonstrated. Compression down to 194 fs was also achieved, but with a degraded and unstable HCF output. Such a system makes it is possible to reach sub-ps pulse duration and TW peak power level in cryogenic Joule-class systems. Further compression to sub-100 fs pulses would open new applications in various research fields to Yb:YAG laser systems. The high input energy in HCF creates challenges and there are aspects of the technique that should be improved. Firstly, the nature of flat-top beam profile which is characteristic of high-energy laser systems, requires the fiber tip to sustain a certain percentage of laser energy without ablating when the spot size that is best for transmission is used. Improved fiber tip design and the use of special materials could aid to scale this technique to higher energy. Secondly, other combinations of fiber core size and non-linear medium each with different optical and flow characteristics could offer advantages. This includes the possibility of mixed gas media. Third, the use of circular polarization should enable scaling to higher energies since it

decreases the peak intensity in the HCF by a factor of $\sqrt{2}$. Simulations suggest potential advantages of multi-stage broadening with shorter sections. Lastly, pulse stacking could offer a solution to overcome fiber tip ablation to allow scaling to > 1 J pulse energies. Overall, there is significant potential in the use of the HCF broadening technique for compressing high energy pulses from high average power Yb laser systems.

Chapter 5 Summary and conclusion

The recent development of high energy, high repetition rate, efficient, ultrafast laser systems based on diode-pumped cryogenic Yb:YAG amplifiers opens new applications in both research and industrial technologies. Several of these applications require the generation of shaped pulse trains, or shorter pulses. The work described in this dissertation includes advances in tailoring the output pulses of a cryogenic Yb:YAG laser system based on the Joule level cryogenic amplifier, and the demonstration of their use in applications.

The performance of ion beam sputtering (IBS) coatings in the environmental conditions of cryogenic Yb:YAG amplifiers was evaluated. Since the damage threshold fluence of AR/HR optical coatings is comparable to the saturation fluence of Yb:YAG, improved coating performance is crucial for higher output energy, efficiency and reliability of such amplifiers. In order to evaluate the performance of the optical coatings used in these amplifiers, 1-on-1 and N-on-1 laser damage threshold (LIDT tests) were conducted with a LIDT setup based on the ISO:21254 standard with a deep-learning damage detection algorithm. The comparison between the coatings deposited on standard 10-5 and "superpolished" Yb:YAG substrates shows that removing subsurface defects is beneficial to increase LIDT. Damage threshold of 20.4±0.6 J/cm^2 for AR coating, and 27.4±1.3 J/cm^2 for HR coating were achieved in coatings deposited onto 0.15 nm RMS surface roughness "superpolished" Yb:YAG substrates. Environmental conditions were found to not significantly affect the LIDT behavior of IBS coated Yb:YAG crystals.

An arbitrary pulse shape synthesizer was developed to be able to temporally shape the Joule-level pulses from the CPA Yb:YAG amplifier for specific applications. The seed pulses from the front end of the chirped pulse laser system were separated into ten channels and were sent into a set of delay stages in which the intensity of individual pulses was controlled by liquid crystal windows. After amplification, the pulses can be correctly compressed in the grating compressor and formed into a pulse envelop with arbitrary shape. This method can provide an advantage in applications such as plasma generation by providing a way to tailor the heating to the plasma. The

synthesized output of cryogenic Yb:YAG laser was used to pump a λ=18.9 nm soft X-Ray laser. A 50% increase in conversion efficiency from pump laser energy to soft X-Ray output energy was obtained with a synthesized pump pulse. The best pulse structure consisted of an early pre-pulse series and a secondary picosecond pre-pulse group. The early pre-pulse series contained 5% of the total energy, and was composed of 3 individual pulses of equal intensity, separated by 70 ps intervals and was set at 850 ps prior to the main pump pulse. The secondary picosecond pre-pulse group contained 10 % of the total pulse energy, and composed of two pulses set at -35 ps and -18 ps respect to the main heating pulse, with a 25%/75% energy split.

Finally a method for post-compressing the high energy picosecond laser pulses into the femtosecond range is reported. The transform limited pulse duration of cryogenic Yb:YAG amplifiers is limited to several picoseconds by their ~0.3 nm amplified pulse bandwidth. Post compression to sub-100 fs pulse durations would make possible the use of these efficient lasers in applications such as high gradient plasma accelerators, which require both high pulse energy and femtosecond level pulse. This work demonstrates a post-compression technique that used a hollow core fiber (HCF) charged with nitrogen as the non-linear medium to compress 300 mJ, 8 ps pulses into the sub-500 fs range. Up to 300 mJ pulses were broadened to ~3 nm by self-phase modulation (SPM), and to ~4 nm with the additional broadening from stimulated Raman scattering. The broadened pulses were post compressed by a factor of 17 to a duration of 460 fs. Scaling to higher energies and post compression to shorter pulse durations are also shown to be possible using helium. Improved fiber tip design and the use of different non-liner medium could aid scaling this technique to higher energies and compression ratios. Additional pulse energy scaling of this post-compression could result from the techniques that lowers the peak intensity in the HCF, such as the use of circular polarization and pulse stacking.

Bibliography

[1] D. Strickland, and G. Mourou, "Compression of amplified chirped optical pulses," Optics Communications **56**, 219-221 (1985).

[2] M. J. LaGasse, R. W. Schoenlein, J. G. Fujimoto, and P. A. Schulz, "Amplification of femtosecond pulses in Ti:Al2O3 using an injection-seeded laser," Optics Letters **14**, 1347-1349 (1989).

[3] J. Squier, F. Salin, G. Mourou, and D. Harter, "100-fs pulse generation and amplification in Ti:Al2O3," Optics Letters **16**, 324-326 (1991).

[4] J. D. Kmetec, J. J. Macklin, and J. F. Young, "0.5-TW, 125-fs Ti:sapphire laser," Optics Letters **16**, 1001-1003 (1991).

[5] C. P. J. Barty, C. L. Gordon, and B. E. Lemoff, "Multiterawatt 30-fs Ti:sapphire laser system," Optics Letters **19**, 1442-1444 (1994).

[6] C. Danson, C. Haefner, J. Bromage, T. Butcher, J.-C. Chanteloup, E. Chowdhury, A. Galvanauskas, L. Gizzi, J. Hein, D. Hillier, N. Hopps, Y. Kato, E. Khazanov, R. Kodama, G. Korn, R. Li, Y. Li, J. Limpert, J. Ma, and J. Zuegel, "Petawatt and exawatt class lasers worldwide," High Power Laser Science and Engineering **7** (2019).

[7] T. J. Yu, S. K. Lee, J. H. Sung, J. W. Yoon, T. M. Jeong, and J. Lee, "Generation of high-contrast, 30 fs, 1.5 PW laser pulses from chirped-pulse amplification Ti:sapphire laser," Optics Express **20**, 10807-10815 (2012).

[8] Y. X. Chu, X. Y. Liang, L. H. Yu, Y. Xu, L. Xu, L. Ma, X. M. Lu, Y. Q. Liu, Y. X. Leng, R. X. Li, and Z. Z. Xu, "High-contrast 2.0 Petawatt Ti: sapphire laser system," Optics Express **21**, 29231-29239 (2013).

[9] W. Q. Li, Z. B. Gan, L. H. Yu, C. Wang, Y. Q. Liu, Z. Guo, L. Xu, M. Xu, Y. Hang, Y. Xu, J. Y. Wang, P. Huang, H. Cao, B. Yao, X. B. Zhang, L. R. Chen, Y. H. Tang, S. Li, X. Y. Liu, S. M. Li, M. Z. He, D. J. Yin, X. Y. Liang, Y. X. Leng, R. X. Li, and Z. Z. Xu, "339 J high-energy Ti:sapphire chirped-pulse amplifier for 10 PW laser facility," Optics Letters **43**, 5681-5684 (2018).

[10] P. F. Moulton, "Spectroscopic and laser characteristics of Ti:Al2O3," Journal of the Optical Society of America B **3**, 125-133 (1986).

[11] T. T. Basiev, Y. K. Voronko, T. G. Mamedov, and I. A. Shcherbakov, "Energy Migration among Yb3+ Ions in Garnet Crystals," Kvantovaya Elektronika **2**, 2172-2182 (1975).

[12] J. Filevich, J. J. Rocca, M. C. Marconi, S. J. Moon, J. Nilsen, J. H. Scofield, J. Dunn, R. F. Smith, R. Keenan, J. R. Hunter, and V. N. Shlyaptsev, "Observation of a multiply ionized plasma with index of refraction greater than one," Physical Review Letters **94** (2005).

[13] R. F. Smith, J. Dunn, J. Nilsen, V. N. Shlyaptsev, S. Moon, J. Filevich, J. J. Rocca, M. C. Marconi, J. R. Hunter, and T. W. Barbee, "Picosecond x-ray laser interferometry of dense plasmas," Physical Review Letters **89** (2002).

[14] F. Albert, N. Lemos, J. L. Shaw, P. M. King, B. B. Pollock, C. Goyon, W. Schumaker, A. M. Saunders, K. A. Marsh, A. Pak, J. E. Ralph, J. L. Martins, L. D. Amorim, R. W. Falcone, S. H. Glenzer, J. D. Moody, and C. Joshi, "Betatron x-ray radiation from laser-plasma accelerators driven by femtosecond and picosecond laser systems," Physics of Plasmas **25** (2018).

[15] F. Albert, and A. G. R. Thomas, "Applications of laser wakefield accelerator-based light sources," Plasma Physics and Controlled Fusion **58** (2016).

[16] N. Kanda, T. Imahoko, K. Yoshida, A. Tanabashi, A. A. Eilanlou, Y. Nabekawa, T. Sumiyoshi, M. Kuwata-Gonokami, and K. Midorikawa, "Opening a new route to multiport

coherent XUV sources via intracavity high-order harmonic generation," Light-Science & Applications **9** (2020).

[17] J. S. Feehan, J. H. V. Price, T. J. Butcher, W. S. Brocklesby, J. G. Frey, and D. J. Richardson, "Efficient high-harmonic generation from a stable and compact ultrafast Yb-fiber laser producing 100 μJ, 350 fs pulses based on bendable photonic crystal fiber," Applied Physics B **123**, 43 (2017).

[18] Y. Wang, H. Chi, C. Baumgarten, K. Dehne, A. R. Meadows, A. Davenport, G. Murray, B. A. Reagan, C. S. Menoni, and J. J. Rocca, "1.1 J Yb:YAG picosecond laser at 1 kHz repetition rate," Optics Letters **45**, 6615-6618 (2020).

[19] C. Herkommer, P. Krotz, S. Klingebiel, C. Wandt, D. Bauer, K. Michel, R. Kienberger, and T. Metzger, "Towards a Joule-Class Ultrafast Thin-Disk Based Amplifier at Kilohertz Repetition Rate," 2019 Conference on Lasers and Electro-Optics (Cleo) (2019).

[20] B. A. Reagan, C. Bamgarten, K. Wernsing, H. Bravo, M. Woolston, A. Curtis, F. J. Furch, B. M. Luther, D. Patel, C. S. Menoni, and J. J. Rocca, "1 Joule, 100 Hz Repetition Rate, Picosecond CPA Laser for Driving High Average Power Soft X-Ray Lasers," in *CLEO: 2014*(Optica Publishing Group, San Jose, California, 2014), p. SM1F.4.

[21] T. Nubbemeyer, M. Kaumanns, M. Ueffing, M. Gorjan, A. Alismail, H. Fattahi, J. Brons, O. Pronin, H. G. Barros, Z. Major, T. Metzger, D. Sutter, and F. Krausz, "1 kW, 200 mJ picosecond thin-disk laser system," Optics Letters **42**, 1381-1384 (2017).

[22] C. Baumgarten, M. Pedicone, H. Bravo, H. Wang, L. Yin, C. S. Menoni, J. J. Rocca, and B. A. Reagan, "1 J, 0.5 kHz repetition rate picosecond laser," Optics Letters **41**, 3339-3342 (2016).

[23] M. Smrž, O. Novák, J. Mužík, H. Turčičová, M. Chyla, S. S. Nagisetty, M. Vyvlečka, L. Roškot, T. Miura, J. Černohorská, P. Sikocinski, L. Chen, J. Huynh, P. Severová, A.

Pranovich, A. Endo, and T. Mocek, "Advances in High-Power, Ultrashort Pulse DPSSL Technologies at HiLASE," Applied Sciences **7** (2017).

[24] B. A. Reagan, K. A. Wernsing, A. H. Curtis, F. J. Furch, B. M. Luther, D. Patel, C. S. Menoni, and J. J. Rocca, "Demonstration of a 100 Hz repetition rate gain-saturated diode-pumped table-top soft x-ray laser," Optics Letters **37**, 3624-3626 (2012).

[25] C. M. Baumgarten, "Development of a High Power Chirped Pulse Amplification Laser for Driving Secondary Sources," (ProQuest Dissertations Publishing, 2019).

[26] T. Y. Fan, S. Klunk, and G. Henein, "DIODE-PUMPED Q-SWITCHED YB-YAG LASER," Optics Letters **18**, 423-425 (1993).

[27] S. Klingebiel, C. Wandt, C. Skrobol, I. Ahmad, S. A. Trushin, Z. Major, F. Krausz, and S. Karsch, "High energy picosecond Yb:YAG CPA system at 10 Hz repetition rate for pumping optical parametric amplifiers," Optics Express **19**, 5357-5363 (2011).

[28] C. L. Chang, P. Krogen, K. H. Hong, L. E. Zapata, J. Moses, A. L. Calendron, H. K. Liang, C. J. Lai, G. J. Stein, P. D. Keathley, G. Laurent, and F. X. Kartner, "High-energy, kHz, picosecond hybrid Yb-doped chirped-pulse amplifier," Optics Express **23**, 10132-10144 (2015).

[29] T. Metzger, A. Schwarz, C. Y. Teisset, D. Sutter, A. Killi, R. Kienberger, and F. Krausz, "High-repetition-rate picosecond pump laser based on a Yb:YAG disk amplifier for optical parametric amplification," Optics Letters **34**, 2123-2125 (2009).

[30] P. Lacovara, H. K. Choi, C. A. Wang, R. L. Aggarwal, and T. Y. Fan, "ROOM-TEMPERATURE DIODE-PUMPED YB-YAG LASER," Optics Letters **16**, 1089-1091 (1991).

[31] B. E. Schmidt, A. Hage, T. Mans, F. Legare, and H. J. Woerner, "Highly stable, 54mJ Yb-InnoSlab laser platform at 0.5kW average power," Optics Express **25**, 17549-17555 (2017).

[32] J. Fischer, J. Drs, F. Labaye, N. Modsching, V. J. Wittwer, and T. Sudmeyer, "Intra-oscillator high harmonic generation in a thin-disk laser operating in the 100-fs regime," Optics Express **29**, 5833-5839 (2021).

[33] J. Tummler, K. A. Janulewicz, G. Priebe, and P. V. Nickles, "10-Hz grazing-incidence pumped Ni-like Mo x-ray laser," Physical Review E **72** (2005).

[34] W. J. Brown, S. G. Anderson, C. P. J. Barty, S. M. Betts, R. Booth, J. K. Crane, R. R. Cross, D. N. Fittinghoff, D. J. Gibson, F. V. Hartemann, E. P. Hartouni, J. Kuba, G. P. Le Sage, D. R. Slaughter, A. M. Tremaine, A. J. Wootton, P. T. Springer, and J. B. Rosenzweig, "Experimental characterization of an ultrafast Thomson scattering x-ray source with three-dimensional time and frequency-domain analysis," Physical Review Special Topics-Accelerators and Beams **7** (2004).

[35] F. V. Hartemann, A. M. Tremaine, S. G. Anderson, C. P. J. Barty, S. M. Betts, R. Booth, W. J. Brown, J. K. Crane, R. R. Cross, D. J. Gibson, D. N. Fittinghoff, J. Kuba, G. P. Le Sage, D. R. Slaughter, A. J. Wootton, E. P. Hartouni, P. T. Springer, J. B. Rosenzweig, and A. K. Kerman, "Characterization of a bright, tunable, ultrafast Compton scattering X-ray source," Laser and Particle Beams **22**, 221-244 (2004).

[36] L. C. Jarrott, A. J. Kemp, L. Divol, D. Mariscal, B. Westover, C. McGuffey, F. N. Beg, M. Suggit, C. Chen, D. Hey, B. Maddox, J. Hawreliak, H. S. Park, B. Remington, M. S. Wei, and A. MacPhee, "K-alpha and bremsstrahlung x-ray radiation backlighter sources from short pulse laser driven silver targets as a function of laser pre-pulse energy," Physics of Plasmas **21** (2014).

[37] T. Tajima, and J. M. Dawson, "Laser Electron Accelerator," Physical Review Letters **43**, 267-270 (1979).

[38] C. Joshi, W. B. Mori, T. Katsouleas, J. M. Dawson, J. M. Kindel, and D. W. Forslund, "Ultrahigh gradient particle acceleration by intense laser-driven plasma density waves," Nature **311**, 525-529 (1984).

[39] M. Bailly-Grandvaux, D. Kawahito, C. McGuffey, J. Strehlow, B. Edghill, M. S. Wei, N. Alexander, A. Haid, C. Brabetz, V. Bagnoud, R. Hollinger, M. G. Capeluto, J. J. Rocca, and F. N. Beg, "Ion acceleration from microstructured targets irradiated by high-intensity picosecond laser pulses," Physical Review E **102** (2020).

[40] J. Alvarez, J. Fernández-Tobias, K. Mima, S. Nakai, S. Kar, Y. Kato, and J. M. Perlado, "Laser Driven Neutron Sources: Characteristics, Applications and Prospects," Physics Procedia **60**, 29-38 (2014).

[41] T. Fan, D. Ripin, R. Aggarwal, J. Ochoa, B. Chann, M. Tilleman, and J. Spitzberg, "Cryogenic Yb3+-Doped Solid-State Lasers," Selected Topics in Quantum Electronics, IEEE Journal of **13**, 448-459 (2007).

[42] F. X. Morrissey, T. Y. Fan, D. E. Miller, and D. Rand, "Picosecond kilohertz-class cryogenically cooled multistage Yb-doped chirped pulse amplifier," Optics Letters **42**, 707-710 (2017).

[43] J. Dong, M. Bass, Y. L. Mao, P. Z. Deng, and F. X. Gan, "Dependence of the Yb3+ emission cross section and lifetime on temperature and concentration in yttrium aluminum garnet," Journal of the Optical Society of America B-Optical Physics **20**, 1975-1979 (2003).

[44] L. J. S. P. J. Keldysh, "Ionization in the field of a strong electromagnetic wave," **20**, 1307-1314 (1965).

[45] K. Obata, K. Sugioka, and K. Toyoda, "Enhance refractive index modification of fused silica by multiwavelength excitation process using F 2 and KrF excimer lasers," (2022).

[46] Y. R. Shen, *The principles of nonlinear optics* (J. Wiley, 1984).

[47] R. Waxler, "Laser glass composition and the possibility of eliminating electrostrictive effects," IEEE Journal of Quantum Electronics **7**, 166-167 (1971).

[48] A. Owyoung, "Ellipse rotation studies in laser host materials," IEEE Journal of Quantum Electronics **9**, 1064-1069 (1973).

[49] A. V. Smith, and B. T. Do, "Bulk and surface laser damage of silica by picosecond and nanosecond pulses at 1064 nm," Applied Optics **47**, 4812-4832 (2008).

[50] J. F. Bisson, Y. Feng, A. Shirakawa, H. Yoneda, J. R. Lu, H. Yagi, T. Yanagitani, and K. I. Ueda, "Laser damage threshold of ceramic YAG," Japanese Journal of Applied Physics Part 2-Letters **42**, L1025-L1027 (2003).

[51] B. T. Do, and A. V. Smith, "Bulk optical damage thresholds for doped and undoped, crystalline and ceramic yttrium aluminum garnet," Applied Optics **48**, 3509-3514 (2009).

[52] B. C. Stuart, M. D. Feit, S. Herman, A. M. Rubenchik, B. W. Shore, and M. D. Perry, "Nanosecond-to-femtosecond laser-induced breakdown in dielectrics," Physical Review B **53**, 1749-1761 (1996).

[53] A. Dyan, F. Enguehard, S. Lallich, H. Piombini, and G. Duchateau, "Scaling laws in laser-induced potassium dihydrogen phosphate crystal damage by nanosecond pulses at 3 omega," Journal of the Optical Society of America B-Optical Physics **25**, 1087-1095 (2008).

[54] M. De Vido, D. Meissner, S. Meissner, K. Ertel, P. J. Phillips, P. D. Mason, S. Banerjee, T. J. Butcher, J. M. Smith, C. Edwards, C. Hernandez-Gomez, and J. L. Collier,

"Characterisation of adhesive-free bonded crystalline Yb:YAG for high energy laser applications," Optical Materials Express **7**, 425-432 (2017).

[55] M. De Vido, M. J. Walsh, S. Kirkpatrick, R. Svrluga, K. Ertel, P. J. Phillips, P. D. Mason, S. Banerjee, J. M. Smith, T. J. Butcher, C. Edwards, C. Hernandez-Gomez, and J. L. Collier, "Impact of gas cluster ion and accelerated neutral atom beam surface treatments on the laser-induced damage threshold of ceramic Yb:YAG," Optical Materials Express **7**, 3303-3311 (2017).

[56] W. Ackermann, G. Asova, V. Ayvazyan, A. Azima, N. Baboi, J. Bahr, V. Balandin, B. Beutner, A. Brandt, A. Bolzmann, R. Brinkmann, O. I. Brovko, M. Castellano, P. Castro, L. Catani, E. Chiadroni, S. Choroba, A. Cianchi, J. T. Costello, D. Cubaynes, J. Dardis, W. Decking, H. Delsim-Hashemi, A. Delserieys, G. Di Pirro, M. Dohlus, S. Dusterer, A. Eckhardt, H. T. Edwards, B. Faatz, J. Feldhaus, K. Flottmann, J. Frisch, L. Frohlich, T. Garvey, U. Gensch, C. Gerth, M. Gorler, N. Golubeva, H. J. Grabosch, M. Grecki, O. Grimm, K. Hacker, U. Hahn, J. H. Han, K. Honkavaara, T. Hott, M. Huning, Y. Ivanisenko, E. Jaeschke, W. Jalmuzna, T. Jezynski, R. Kammering, V. Katalev, K. Kavanagh, E. T. Kennedy, S. Khodyachykh, K. Klose, V. Kocharyan, M. Korfer, M. Kollewe, W. Koprek, S. Korepanov, D. Kostin, M. Krassilnikov, G. Kube, M. Kuhlmann, C. L. S. Lewis, L. Lilje, T. Limberg, D. Lipka, F. Lohl, H. Luna, M. Luong, M. Martins, M. Meyer, P. Michelato, V. Miltchev, W. D. Moller, L. Monaco, W. F. O. Muller, A. Napieralski, O. Napoly, P. Nicolosi, D. Nolle, T. Nunez, A. Oppelt, C. Pagani, R. Paparella, N. Pchalek, J. Pedregosa-Gutierrez, B. Petersen, B. Petrosyan, G. Petrosyan, L. Petrosyan, J. Pfluger, E. Plonjes, L. Poletto, K. Pozniak, E. Prat, D. Proch, P. Pucyk, P. Radcliffe, H. Redlin, K. Rehlich, M. Richter, M. Roehrs, J. Roensch, R. Romaniuk, M. Ross, J. Rossbach, V. Rybnikov, M. Sachwitz, E. L. Saldin, W. Sandner, H. Schlarb, B. Schmidt, M. Schmitz, P. Schmuser, J. R. Schneider, E. A. Schneidmiller, S. Schnepp, S. Schreiber, M. Seidel, D. Sertore, A. V. Shabunov, C. Simon, S. Simrock, E. Sombrowski, A. A. Sorokin, P. Spanknebel, R.

Spesyvtsev, L. Staykov, B. Steffen, F. Stephan, F. Stulle, H. Thom, K. Tiedtke, M. Tischer, S. Toleikis, R. Treusch, D. Trines, I. Tsakov, E. Vogel, T. Weiland, H. Weise, M. Wellhoffer, M. Wendt, I. Will, A. Winter, K. Wittenburg, W. Wurth, P. Yeates, M. V. Yurkov, I. Zagorodnov, and K. Zapfe, "Operation of a free-electron laser from the extreme ultraviolet to the water window," Nature Photonics **1**, 336-342 (2007).

[57] E. Allaria, R. Appio, L. Badano, W. A. Barletta, S. Bassanese, S. G. Biedron, A. Borga, E. Busetto, D. Castronovo, P. Cinquegrana, S. Cleva, D. Cocco, M. Cornacchia, P. Craievich, I. Cudin, G. D'Auria, M. Dal Forno, M. B. Danailov, R. De Monte, G. De Ninno, P. Delgiusto, A. Demidovich, S. Di Mitri, B. Diviacco, A. Fabris, R. Fabris, W. Fawley, M. Ferianis, E. Ferrari, S. Ferry, L. Froehlich, P. Furlan, G. Gaio, F. Gelmetti, L. Giannessi, M. Giannini, R. Gobessi, R. Ivanov, E. Karantzoulis, M. Lonza, A. Lutman, B. Mahieu, M. Milloch, S. V. Milton, M. Musardo, I. Nikolov, S. Noe, F. Parmigiani, G. Penco, M. Petronio, L. Pivetta, M. Predonzani, F. Rossi, L. Rumiz, A. Salom, C. Scafuri, C. Serpico, P. Sigalotti, S. Spampinati, C. Spezzani, M. Svandrlik, C. Svetina, S. Tazzari, M. Trovo, R. Umer, A. Vascotto, M. Veronese, R. Visintini, M. Zaccaria, D. Zangrando, and M. Zangrando, "Highly coherent and stable pulses from the FERMI seeded free-electron laser in the extreme ultraviolet," Nature Photonics **6**, 699-704 (2012).

[58] M. C. Chen, P. Arpin, T. Popmintchev, M. Gerrity, B. Zhang, M. Seaberg, D. Popmintchev, M. M. Murnane, and H. C. Kapteyn, "Bright, Coherent, Ultrafast Soft X-Ray Harmonics Spanning the Water Window from a Tabletop Light Source," Physical Review Letters **105** (2010).

[59] I. Pupeza, S. Holzberger, T. Eidam, H. Carstens, D. Esser, J. Weitenberg, P. Russbuldt, J. Rauschenberger, J. Limpert, T. Udem, A. Tunnermann, T. W. Hansch, A. Apolonski, F. Krausz, and E. Fill, "Compact high-repetition-rate source of coherent 100 eV radiation," Nature Photonics **7**, 608-612 (2013).

[60] S. Suckewer, and P. Jaegle, "X-Ray laser: past, present, and future," Laser Physics Letters **6**, 411-436 (2009).

[61] D. Alessi, Y. Wang, B. M. Luther, L. Yin, D. H. Martz, M. R. Woolston, Y. Liu, M. Berrill, and J. J. Rocca, "Efficient Excitation of Gain-Saturated Sub-9-nm-Wavelength Tabletop Soft-X-Ray Lasers and Lasing Down to 7.36 nm," Physical Review X **1** (2011).

[62] F. J. Furch, B. A. Reagan, B. M. Luther, A. H. Curtis, S. P. Meehan, and J. J. Rocca, "Demonstration of an all-diode-pumped soft x-ray laser," Optics Letters **34**, 3352-3354 (2009).

[63] J. Tummler, R. Jung, H. Stiel, P. V. Nickles, and W. Sandner, "High-repetition-rate chirped-pulse-amplification thin-disk laser system with joule-level pulse energy," Optics Letters **34**, 1378-1380 (2009).

[64] B. J. Macgowan, S. Maxon, P. L. Hagelstein, C. J. Keane, R. A. London, D. L. Matthews, M. D. Rosen, J. H. Scofield, and D. A. Whelan, "Demonstration of Soft-X-Ray Amplification in Nickel-Like Ions," Physical Review Letters **59**, 2157-2160 (1987).

[65] J. Nilsen, J. C. Moreno, L. B. DaSilva, and J. A. Koch, "Lasing at 79 angstrom in Ni-like nd using multiple pulse illumination and other new results," Soft X-Ray Lasers and Applications **2520**, 152-156 (1995).

[66] H. Daido, R. Kodama, K. Murai, G. Yuan, M. Takagi, Y. Kato, I. W. Choi, and C. H. Nam, "Significant Improvement in the Efficiency and Brightness of the J=0-1 19.6-Nm Line of the Germanium Laser by Use of Double-Pulse Pumping," Optics Letters **20**, 61-63 (1995).

[67] V. N. Shlyaptsev, D. James, S. Moon, R. Smith, K. Roisin, N. Joseph, B. F. Kevin, K. Jaroslav, A. L. Osterheld, J. J. G. Rocca, M. L. Bradley, W. Yong, and C. M. Mario, "Numerical studies of transient and capillary x-ray lasers and their applications," in *Proc.SPIE*(2003).

[68] S. Maxon, P. Hagelstein, K. Reed, and J. Scofield, "A Gas Puff Soft-X-Ray Laser Target Design," Journal of Applied Physics **57**, 971-972 (1985).

[69] B. M. Luther, Y. Wang, M. A. Larotonda, D. Alessi, M. Berrill, M. C. Marconi, J. J. Rocca, and V. N. Shlyaptsev, "Saturated high-repetition-rate 18.9-nm tabletop laser in nickellike molybdenum," Optics Letters **30**, 165-167 (2005).

[70] R. A. Banici, G. V. Cojocaru, R. G. Ungureanu, R. Dabu, D. Ursescu, and H. Stiel, "Pump energy reduction for a high gain Ag X-ray laser using one long and two short pump pulses," Optics Letters **37**, 5130-5132 (2012).

[71] H. T. Kim, I. W. Choi, N. Hafz, J. H. Sung, T. J. Yu, K. H. Hong, T. M. Jeong, Y. C. Noh, D. K. Ko, K. A. Janulewicz, J. Tummler, P. V. Nickles, W. Sandner, and J. Lee, "Demonstration of a saturated Ni-like Ag x-ray laser pumped by a single profiled laser pulse from a 10-Hz Ti : sapphire laser system," Physical Review A **77** (2008).

[72] G. V. Cojocaru, R. G. Ungureanu, R. A. Banici, D. Ursescu, O. Delmas, M. Pittman, O. Guilbaud, S. Kazamias, K. Cassou, J. Demailly, O. Neveu, E. Baynard, and D. Ros, "Thin film beam splitter multiple short pulse generation for enhanced Ni-like Ag x-ray laser emission," Optics Letters **39**, 2246-2249 (2014).

[73] F. Shimizu, "Frequency Broadening in Liquids by a Short Light Pulse," Physical Review Letters **19**, 1097-1100 (1967).

[74] M. Sheik-Bahae, and M. P. J. H. o. O. Hasselbeck, "Third-order optical nonlinearities," **4**, 16.11-16.36 (2000).

[75] A. C. Newell, and J. V. Moloney, *Nonlinear optics* (Addison-Wesley, 1992).

[76] H. Hora, "Y. R. Shen, The Principles of Nonlinear Optics, John Wiley & Sons, New York, 1984, 576 pages," Laser and Particle Beams **4**, 318-319 (1986).

[77] I. O. f. Standardization, "ISO 21254-1:2011," in *Lasers and laser-related equipment -- Test methods for laser-induced damage threshold*(2011).

[78] T. Day, H. Wang, E. Jankowska, B. A. Reagan, J. J. Rocca, C. J. Stolz, P. Mirkarimi, J. Folta, J. Roehling, A. Markosyan, R. R. Route, M. M. Fejer, and C. S. Menoni, "Impacts of SiO2 planarization on optical thin film properties and laser damage resistance," Laser-Induced Damage in Optical Materials 2016 **10014**, 1001422 (2016).

[79] P. Langston, D. Patel, A. Markosyan, E. M. Krous, B. Langdon, R. Route, M. Fejer, and C. S. Menoni, "SiO2/HfO2 multilayers: impact of process parameters and stack geometry on the optical and structural properties," in *Frontiers in Optics 2008/Laser Science XXIV/Plasmonics and Metamaterials/Optical Fabrication and Testing*(Optical Society of America, Rochester, New York, 2008), p. JSuA27.

[80] T. Yasuki, K. Junji, and F. Masayuki, "Nonlinear refractive index of a YAG crystal at low temperature," in *CLEO/Europe - EQEC 2009 - European Conference on Lasers and Electro-Optics and the European Quantum Electronics Conference*(2009), pp. 1-1.

[81] P. Kabaciński, T. M. Kardaś, Y. Stepanenko, and C. Radzewicz, "Nonlinear refractive index measurement by SPM-induced phase regression," Optics Express **27**, 11018-11028 (2019).

[82] N. Bloembergen, "Laser-induced electric breakdown in solids," IEEE Journal of Quantum Electronics QE-10H3(3), 375-386 (1974).

[83] H. Wang, W. L. Zhang, and H. B. He, "Laser-induced damage behaviors of antireflective coatings at cryogenic condition," Applied Optics **51**, 8687-8692 (2012).

[84] L. A. Emmert, M. Mero, and W. Rudolph, "Modeling the effect of native and laser-induced states on the dielectric breakdown of wide band gap optical materials by multiple subpicosecond laser pulses," Journal of Applied Physics **108** (2010).

[85] T. A. Laurence, R. A. Negres, E. Feigenbaum, N. Shen, S. Ly, D. Alessi, J. D. Bude, and C. W. Carr, "Laser-induced modifications of HfO2 coatings using picosecond pulses at 1053 nm: Using polarization to isolate surface defects," Journal of Applied Physics **124** (2018).

[86] T. Kamimura, S. Fukumoto, R. Ono, Y. K. Yap, M. Yoshimura, Y. Mori, T. Sasaki, and K. Yoshida, "Enhancement of CsLiB6O10 surface-damage resistance by improved crystallinity and ion-beam etching," Optics Letters **27**, 616-618 (2002).

[87] C. J. Stolz, J. E. Wolfe, P. B. Mirkarimi, J. A. Folta, J. J. Adams, M. G. Menor, N. E. Teslich, R. Soufli, C. S. Menoni, and D. Patel, "Substrate and coating defect planarization strategies for high-laser-fluence multilayer mirrors," Thin Solid Films **592**, 216-220 (2015).

[88] P. W. Wachulak, M. C. Marconi, R. A. Bartels, C. S. Menoni, and J. J. Rocca, "Soft x-ray laser holography with wavelength resolution," Journal of the Optical Society of America B-Optical Physics **25**, 1811-1814 (2008).

[89] I. Kuznetsov, J. Filevich, F. Dong, M. Woolston, W. L. Chao, E. H. Anderson, E. R. Bernstein, D. C. Crick, J. J. Rocca, and C. S. Menoni, "Three-dimensional nanoscale molecular imaging by extreme ultraviolet laser ablation mass spectrometry," Nature Communications **6** (2015).

[90] B. A. Reagan, M. Berrill, K. A. Wernsing, C. Baumgarten, M. Woolston, and J. J. Rocca, "High-average-power, 100-Hz-repetition-rate, tabletop soft-x-ray lasers at sub-15-nm wavelengths," Physical Review A **89** (2014).

[91] Y. Wang, M. A. Larotonda, B. M. Luther, D. Alessi, M. Berrill, V. N. Shlyaptsev, and J. J. Rocca, "Demonstration of high-repetition-rate tabletop soft-x-ray lasers with saturated output at wavelengths down to 13.9 nm and gain down to 10.9 nm," Physical Review A **72** (2005).

[92] A. Rockwood, Y. Wang, S. Wang, M. Berrill, V. N. Shlyaptsev, and J. J. Rocca, "Compact gain-saturated x-ray lasers down to 6.85 nm and amplification down to 5.85 nm," Optica **5**, 257-262 (2018).

[93] P. V. Nickles, V. N. Shlyaptsev, M. Kalachnikov, M. Schnurer, I. Will, and W. Sandner, "Short pulse x-ray laser 32.6 nm based on transient gain in Ne-like titanium," Physical Review Letters **78**, 2748-2751 (1997).

[94] R. Keenan, J. Dunn, P. K. Patel, D. F. Price, R. F. Smith, and V. N. Shlyaptsev, "High-repetition-rate grazing-incidence pumped x-ray laser operating at 18.9 nm," Physical Review Letters **94** (2005).

[95] B. Luther, Y. Wang, M. Larotonda, D. Alessi, M. Berrill, M. Marconi, J. Rocca, and V. Shlyaptsev, "Saturated high-repetition-rate 18.9-nm tabletop laser in nickellike molybdenum," Optics Letters **30**, 165-167 (2005).

[96] L. Yin, H. C. Wang, B. A. Reagan, and J. J. Rocca, "Programmable pulse synthesizer for the generation of Joule-level picosecond laser pulses of arbitrary shape," Optics Express **27** (2019).

[97] L. Yin, H. C. Wang, B. A. Reagan, and J. J. Rocca, "Programmable pulse synthesizer for the generation of Joule-level picosecond laser pulses of arbitrary shape," Optics Express **27**, 35325-35335 (2019).

[98] M. Berrill, D. Alessi, Y. Wang, S. R. Domingue, D. H. Martz, B. M. Luther, Y. W. Liu, and J. J. Rocca, "Improved beam characteristics of solid-target soft x-ray laser amplifiers by injection seeding with high harmonic pulses," Optics Letters **35**, 2317-2319 (2010).

[99] N. Milosevic, G. Tempea, and T. Brabec, "Optical pulse compression: bulk media versus hollow waveguides," Optics Letters **25**, 672-674 (2000).

[100] M. Kaumanns, V. Pervak, D. Kormin, V. Leshchenko, A. Kessel, M. Ueffing, Y. Chen, and T. Nubbemeyer, "Multipass spectral broadening of 18 mJ pulses compressible from 1.3 ps to 41 fs," Optics Letters **43**, 5877-5880 (2018).

[101] M. Kaumanns, D. Kormin, T. Nubbemeyer, V. Pervak, and S. Karsch, "Spectral broadening of 112 mJ, 1.3 ps pulses at 5 kHz in a LG(10) multipass cell with compressibility to 37 fs," Optics Letters **46**, 929-932 (2021).

[102] A. L. Viotti, S. Alisauskas, A. Bin Wahid, P. Balla, N. Schirmel, B. Manschwetus, I. Hartl, and C. M. Heyl, "60 fs, 1030 nm FEL pump-probe laser based on a multi-pass post-compressed Yb:YAG source," Journal of synchrotron radiation **28**, 36-43 (2021).

[103] C. Bree, J. Bethge, S. Skupin, L. Berge, A. Demircan, and G. Steinmeyer, "Cascaded self-compression of femtosecond pulses in filaments," New Journal of Physics **12** (2010).

[104] F. Krausz, C. Spielmann, T. Brabec, E. Wintner, and A. J. Schmidt, "Subpicosecond pulse generation from a Nd:glass laser using a nonlinear external cavity," Optics Letters **15**, 737-739 (1990).

[105] R. L. Fork, C. H. Brito Cruz, P. C. Becker, and C. V. Shank, "Compression of optical pulses to six femtoseconds by using cubic phase compensation," Optics Letters **12**, 483-485 (1987).

[106] M. Nisoli, S. DeSilvestri, and O. Svelto, "Generation of high energy 10 fs pulses by a new pulse compression technique," Applied Physics Letters **68**, 2793-2795 (1996).

[107] M. Ouillé, A. Vernier, F. Böhle, M. Bocoum, A. Jullien, M. Lozano, J.-P. Rousseau, Z. Cheng, D. Gustas, A. Blumenstein, P. Simon, S. Haessler, J. Faure, T. Nagy, and R. Lopez-Martens, "Relativistic-intensity near-single-cycle light waveforms at kHz repetition rate," Light: Science & Applications **9**, 47 (2020).

[108] O. Hort, A. Dubrouil, A. Cabasse, S. Petit, E. Mével, D. Descamps, and E. Constant, "Postcompression of high-energy terawatt-level femtosecond pulses and application to high-order harmonic generation," Journal of the Optical Society of America B **32**, 1055-1062 (2015).

[109] M. Giguère, B. E. Schmidt, A. D. Shiner, M.-A. Houle, H. C. Bandulet, G. Tempea, D. M. Villeneuve, J.-C. Kieffer, and F. Légaré, "Pulse compression of submillijoule few-optical-cycle infrared laser pulses using chirped mirrors," Optics Letters **34**, 1894-1896 (2009).

[110] A. Suda, M. Hatayama, K. Nagasaka, and K. Midorikawa, "Generation of sub-10-fs, 5-mJ-optical pulses using a hollow fiber with a pressure gradient," Applied Physics Letters **86** (2005).

[111] A. Hoffmann, M. Zürch, M. Gräfe, and C. Spielmann, "Spectral broadening and compression of sub-millijoule laser pulses in hollow-core fibers filled with sulfur hexafluoride," Optics Express **22**, 12038-12045 (2014).

[112] T. Nagy, S. Hädrich, P. Simon, A. Blumenstein, N. Walther, R. Klas, J. Buldt, H. Stark, S. Breitkopf, P. Jójárt, I. Seres, Z. Várallyay, T. Eidam, and J. Limpert, "Generation of three-cycle multi-millijoule laser pulses at 318 W average power," Optica **6**, 1423-1424 (2019).

[113] G. Fan, P. A. Carpeggiani, Z. Tao, G. Coccia, R. Safaei, E. Kaksis, A. Pugzlys, F. Légaré, B. E. Schmidt, and A. Baltuška, "70 mJ nonlinear compression and scaling route for an Yb amplifier using large-core hollow fibers," Optics Letters **46**, 896-899 (2021).

[114] R. H. Stolen, and C. Lin, "Self-phase-modulation in silica optical fibers," Physical Review A **17**, 1448-1453 (1978).

[115] R. H. Stolen, E. P. Ippen, and A. R. Tynes, "Raman Oscillation in Glass Optical Waveguide," Applied Physics Letters **20**, 62-64 (1972).

[116] G. Tartar, H. Ranner, F. Winter, and E. Wintner, "Simulation of optical breakdown in nitrogen by focused short laser pulses of 1064 nm wavelength," Laser and Particle Beams **26**, 567-573 (2008).

[117] C. J. Peters, M. N. Shneider, and R. B. Miles, "Kinetics model of femtosecond laser ionization in nitrogen and comparison to experiment," Journal of Applied Physics **125** (2019).

[118] C. E. Miller, "A note on the Raman spectra of nitrogen," Journal of Chemical Physics **6**, 902-904 (1938).

[119] D. V. Petrov, I. I. Matrosov, D. O. Sedinkin, and A. R. Zaripov, "Raman Spectra of Nitrogen, Carbon Dioxide, and Hydrogen in a Methane Environment," Optics and Spectroscopy **124**, 8-12 (2018).

[120] M. A. Henesian, C. D. Swift, and J. R. Murray, "Stimulated Rotational Raman-Scattering in Nitrogen in Long Air Paths," Optics Letters **10**, 565-567 (1985).

[121] A. M. Weiner, J. P. Heritage, and R. H. Stolen, "Effect of stimulated Raman scattering and pulse walkoff on self-phase modulation in fibers," in *Conference on Lasers and Electro-Optics*, G. H. E. M. P. Bjorklund, and D. Pinnow, eds. (Optica Publishing Group, San Francisco, California, 1986), p. THC4.

[122] D. Schadt, B. Jaskorzynska, and U. Österberg, "Numerical study on combined stimulated Raman scattering and self-phase modulation in optical fibers influenced by walk-off between pump and Stokes pulses," Journal of the Optical Society of America B **3**, 1257-1262 (1986).

[123] D. Eimerl, D. Milam, and J. Yu, "Large bandwidth frequency-converted Nd:glass laser at 527 nm with $\Delta\nu$=2%," Physical Review Letters **70**, 2738-2741 (1993).

[124] G. S. McDonald, G. H. C. New, L. L. Losev, A. P. Lutsenko, and M. Shaw, "Ultrabroad-bandwidth multifrequency Raman generation," Optics Letters **19**, 1400-1402 (1994).

[125] R. H. Stolen, and A. M. Johnson, "The Effect of Pulse Walkoff on Stimulated Raman-Scattering in Fibers," Ieee Journal of Quantum Electronics **22**, 2154-2160 (1986).

[126] T. G. B. de Souza, E. C. Barbano, S. C. Zilio, and L. Misoguti, "Measurement of nonlinear refractive indices of air, oxygen, and nitrogen in capillary by changing the temporal width of short laser pulses," Journal of the Optical Society of America B **34**, 2233-2237 (2017).

[127] J. Schwarz, P. Rambo, M. Kimmel, and B. Atherton, "Measurement of nonlinear refractive index and ionization rates in air using a wavefront sensor," Optics Express **20**, 8791-8803 (2012).

[128] M. C. Potter, M. Hondzo, and D. C. Wiggert, *Mechanics of fluids* (Cengage Learning, 2010).

[129] M. V. Ammosov, N. B. Delone, and V. P. Krainov, "Tunnel Ionization of Complex Atoms and Atomic Ions in a Varying Electromagnetic-Field," Zhurnal Eksperimentalnoi I Teoreticheskoi Fiziki **91**, 2008-2013 (1986).

[130] S. Hulin, T. Auguste, P. D'Oliveira, P. Monot, S. Jacquemot, L. Bonnet, and E. Lefebvre, "Soft-x-ray laser scheme in a plasma created by optical-field-induced ionization of nitrogen," Physical Review E **61**, 5693-5700 (2000).